METHODS FOR MRI-GUIDED TREATMENT OF PAINFUL BONE METASTASES WITH FOCUSED ULTRASOUND

Beatrice Lena

Colophon

Printed by: Ridderprint

Cover design: Arianna Godio, Paola Sodano, Beatrice Lena
Layout: Beatrice Lena, Pascal Ramaekers, Luisa Raimondo

ISBN: 978-94-6458-511-7

Thesis with a summary in Dutch, English and Italian, Utrecht University
Beatrice Lena, 2022

The research described in this thesis was supported by the Applied and Engineering Sciences research program (project number 15179), which is partly financed by the Netherlands Organization for Scientific Research,the Dutch Cancer Society, and PPP allowance of Top Sector Life Sciences & Health. Printing of this thesis was partially supported by: Grad School, GSLS, Utrecht University.

METHODS FOR MRI-GUIDED TREATMENT OF PAINFUL BONE METASTASES WITH FOCUSED ULTRASOUND

Methoden voor MRI-geleide behandeling van pijnlijke botmetastasen met gefocusseerd ultrageluid
(met een samenvatting in het Nederlands)

Metodi per trattamenti di metastasi ossee dolorose con ultrasuoni focalizzati guidati dalla risonanza magnetica
(con un riassunto in Italiano)

Proefschrift

ter verkrijging van de graad van doctor aan de
Universiteit Utrecht,
op gezag van de
rector magnificus, prof.dr. H.R.B.M. Kummeling,
ingevolge het besluit van het college voor promoties
in het openbaar te verdedigen op
donderdag 29 september 2022 des middags te 12.15 uur

door

Beatrice Lena

geboren op 23 maart 1992
te Borgomanero, Italië

Promotoren:
Prof. Dr. ir. M. A. Viergever
Prof. Dr. C. T. W. Moonen
Copromotoren:
Dr. ir L. W. Bartels
Dr. C. Bos

Beoordelingscommissie:
Prof. dr. J. J. Verlaan (voorzitter)
Prof. dr. ir. C. A.T. van den Berg
Prof. dr. H.M. Verkooijen
Prof. dr. P.A.J. Hilbers
Prof. dr. ir. T.W.J. Scheenen

The work presented in this thesis was carried out at the Image Science Institute (ISI), Imaging Division, Department of Radiology at the University Medical Center Utrecht.

Contents

1 General Introduction **1**
1.1 (High-Intensity) Focused Ultrasound for cancer therapy: a re-discovered technique 2
1.2 (High-Intensity) Focused Ultrasound as palliative treatment for painful bone metastases 4
1.2.1 Pain palliation of bone metastases 4
1.3 Technical challenges 6
1.4 Thesis Outline 10

2 Synthetic CT for the planning of MR-HIFU treatment of bone metastases . **15**
2.1 Introduction 17
2.2 Methods 17
2.2.1 Patient Data 17
2.2.2 Acquisition parameters 18
2.2.3 Preprocessing 19
2.2.4 Neural Network 19
2.2.5 Evaluation 19
2.3 Results 20
2.4 Discussion 22
2.5 Supplementary Materials 27

3 Rapid 2D Variable Flip Angle Method for T_1 Measurements **31**
3.1 Introduction 33
3.2 Theory 34
3.2.1 T_1 mapping using the Variable Flip Angle Method 34
3.2.2 Correction of 2D VFA T_1 mapping 34
3.3 Methods 36
3.3.1 Applicability of the linearization in the 2D VFA method 37
3.3.2 Performance of 2D VFA T_1 mapping (over a range of FAs) 37
3.3.3 Experimental validation 38
3.4 Results 39
3.4.1 Applicability of the linearization in the 2D VFA method 39
3.4.2 Performance of 2D VFA T_1 mapping (over a range of FAs) 40
3.4.3 Experimental validation 43
3.5 Discussion 44
3.6 Conclusion 47

3.7 Supplementary Materials 48

4 Interleaved water and fat MRT for HIFU ablation of bone lesions 53
4.1 Introduction 55
4.2 Methods 56
4.2.1 Identification of water and fat voxels 56
4.2.2 Calculation of temperature maps 56
4.2.3 Ex vivo MR-HIFU heating experiment 58
4.2.4 Non-heating demonstration on a volunteer 59
4.3 Results 59
4.3.1 Ex vivo MR-HIFU heating experiment 59
4.3.2 Non-heating demonstration on a volunteer 60
4.4 Discussion 62
4.5 Conclusion 63

5 The influence of fat layer thickness and sonication settings on the EDBS. . . 65
5.1 Introduction 67
5.2 Materials and Methods 68
5.2.1 The tools 68
5.2.2 Simulation and measurements under varying realistic conditions 72
5.3 Results 75
5.3.1 Simulations of the experiments 75
5.3.2 MR-HIFU experiments 77
5.3.3 Comparison of energy and temperature 78
5.4 Discussions 81
5.5 Supplementary Materials 84

6 General Discussion 89
6.1 Technical Considerations 90
6.2 Future perspectives 93

7 Appendices 101
English Summary 103
Nederlandse Samenvatting 107
Riassunto in Italiano 111
Bibliography 115
List of Publications 129
Acknoledgments 131
Acknoledgments 131
About the author 141

1

General Introduction

Magnetic Resonance Imaging (MRI), medical application of the Nuclear magnetic resonance (NMR) spectroscopy [1], is one of the techniques of choice for medical imaging thanks to its excellent soft tissue contrasts. Based on the interactions of the hydrogen protons in the body with the surrounding atomic and molecular tissue environment, it is relatively safe, noninvasive and versatile [2]. Besides its use for clinical diagnostic imaging, MRI is suited for guidance of thermal therapies, as it allows temperature mapping during the treatment [3–5]. It may sound almost incredible that playing with the physics of tissues, it is possible not only to acquire high-resolution anatomical images but also to map temperature in near real-time.
In the last decades, minimally invasive and noninvasive thermal therapies have gained interest as local treatments of benign and malignant diseases, since they reduce infection risks, shorten the hospital stays and allow for more rapid recovery. The most common thermal therapies employ radiofrequency (RF), laser, microwave, or therapeutic ultrasound (US) to heat tissues, without using ionizing radiation [6]. The first three generate heat through probes by long electromagnetic waves, whereas ultrasound is a technique based on short mechanical waves. Although it is possible to generate focused heat through microwaves or radiofrequencies, long waves cannot be focused as precisely as shorter waves, and their penetration depth is limited. The use of short waves as therapeutic ultrasound with High-Intensity Focused Ultrasound (HIFU) provides adequate tissue penetration, ranging from 1 to 20 cm, non-invasively, allowing the creation of localized heated areas [7].
This thesis covers the work carried out to improve MR-guided High-Intensity Focused Ultrasound (MR-HIFU) therapies, specifically in the context of palliative treatment of painful bone metastases. The rest of this chapter will introduce the current state of the art and highlights some of the specific gaps in scientific knowledge in this discipline, starting with the role of Focused Ultrasound treatments for cancer therapy.

1.1. (HIGH-INTENSITY) FOCUSED ULTRASOUND FOR CANCER THERAPY: A RE-DISCOVERED TECHNIQUE

"The 45-year history of research in cancer therapy involving ultrasound may be divided into the four periods of initiation, enthusiasm, pessimism, and revival"
(Kremkau F., Journal of Clinical Ultrasound, 1979)[8].

The principle of focused ultrasound involves the transmission of ultrasound waves into the body from a US transducer, after ensuring acoustic coupling between the transducer and the body. The interference of US waves emitted from the transducer elements creates a beam that can be focused within the body (Figure 1.1). The absorption of ultrasound energy by the tissues generates thermal heating within the focus. This effect has been exploited for local tumor control, through thermal ablation [9]. A variety of therapeutic applications of HIFU are being investigated and/or are clinically available[10–15], most of them based on local tissue destruction by thermal ablation. Although focused ultrasound has been proposed and adopted in clinical care for many oncological applications only in the last twenty years [16], the use of ultrasound in cancer therapy was already debated in 1979 [8]. The first investigations with HIFU date

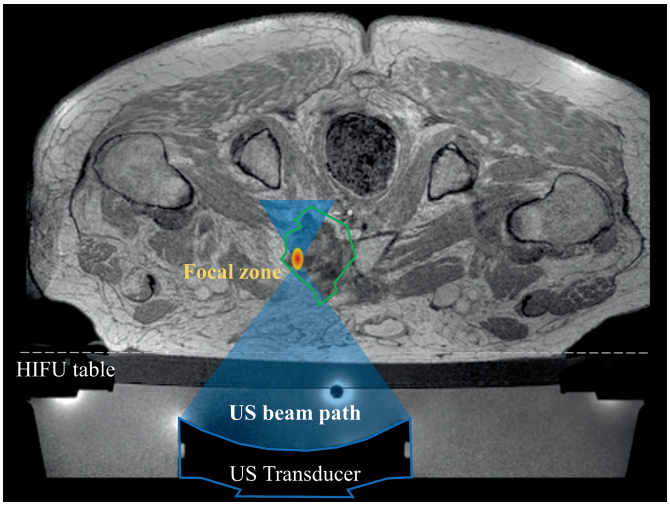

Figure 1.1: Illustration of ultrasound waves being focused on a bone metastasis. The metastatic region is within the green shape.

back to 1942 [17] and the earliest HIFU interventions were conducted in the 1950's [18]. However, technical limitations, as the lack of reliable image guidance and the difficulties to target the US beam noninvasively, made the technique less favourable to be introduced in the clinical setting [19].

HIFU was rediscovered in the 1990s with the introduction of MR-compatible transducers that allows MRI as image guidance modality [20] and the development of phased-array ultrasound transducers which permitted the focusing of the ultrasound beams using a hemispheric transducer design [19, 21]. Such rediscovery was substantially promoted by investigations into the potential uses of HIFU in urology. Early clinical trials were found successful until some extent for treatments of prostate cancer, by means of HIFU under US guidance [22, 23].

Nowadays, the modern HIFU devices combine different technological advances into a single unit: the thermal ablation with high-intensity focused ultrasound with either MRI guidance and temperature MR mapping or US guidance [24]. In current clinical practice, HIFU interventions are predominantly guided by one of these two imaging modalities and each modality presents advantages and disadvantages. US imaging is cheap, portable, compatible with patient implants and its frame rate favourable for imaging moving organs [25]. MR imaging has excellent soft tissue differentiation, provides spatial guidance in the targeted area independently from the acoustic absorption and reflection of tissues (inside the skull, for example) and is able to monitor temperature intraprocedurally using temperature-dependent proton resonance frequency shift, T_1 temperature mapping, or diffusion temperature mapping [7].

Over the past two decades, continuous advances in imaging, transducer design, modes of energy delivery and engineering have accelerated the clinical introduction of cancer therapy using HIFU [26]. An important transition of the field from early-staged to first-in-human clinical trials happened in 2017, when for the first time the number of HIFU procedures in clinical trials overtook their number in a preclinical stage [27].

Fourty-two years after the paper from Kremkau, we could complete his sentence: up to now, the 87-year history of research in cancer therapy involving ultrasound as treatment option may be divided into the five periods of initiation, enthusiasm, pessimism, revival and clinical application.
Nowadays, the main clinical applications of HIFU involve tumor-debulking applications as thermal ablation of uterine fibroids and liver and prostate cancer, and palliative procedures as thermal ablation of painful bone metastases [28, 29]. Specifically, two clinically used MR-HIFU systems, Insightec and the Philips Sonalleve, received the European Conformity (CE) marking for the treatment of painful bone metastases in 2007 and 2011, respectively [30].

1.2. (HIGH-INTENSITY) FOCUSED ULTRASOUND AS PALLIATIVE TREATMENT FOR PAINFUL BONE METASTASES

"There is evidence to suggest that focused US directed at the skeletal system can cause immediate damage"
(Smith N.B. et al, Ultrasound in Medicine and Biology, 2001)[31].

The effect described by Smith et al. became the strongest rationale for applications of HIFU on bone and the reason why MR-HIFU procedures emerged as feasible and safe treatment options for patients with painful bone metastases [32–34].
The initial applications of HIFU treatment on bone were limited to lesions on the bone surface [35], as only a small portion of waves penetrates the bone itself, while the major part is absorbed or reflected to neighbouring structures. This effect is due to the high ultrasound absorption rate of the bone [36]. This high ultrasound absorption and the low heat capacity of bone leads to an increase in temperature in the bone itself with respect to the temperature in the surrounding soft tissues [37–39]. Following studies demonstrated that the high temperatures elevations at the soft tissue/bone interface caused critical thermal damage to the adjacent periosteum (a complex innervated structure that cover bones) [40, 41]. Early HIFU procedures in the 1980's reported significant, sometimes intolerable, pain in patients [35, 42, 43], probably caused by bone heating, and treatments were planned to avoid temperature elevations at the bone surface [37, 44].
Current treatments of bone lesions take advantage of the critical damage to the periosteum and play an important role in pain palliation of bone metastases [33].

1.2.1. PAIN PALLIATION OF BONE METASTASES

Bone metastases.
Bone metastases are a common complication of cancer, with approximately 320,000 new cases per year in the United States (from the American Cancer Society, 2021[45]) and are expected to increase as patients with cancer live longer. The bone is the third most common site of metastatic disease after the lungs and the liver and mostly arise from primary sites as breast, prostate and lung [46, 47].

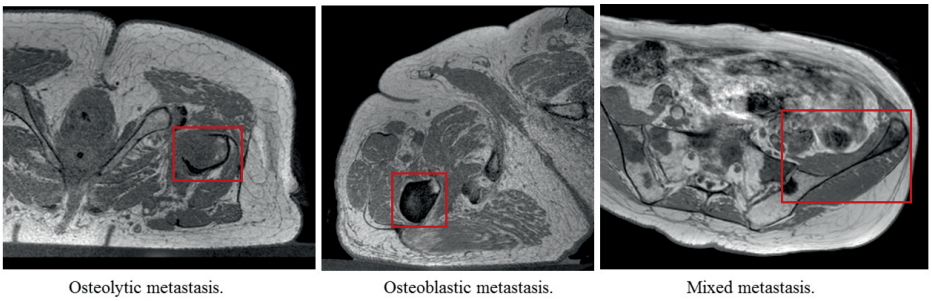

Figure 1.2: Types of bone metastasis: osteolytic (bone destruction), osteoblastic (new bone formation) and mixed. The metastases are within the red box.

Bone metastases differ in aspect depending on the interactions between the cancer cells and the tissue microenvironment. They can be characterized by bone cortex destruction, in case of osteolytic metastases, or new bone formation, in case of osteoblastic metastases, or a combination of both, leading to mixed lesions (Figure 1.2). The nature of the metastasis can be associated with the primary tumor, for example breast cancers are associated mainly with osteolytic metastases, while prostate cancers with osteoblastic ones [48].

Pain.
Metastatic bone pain is a common symptom, occurring in 60%-70% of patients with bone metastases and can negatively affect quality of life and daily functioning [49–52]. It is often related to the metastasis itself, possibly caused by:

- the tumor mass, which compresses or infiltrates the nerves;
- injury to local nociceptors (the "pain receptors"), which alters the nerve impulse transmission.

Based on its cause, bone pain can be characterized as nociceptive (i.e., caused by tissue injury) or neuropathic (i.e., caused by damage to the nervous system). Both forms can occur simultaneously, making it challenging to characterize and manage the pain [49, 50].

Treatment of bone metastases.
Up to now, external beam radiotherapy (EBRT) combined with opioids is the standard modality for local treatments of painful bone metastases. Approximately 47–80% of patients experience at least some degree of pain relief within three to eight weeks after the treatment [53–55]. Thirty percent of patients do not respond to EBRT at all, and 50% of responders will experience recurrent pain [55–57]. Retreatment with radiotherapy of non-responders or those with recurrent pain is limited by radiation dose and is effective only in 60% of patients [58]. Finally, even in patients that show pain response, delayed side effects do not always lead to an improvement of the quality of life, as shown by the analysis of the Dutch Bone Metastasis study [59].

In patients with bone metastases, generally with a limited expected survival, immediate pain relief is important, and complications of treatments should be minimized. In this context, MR- HIFU is a promising additional/alternative treatment to radiotherapy, being a non-invasive procedure that may provide fast and durable pain palliation [32, 36, 60, 61]. Already three days after the treatment, 50-73% of the treated patients showed significant pain reduction [34]. Moreover, the treatment procedure may be repeated safely if required, because no ionizing radiation is used.
Pain relief is thought to be achieved by:

- Ablation of the nerves causing the pain, especially the periosteum: as a rule of thumb, lethal cell damage, i.e., protein denaturation and cell death, occurs when temperatures >55 °C are maintained for at least one second [62, 63];
- Shrinkage of the tumor mass, which may lead to pain reduction by relieving the pressure on nearby nerves;
- Local denervation, caused by tissue heating damages of nociceptive fibres and decrease of their density [64].

Although further research is needed to better understand the mechanisms of pain palliation with HIFU and to fully establish its efficacy, HIFU procedures have been found promising to treat both nociceptive and neuropathic pain of bone metastases [64, 65]. Improvements in the quality of life of the patients, as physical functioning in addition to pain relief, have been reported already within a few days after a single MR-guided HIFU treatment session [66].
Moreover, other benefits that have recently been reported are:

- Facilitation of local cancer mass control, especially in case of cortical bone interruption [67];
- Stimulation of the immune response against the tumor [68];
- Potential bone remineralization after the treatment [69];
- Enhancement of the therapeutic effects of radiation therapy.

Currently, a project funded by the European Commission, the FURTHER project, is investigating the effectiveness of MR-HIFU as an alternative or additional treatment option for pain relief caused by bone metastases. A randomised controlled trial is conducted comparing pain response in patients treated in 9 different centres with radiotherapy only, MR-HIFU only and radiotherapy combined with MR-HIFU[70].

1.3. TECHNICAL CHALLENGES

"Focused Ultrasound is something right out of Star Trek. You can cure tumors, through the skin without having to cut it"
(Patient treated for painful bone lesion, "FUF. Bringing the Future into Focus", 2016)[71].

Focused ultrasound can be directed from outside into lesions inside the body, without the need for surgery. At the focus, the ultrasound intensity is so high, that tissue heating leading to cell death occurs. In this way, nerves responsible for the pain from bone metastases can be very locally eliminated. This concept has been shown to work, but some technological challenges at each treatment step need to be addressed in order to broaden the scope of its applicability.

Prior to therapy: Eligibility assessment
Prior to the treatment procedure, the eligibility of a patient for the procedure should be assessed. Usually, key parameters to assess eligibility are target lesion size, location and accessibility to the ultrasound beam. Imaging plays an important role at this stage, to depict the tumor and its surrounding environment (including the beam path) for a possible treatment planning. CT is better suited for the exposure of cortical bone loss or bone creation, inherent to bone metastases and the assessment of the integrity or infiltration of adjacent cortical bone, whereas MRI provides means for the delineation of the lesion. These two imaging examinations are not always acquired pre-procedurally, as the acquisition with both modalities is expensive and increase patients' burden.

Therapy Planning
In this stage, visualization of the target area is essential [72]. The absorption of ultrasonic energy in the lesion strongly depends on the composition of the lesion, in particular on the amount of cortical bone present [31, 37]. Therefore, accurate depiction of the lesion and the surrounding environment is important. Moreover, the presence of layers of different tissue types in the beam path determine the beam attenuation and the location and shape of the ultrasound focus, which may result in insufficient heating of target lesions and unwanted heating outside the target area. In this context, MRI offers excellent tissue contrasts and is capable of providing three-dimensional images for treatment safety and efficacy.
For HIFU procedures of bone metastases, the treatment is planned mostly on MR images, however, cortical bone, also referred to as compact bone, gives non-specific and almost zero signal on conventional MRI, due to its low water content and short relaxation times. Methods for direct visualization of compact bone using MRI have been explored through use of sequences with short echo times, as ultrashort- and zero- echo time sequences (UTE, ZTE) [73], that are able to measure signal of tissues with very short relaxation times. However, despite improving bone specificity, these sequences face challenges in developing adequate contrast between bone and other structures as air or tissue interfaces. This is particularly problematic for the evaluation of bone integrity in the metastases. In addition, UTE and ZTE sequences are not yet commonly available to be used in clinical workflow.
Another way to improve depiction of the bone distribution in and around the lesion is through registration of the CT images acquired for the eligibility assessment phase to MR images acquired on the treatment day [74]. However, this registration can be difficult because the CT and MR images are often acquired with the patient in different positions (Figure 1.3) and some physiological changes may have occurred between the two acquisitions.
Currently, a method that allows the visualization of soft tissues and the depiction of

the bone distribution in the target and its surrounding with the patient in treatment position is lacking.

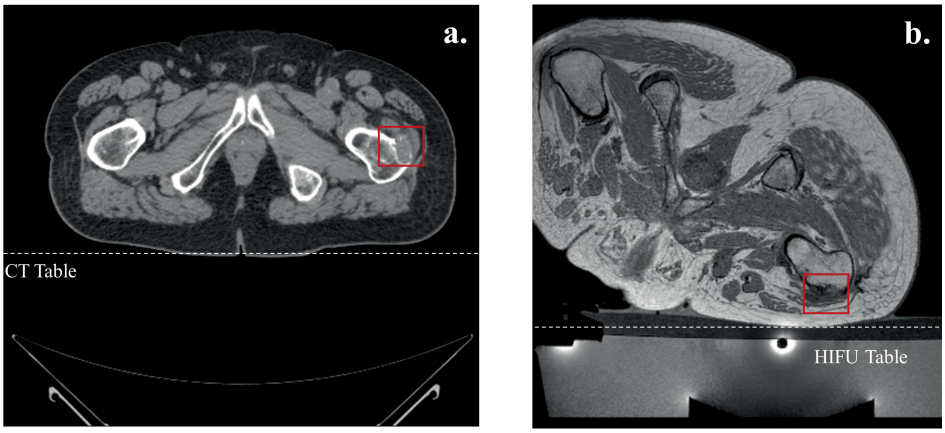

Figure 1.3: Scans from two image modalities of a patient with an osteoblastic metastasis in the femur. a.) CT image, b.) MR image acquired with the patient in treatment position. The transducer is submerged in an oil reservoir in the HIFU table, and the metastasis is within the red box.

Therapy Monitoring

Therapy should be monitored in real time to ensure treatment efficacy, i.e., delivering sufficient energy to reach lethal damage in the target zone, and treatment safety, i.e., preventing damage to its surrounding. MR imaging with its ability to monitor temperature provides means to fulfil this requirement. MR temperature mapping allows monitoring of the temperature increase in the target area and avoiding unwanted thermal damage in the surrounding healthy tissues [4].

The most employed MR thermometry (MRT) technique for clinical procedures in water-based tissue is based on the proton resonance frequency shift (PRFS) of hydrogen nuclei in water molecules. PRFS-based thermometry became popular because of its easy implementation with rapid gradient echo sequences and the linear temperature dependence of the PRFS of water, which is almost independent of the tissue type the water resides in. However, PRFS-based temperature mapping is often hampered by lack of information from cortical bone and fat containing tissues [75]. Thus, during clinical procedures, temperature information is only available in voxels containing aqueous tissues, like muscle or tumor tissue (Figure 1.4).

Therapy monitoring of bone metastases treatments might benefit of fat thermometry, since often adipose tissues as bone marrow or subcutaneous fat are present in the surrounding of the lesion. Alternative MRT methods based on the MR relaxation times have shown promising results to provide quantitative temperature information in fat containing tissues [76–79]. However, these methods are often too slow for monitoring MR-HIFU ablation of bone metastases [76] and/or their precision could be improved [77, 79]. Therefore, there is the need for fast and precise MR thermometry that allow

temperature monitoring intraprocedurally in water and fat, in and around the metastasis.

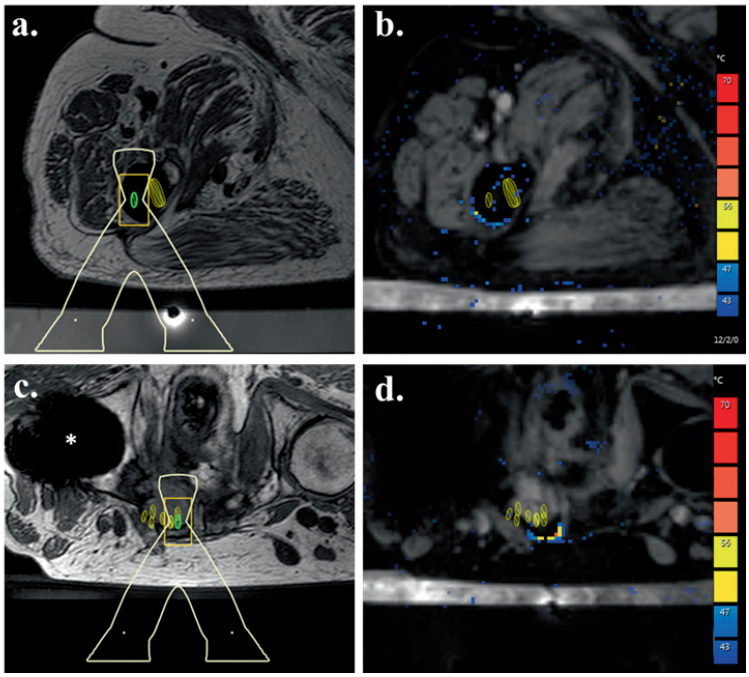

Figure 1.4: Images acquired during the treatment session of two patients with osteoblastic metastasis in femur (first row) and osteolytic metastasis in pelvis (second row), this patient had also an implant in the right femur, indicated by *. In both cases, the metastases were surrounded by fat and bone. (a.-c.) Images from the planning sequence, with the location of the planned sonications (in green) and the shape of the ultrasound beam cone overlayed. (b.-d.) the MR thermometry maps, estimated with the PRFS method: temperature estimates could only be calculated in the soft tissues in the proximity of the lesions.

Evaluation of Therapy progress

In the context of palliative procedures on painful bone metastases, the success of a treatment is determined by pain relief for the patient. Such a relief may be experienced 1 to a few days after the treatment. Therefore, a feature available during the treatment that could be adjusted to maximize therapy efficacy is useful.

In this sense, MR imaging offers a variety of features that are sensitive to different HIFU-induced changes [29]. Thermal maps, acquired through MRT sequences, can be used to quantify exposure of tissue to hyperthermic conditions through the deposited thermal dose [62, 80] and setting a dose threshold for complete cell death, to predict the extent of the thermal damage. However, the thermal dose threshold depends on the tissue type [81] and does not include non-thermal HIFU effects.

Contrast-enhanced (CE) MRI is another frequently used MR method to evaluate treatment effect. Images are acquired before and after the injection of a Gadolinium-based contrast agent, in which the region characterized by a lack of signal enhancement (referred to as nonperfused volume NPV) corresponds to the ablated region. However, this method is less suitable for evaluation of treatments of bone metastases, as an

MR imaging-based evaluation of the ablation zone through NPV is not straightforward when ablating thin periosteal layers. In case of osteoblastic/mixed lesions, the non-enhanced region is not clearly identified, as newly bone formation is not as vascularized as soft tissue lesions (Figure 1.5), thus it becomes hard to use the NPV to predict treatment efficacy after MR-HIFU procedures treatment in bone [65, 82].

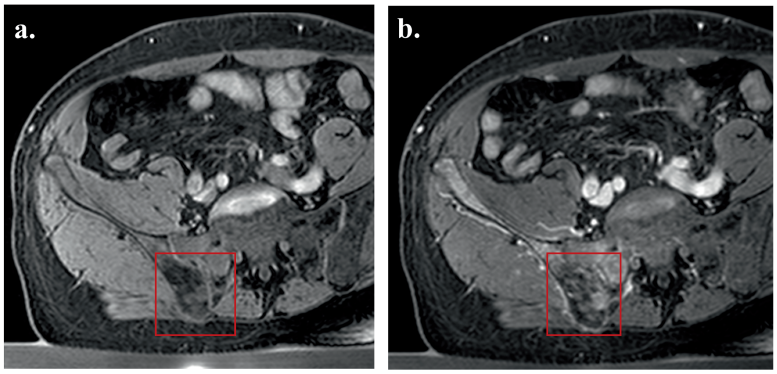

Figure 1.5: MR images acquired post-treatment before (a.) and after (b.) gadolinium injection from a patient with an osteoblastic metastasis (within the red box) in the pelvis. After contrast injection, it is possible to identify a hypointense region in the metastasis. However, it is hard to assess if this is a treatment effect or only inherent to the blastic character (mainly composed by bone) of the metastasis, as a low-signal region was visible in the metastasis also prior to contrast injection.

To overcome the limitations of image-based evaluation, the use of a parameter independent from MR and solely based on the ultrasound knowledge has been proposed in a study using retrospective patient data [83]. This parameter, named "energy density on the bone surface" (EDBS), has the potential to become a good predictor of therapy outcome. However, a thorough understanding of how to calculate the EDBS coefficient and the practical implications for its use in the clinics are currently missing.
Efforts should be made to improve the methods for lesion visualization, treatment monitoring and treatment evaluation for thermal ablation of bone lesions through HIFU interventions. The author of this thesis focused on improving some of them, in particular:

- Depiction of the bone distribution in and around the lesion for planning of HIFU treatments;
- Rapid and precise water and fat thermometry for monitoring of HIFU ablation;
- Practical implications for the use of the EDBS during treatment sessions as indicator for the expected HIFU treatment results.

1.4. THESIS OUTLINE

"This is not fiction. This is the future, and it is rapidly approaching".
John Grisham and Dr. Neal Kassell, "Curing with sound", TEDxCharlottesville, 2015.

The work described in this thesis was aimed at developing and / or improving methods to contribute to the future of image-guided focused ultrasound ablation of bone metastases. From the problems identified in the paragraph 1.3, we saw and investigated opportunities to improve treatment planning, monitoring and evaluation of interventions on painful bone metastases.

Therapy Planning
Although the use of specific sequences and registration techniques could improve bone visualization, currently, in clinical care, planning of HIFU treatments on bone metastases is hard as the bone distribution in and around the metastasis is not easily identifiable. This task is extremely challenging especially because of the different types (lytic or blastic) of metastatic bone.
One way to visualize osseous tissues through MRI is using synthetic CT (sCT), i.e., deriving CT-like images from MRI scans. This method has already shown promising results for radiotherapy [84] and orthopaedic purposes [85, 86]. In **Chapter 2**, a method to improve the visualization of the target area during treatment planning is presented. This method combines synthetic CT with MR images aiming to facilitate the visualization of soft tissue and bone in patients in treatment position. The potential of this approach to adequately depict the cancellous and cortical bone distribution in the different lesion types is investigated.

Therapy Monitoring
As PRFS-based thermometry is unreliable in adipose tissues, alternative methods have been proposed to monitor temperature in fat, involving multiecho PRF thermometry [87], T_2 thermometry of bulk fat [76], and hybrid PRF-T_1 thermometry [78, 88, 89]. In hybrid PRF- T_1 thermometry, T_1 mapping is often performed using the 3D Variable Flip Angle (VFA) method [90], as the VFA method is more suitable for real-time thermometry than the conventional T_1-mapping sequences based on inversion recovery. The conventional VFA method could additionally be sped up, by switching to 2D acquisition. In **Chapter 3**, a method based on 2D VFA is evaluated for rapid time-resolved T_1 mapping for a range of T_1. In **Chapter 4** the proposed T_1 mapping through 2D-VFA is interleaved with PRF mapping to allow thermometry in aqueous and adipose tissues. This could aid monitoring HIFU treatments of bone applications, for which both tissue types can be found in the vicinity of the target.

Evaluation of Therapy progress
Ideally, the use of treatment predictors associated with clinical outcomes could improve therapy outcome. The predictions of these indicators could entail changes in treatment parameters to maximize therapy efficacy. The EDBS has shown positive correlation with treatment outcome on retrospective data [83]. This could be promising in the search for a treatment predictor. However, for the use of this parameter during treatment sessions, it is important to know how it depends on conditions that typically vary between patient cases.
Therefore, in **Chapter 5**, an investigation of the definition of EDBS is presented. Direct measurement of this parameter in patients is not possible, but it can be estimated in different ways, through physical models and/or simulations of varying complexity. To

study how it is influenced by other conditions and parameters during HIFU treatments on bone metastases, experiments and simulations are performed in controlled phantom environments (involving bone, fat and soft tissue-mimicking gel) under varying realistic sonication conditions and for varying object geometries/anatomies.

2

SYNTHETIC CT FOR THE PLANNING OF MR-HIFU TREATMENT OF BONE METASTASES IN PELVIC AND FEMORAL BONES: A FEASIBILITY STUDY

Based on:
Lena B.*, Florkow M.C.*, Ferrer C.J., van Stralen M., Seevinck P. R., Vonken E.P.A., Boomsma M.F., Slotman D.J., Viergever M.A., Moonen C.T.W., Bos C., Bartels L.W. Synthetic CT for the planning of MR-HIFU treatment of bone metastases in pelvic and femoral bones: a feasibility study. *European Radiology (2022)*.

"An optimal treatment planning requires an accurate evaluation on both CT and MR"

(Scipione R. et al., Seminars in Interventional Radiology, 2018) [36]

ABSTRACT

Objectives: Visualization of the bone distribution is an important prerequisite for MRI-guided high-intensity focused ultrasound treatment planning of bone metastases. In this context, we evaluated MRI-based synthetic CT (sCT) imaging for the visualization of cortical bone.

Methods: MR and CT images of nine patients with pelvic and femoral metastases were retrospectively analyzed in this study. The metastatic lesions were osteolytic, osteoblastic or mixed. sCT were generated from pre-treatment or treatment MR images using a UNet-like neural network. sCT was qualitatively and quantitatively compared to CT in the bone (pelvis or femur) containing the metastasis and in a region of interest placed on the metastasis itself, through mean absolute difference (MAD), mean difference (MD), Dice similarity coefficient (DSC), and root mean square surface distance (RMSD).

Results: The dataset consisted of 3 osteolytic, 4 osteoblastic and 2 mixed metastases. For most patients, the general morphology of the bone was well represented in the sCT images and osteolytic, osteoblastic and mixed lesions could be discriminated. Despite an average timespan between MR and CT acquisitions of 61 days, in bone the average (±standard deviation) MAD was 116 ±26 HU, MD -14 ±66 HU, DSC 0.85 ±0.05, and RMSD 2.05 ±0.48 mm and in the lesion, MAD was 132 ±62 HU, MD -31 ±106 HU, DSC 0.75 ±0.2, and RMSD 2.73 ±2.28 mm.

Conclusion: Synthetic CT images adequately depicted the cancellous and cortical bone distribution in the different lesion types, which shows its potential for MRI-HIFU treatment planning.

2.1. INTRODUCTION

Magnetic resonance imaging-guided high-intensity focused ultrasound (MRI-HIFU) has shown promising results for therapy in bones and joints [36, 67, 91, 92]. Particularly, MRI-HIFU has shown potential for pain palliation in patients with bone metastases [83], where the suspected mechanism of action is the thermal ablation of the nerves that produce the pain [32, 40, 49].

The treatment volume may be limited to the superficial periosteum for palliative denervation, or it can also involve ablation of the deeper tumor tissue[36]. During treatment planning for pain palliation, adequate depiction of the cancellous and cortical bone in and around the lesion in treatment position is required for choosing a treatment strategy appropriate for the lesion type [33]. In case of tumor ablation, delineation of the lesion is also required. MRI is suitable to characterize soft tissues within or adjacent to the periosteum. However, computed tomography (CT) is better suited to expose cortical bone loss (in osteolytic lesions) or bone creation (in osteoblastic lesions) [48], inherent to bone metastases.

Currently, patient eligibility assessment for HIFU treatment and lesion characterization are done using CT scans, and occasionally pre-treatment MRI scans, acquired prior to HIFU treatment [36, 72]. These scans are also used on the treatment day to choose a suitable treatment strategy approach, depending on the integrity of the bone cortex [33, 41]. However, patient positions in pre-treatment and treatment images usually differ. In addition, pre-treatment images may have been acquired up to months prior to the MRI-HIFU treatment procedure, so clinically significant delay may exist between the scans.

To provide information on the cancellous and cortical bone distribution in and around the lesion in MR-HIFU treatment position, strategies to register pre-treatment CT to MR images have been investigated. However, interscan registration was reported to be a complex time-consuming process and pathological changes over time were ignored [74].

In the last decade, the development of synthetic CT (sCT), i.e., deriving CT-like images from MRI scans, has enabled an MRI-based visualization of osseous tissues for radiotherapy [84] and orthopedic care [85, 86, 93, 94]. In the MR-HIFU context, such sCT images could be generated from MR images acquired during the treatment session to depict the bone distribution in the treatment position. Although sCT generation has been used for orthopaedic purposes [85, 86, 95] and HIFU treatment planning [96], its ability to reconstruct bone blastic or lytic lesions is unknown.

We implemented a fast and automated method for sCT generation that enables the combined visualization of soft tissue and cortical bone. By qualitatively and quantitatively comparing sCT with CT, we investigated the potential of sCT images for visualizing cancellous and cortical bone in patients with bone metastases.

2.2. METHODS

2.2.1. PATIENT DATA

Imaging data of nine patients were used retrospectively for this study. The patients were screened for palliative MRI-HIFU treatment of bone metastases at the radiology department of Isala Hospital (Zwolle, The Netherlands), between January 2019 and De-

cember 2019 and written informed consent for the use of their data for scientific research was obtained. All patients underwent radiotherapy before the MRI-HIFU treatment. For the purpose of this study, all data were anonymized.

2.2.2. ACQUISITION PARAMETERS

All patients had a pre-treatment CT scan, available from radiotherapy planning. Acquisition parameters are shown in Table 2.1.

Table 2.1: Main imaging sequence parameters for pre-treatment CT and pre-treatment and treatment MR scans. Values between square brackets indicate a range. TE = echo time; TR = repetition time.

CT	
CT scanner	iCT 256, Brilliance Big Bore or Ingenuity CT, Philips Healthcare
In-plane reconstructed pixel size (range)	[0.67 - 0.98] × [0.67 - 0.98] mm^2
Slice spacing	3 mm
Tube Voltage	120 kV
Exposure	[69 - 253] mAs
MR	
MR scanner	Achieva, Philips Healthcare
Type	Radiofrequency-spoiled T_1-weighted multi-echo gradient-echo
Scan mode	3D
In-plane pixel size (range)	[0.92 - 1] × [0.92 - 1] mm^2
Partition thickness	2 mm
TE1/ TE2 / TR	2.1/4.2/7 ms
Flip Angle	10°
Number of slices	150
Acquisition duration	≈ 3 minutes

MRI scans were acquired on a 1.5T scanner. Pre-treatment MR scans were acquired with a 16-element coil with the patient in supine position. Treatment MRI scans were acquired with an integrated 2-element coil inside the HIFU tabletop (Sonalleve V2, Profound Medical) combined with an external 3-element pelvic coil. Treatment position was chosen to minimize the distance between the transducer and the lesion, with proper acoustic access to the lesion. In both MRI sessions, the same sequence was included.

The average time between acquisition of the pre-treatment CT and the treatment MR was 61 days (range: [1; 165] days), whereas the average time between pre-treatment CT and pre-treatment MRI, which was available for four patients, was 31 days (range: [6; 104] days). If available, pre-treatment MR images were used for training and evaluation to minimize interscan positioning and pathophysiological differences. If not, treatment MR images were used (n = 5/9).

2.2.3. PREPROCESSING

Segmentation

The pelvic and femoral bones were semi-automatically segmented on the MR and CT images using image processing software (Mimics Medical 21.0, Materialize). Lesion masks were semi-automatically created on the MR images by a radiologist, using segmentation software (ITK-Snap v3.8.0 [97]).

Registration

CT images were registered to the MR images in two steps. First, an iterative closest point algorithm [98] applied on the MR- and CT-based bone segmentations combined with a dual quaternion interpolation of the soft tissues initialized the registration [99]. Then, an image-based deformable registration was applied on the entire body contour, using open source registration software (Elastix [100]). Given the challenging registration task due to large differences in patients' positioning between the scanning sessions (Figure 2.1), this registration focused on matching the bones at the expense of the surrounding soft tissues. During registration, CT images were resampled to the MRI resolution using cubic B-spline interpolation. In the remainder of the chapter, CT refers to the registered CT.

Normalization

MR intensities were clipped beyond the 95th percentile to exclude the hyperintense signal from the fluid surrounding the transducer inside the HIFU tabletop and then linearly mapped to [-1; 1]. CT intensities were linearly mapped from the Hounsfield unit range [-1024; 3071] to [-1; 1].

2.2.4. NEURAL NETWORK

Synthetic CT images were generated by means of a 3D patch-based UNet-like neural network [101, 102], using an architecture and hyperparameters previously applied for sCT generation in the hip [103]. The neural network took as inputs MR images at two echo times and was trained to minimize the L1 distance between the CT and sCT at a learning rate of 10-4 using an Adam optimizer [104]. During the training, data were augmented to artificially increase the training set. Random flipping of the coronal and sagittal planes and random rotation between -45° and 45° around the feet-head axis were applied to simulate the unconventional patient positioning.
Because of the small amount of data, the network was trained using leave-one-out cross-validation resulting in nine models. For each model, seven data sets were used for training, one for validation, and one as an independent test set. Training and testing were done on a GeForce RTX 2080 Ti (NVIDIA) graphics processing unit.

2.2.5. EVALUATION

To evaluate accuracy, sCT images were compared to CT images in the bone containing the metastasis and the metastasis itself, using the masks as segmented on the MR im-

ages. The metrics used for evaluation were the mean sCT-to-CT difference (MD), mean absolute difference (MAD), the Dice similarity coefficient (DSC) [105] and the sCT-to-CT root mean square surface distance (RMSD) [106]. For the analysis on the bone and the lesion, cancellous and cortical bone were extracted from the CT and sCT images, by means of a 150 HU [107, 108] threshold applied within the bone and the lesion masks, respectively. The DSC and the surface distance were computed between CT and sCT on the extracted bones. Particularly for the surface distance estimation, the lesion masks included a 3-cm margin around them. These methodological steps are summarized in Figure 2.1.

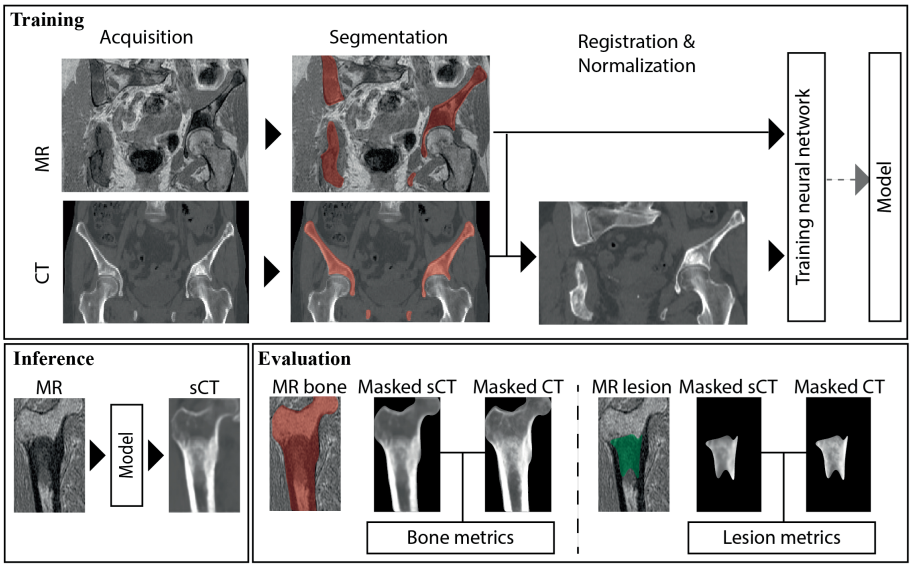

Figure 2.1: Schematic description of the approach. The bone containing the lesion was segmented on MRI and CT and used to register the CT to the MRI. Patches of 24x24x24 voxels were then extracted from the MRI and registered CT to train a synthetic CT (sCT) generation model. Once trained, the model was used to create a sCT of the bone of interest from a patient not seen during the training. The sCT was then evaluated in the bone of interest and the metastatic lesion.

2.3. RESULTS

The characteristics of the population are described in Table 2.2. Synthetic CT images were generated in 66 s from an MR image of matrix size 352×352×150. On average per patient, sCT images were generated in 80 s from the T_1-w gradient-echo images.

Table 2.2: Demographics and clinical characteristics of the patients.

Patient	Patient Sex	Primary Tumor type	Metastasis type	Location of the metastasis	Days between CT and HIFU
P1	Male	Bladder	Mixed	Pelvis	13
P2	Female	Breast	Mixed	Pelvis	35
P3	Female	Colon	Osteoblastic	Pelvis	157
P4	Male	Lung	Osteolytic	Femur	165
P5	Female	Bile duct	Osteolytic	Femur	10
P6	Male	Prostate	Osteoblastic	Femur	1
P7	Male	Prostate	Osteoblastic	Pelvis	1
P8	Male	Liver	Osteolytic	Pelvis	126
P9	Male	Prostate	Osteoblastic	Pelvis	3

Metrics for the quantitative comparison of CT and sCT for all patients are reported in Table 2.3 for the bone containing the lesion and in Table 2.4 for the lesion only. Average ±standard deviation voxelwise differences were: MAD: 116 ±26 HU and MD: -14 ±66 HU in the bone and MAD: 132 ±62 HU and MD: -31 ±106 HU. The MD in the bone of interest was overall negative, which indicates that bone intensities in sCT images were on average underestimated.

Table 2.3: Mean absolute difference (MAD), mean difference (MD), Dice similarity coefficient (DSC) and root mean square difference (RMSD) obtained for each patient between the sCT and CT in the bone containing the lesion. DSC and RMSD were obtained using a threshold of 150 Hounsfield units.

P#	MAD (HU)	MD (HU)	DSC (1)	RMSD(mm)
P1	102	34	0.81	2.70
P2	146	23	0.86	2.54
P3	132	-26	0.74	1.74
P4	96	-47	0.85	1.38
P5	77	29	0.88	1.67
P6	154	119	0.90	1.90
P7	136	-98	0.89	2.11
P8	109	87	0.9	1.76
P9	95	7	0.85	2.65

Despite voxelwise differences, the bone distribution was similar between the CT and sCT, as evidenced by an average DSC among patients of 0.85 ±0.05 in the bone and of 0.75 ±0.2 in the lesion.
The surface of the bone and the osseous tissues inside the lesion have been preserved in the sCT, as indicated by the sCT-to-CT surface distance analysis. The largest errors have been found close by and in the lesion: the average ±standard deviation RMSD

Table 2.4: Mean absolute difference (MAD), mean difference (MD), Dice similarity coefficient (DSC) and root mean square difference (RMSD) obtained for each patient between the sCT and CT in the metastatic lesion. DSC and RMSD were obtained using a threshold of 150 Hounsfield units. Patients are stratified per lesion type.

Lesion Type	P#	MAD (HU)	MD (HU)	DSC (1)	RMSD(mm)
Osteolytic	*P4*	188	100	0.74	1.42
	P5	27	12	0.77	0.75
	P8	108	-51	0.60	3.87
Osteoblastic	*P3*	166	101	0.82	2.08
	P6	235	-229	0.96	0.89
	P7	81	29	0.99	2.08
	P9	149	-123	0.49	7.30
Mixed	*P1*	94	-64	0.56	4.93
	P2	143	-55	0.86	2.86

equals 2.73 ±2.28 mm in and around the lesion compared to 2.05 ±0.48 mm in the entire bone. Three-dimensional bone renderings with overlays of sCT-to-CT surface distances obtained in the bone and in the lesion are available for all patients in Supplementary Material Figure 2.S1. Representative cases of sCT images were obtained for patients presenting osteoblastic (Figure 2.2a), osteolytic (Figure 2.2b) and mixed (Figure 2.2c) lesions are shown in Figure 2.2 along with sCT-to-CT difference maps. The soft tissues around the lesions were well characterized in MR images. Most errors were located in dense and sclerotic regions, although bone formation was identifiable. Synthetic CT images were slightly blurred causing some of the intensity underestimation seen in Tables 2.3 and 2.4.

Overall, a good sCT-CT correspondence has been observed as shown in Figure 2.3 which displays the sCT images of all patients. For three patients, significant differences between sCT and CT were visible, but their cause, sCT generation errors or interscan pathological changes, can hardly be determined given the long timespan between the MRI and CT acquisitions. For one patient, the model largely underestimated the sclerotic region.

Figure 2.4 shows the potential use of sCT as a bone visualization tool for planning of MR-HIFU treatment in the pelvis and femur.

2.4. DISCUSSION

In this study, we evaluated the potential of deep learning-based synthetic CT generation for the visualization of cancellous and cortical bone to support MR-HIFU treatment planning for metastases in pelvic and femoral bones. Combining MRI and CT-like imaging in a single reference frame would be useful to better define the region of treatment and the bone cortex, during treatment planning for pain palliation (and

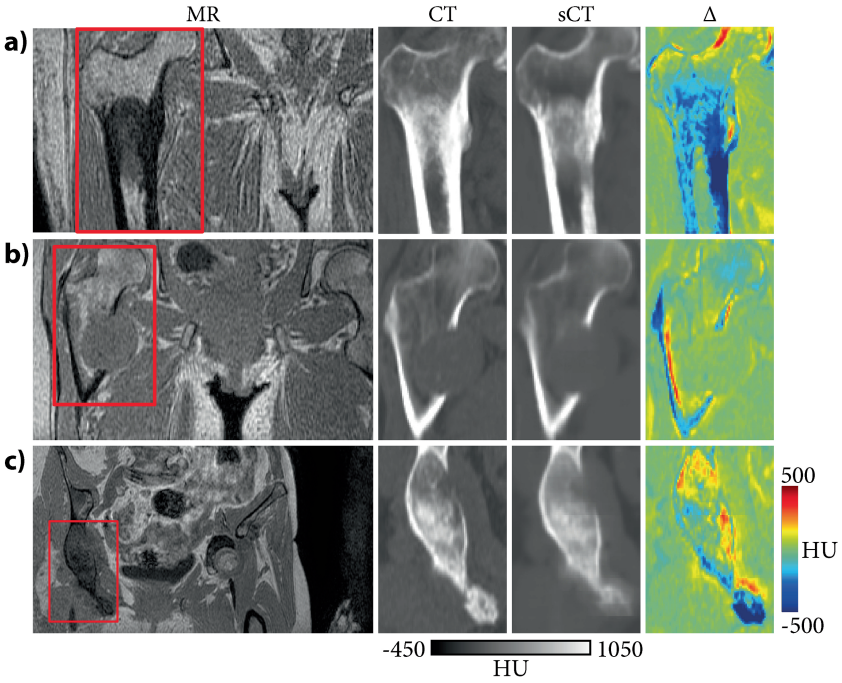

Figure 2.2: MR, CT, synthetic CT (sCT) and sCT-to-CT difference (Δ) obtained for three patients presenting a) osteoblastic, b) osteolytic and c) mixed lesions. Red boxes on the MR images indicate the region that was zoomed in to compare CT and sCT images.

tumor ablation, if attempted). The short sCT generation time (< 2 min) required per patient makes this approach suitable for on-the-fly treatment planning. Pretreatment CT and sCT images showed similar cortical bone distribution in patients with bone metastases.

For treatment planning, qualitative visualization of the bone distribution in the lesion and its vicinity is paramount. Inadequate depiction of the lesion can result in over- or under- treatment of the lesion and potential damage to the surrounding tissue. CT could be used for bone cortex depiction, but a recent CT is not always available and large differences in patient positioning during pretreatment CT imaging and treatment MR-imaging are often present. Synthetic CT offers an easier interpretation of the bone distribution in treatment position, facilitating physicians to perform the ablations [33]. The delineation and characterization of the lesion could be performed on MRI. However, sometimes it is unclear where remaining parts of cortical bone are present, solely based on (intraprocedural) MRI. Here, sCT might have additional value for characterization and/or delineation of the metastasis. Moreover, sCT images could potentially be used for identification of other bony structures along the US beam path and serve as input for sonication simulations to facilitate treatment cell positioning and optimization of sonication protocols for energy deposition in the target lesion [109, 110]. This approach of combined sCT and MR images could also be of value for other fields of MR-HIFU applications in bones, such as treatment of osteoid osteoma. However, the

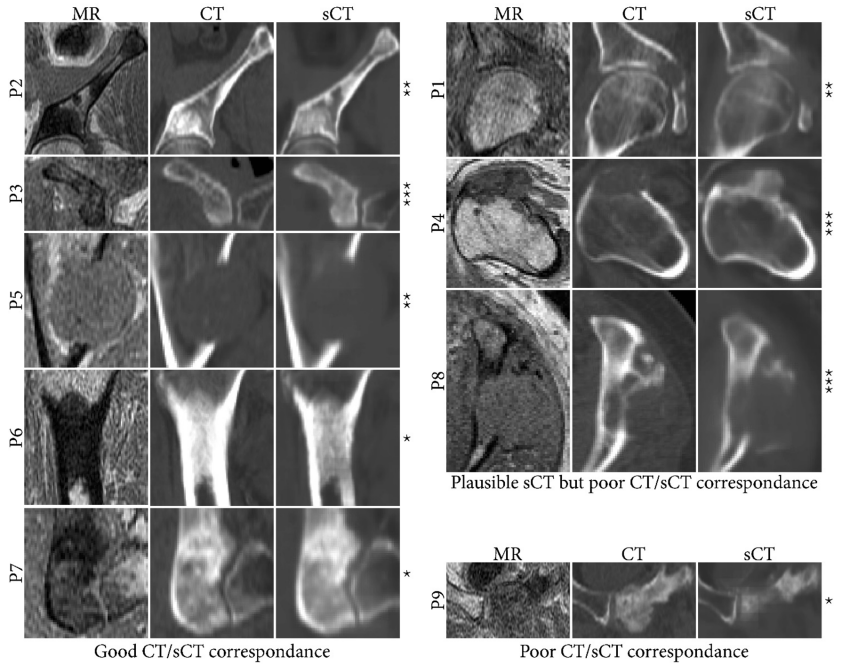

Figure 2.3: Comparison of single slices out of the MR, CT and sCT datasets of all patients, divided by their sCT-CT correspondence in the lesion. For most patients, lesions could be correctly identified on sCT images. For three patients, differences were observed between CT and sCT images, but it is hard to judge whether they are due to pathological changes (e.g., calcium-enriched bone visible in CT but not MRI in P8) or error in sCT reconstruction. For one patient, definite sCT reconstruction errors are visible with sclerotic regions not well depicted. Stars indicate different timespan between pretreatment CT and treatment MR: $*$ < 10 *days*, $**$ 10 – 35 *days*, $***$ > 100 *days*.

network will probably need to be re-trained with osteoid osteoma data.
The quantitative metrics obtained in this study are comparable to the results reported in literature, with MAD in the bone larger than 125 HU reported in the lower arm and pelvis for patients with no known orthopaedic conditions [94, 103]. However, this observation on limited data does not allow to draw general conclusions.
In its current implementation, the model was able to provide a rough estimation of the cortical bone distribution in and around the lesion. The exact lesion contour was more approximate, presumably because of its irregular geometry, which might cause partial volume issues in images, and of the slightly blurred sCT images.
Anatomical changes caused by tumor progression could partially explain the lower DSC and higher RMSD of the surface distance between CT and sCT in the lesion. For 6/9 patients, the timespan between the CT and MR was longer than 10 days, the approximate time interval in which anatomical changes would typically occur (Figure 2.2 and example case in Supplementary Materials, Figure 2.S2). Motion artifacts could also afflict the sCT generation and its comparison with CT (see P1 in Supplementary Materials, Figure 2.S3). For one patient, definite sCT reconstruction errors were observed, presumably because the metastasis was newly formed as evidenced by hyperintense signal in the almost opposed-phase image and hypointense signal in the almost in-phase image [111]. This hyperintense signal was observed only in this patient (Supple-

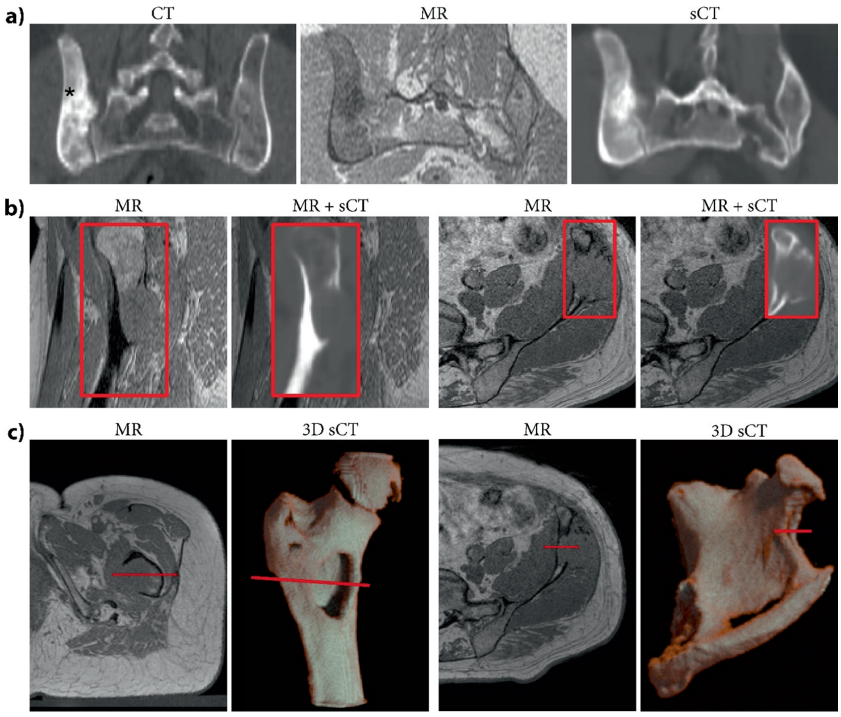

Figure 2.4: a). Pretreatment CT images in the pelvis with conventional patient positioning and MR and intrinsically aligned synthetic CT (sCT) images with unconventional patient positioning for the HIFU treatment. Lesion is indicated by *. Since sCT scans are intrinsically registered with MR, they are able to provide bone cortex depiction with the patient in treatment position. b). MR and a fused visualization of MR and sCT images depicting the cortical bone distribution, obtained for two patients with osteolytic lesions in the femur (left) and in the pelvic iliac crest (right). MR and sCT are inherently registered, allowing straightforward identification of soft tissues and bone. c). MR images from transverse slices of two patients with lesions in the femur and pelvis and corresponding 3D bone renderings that provides an overview of the bone with the lesion. The bone renderings were obtained by thresholding the sCT at 150 Hounsfield units within the bone mask (created in MeVisLab v3.2, MeVis Medical Solutions AG) . The red line identifies the same location in MR images and 3D bone renderings.

mentary Materials, Figure 2.S4) and the sCT error could be solved either on the processing side by adding more newly formed osteoid cases to the training set or, on the acquisition side, by acquiring MR data with more than 2 echoes, to make the model less sensitive to the relaxation time T_2* (shorter in this lesion compared to other tissues).
We acknowledge several limitations to this study. First, the presented results show the potential of MR-based synthetic CT for a limited dataset and more data are required to assess the robustness of the method across patients. However, the lesions were all located in the hip region, which is the most commonly treated region with MRI-HIFU [83]. To limit overfitting caused by the small dataset, a patch-based method with a limited receptive field was used to facilitate the generalizability of the model and data augmentation was applied to feed the network with data corresponding to unconventional patient positioning.
In addition, only the metastatic bone and the lesion were evaluated with sCT, as soft tissues can be better assessed on MR images. Bone reconstruction was slightly blurry,

partly because of registration errors in the training set, mainly due to positioning differences between pretreatment and treatment scans [112]. In the future, by acquiring pre-treatment MR scans in addition to the pre-treatment CT scans, the registration of the training set would be improved and interscan differences would be reduced, leading to the generation of sharper sCT images.

To conclude, this study demonstrated the potential of sCT for visualizing cancellous and cortical bone distribution for HIFU treatment procedures of bone metastases in the hip region. Osteolysis and ossification were visible on the sCT images with the bone distribution comparable between CT and sCT within the bone of interest. Thus, synthetic CT images could help in visualizing bone lesions with CT-like contrasts for planning of palliative MRI-HIFU procedures, including the targeting of the lesions and treatment planning.

2.5. SUPPLEMENTARY MATERIALS

Figure 2.S1:

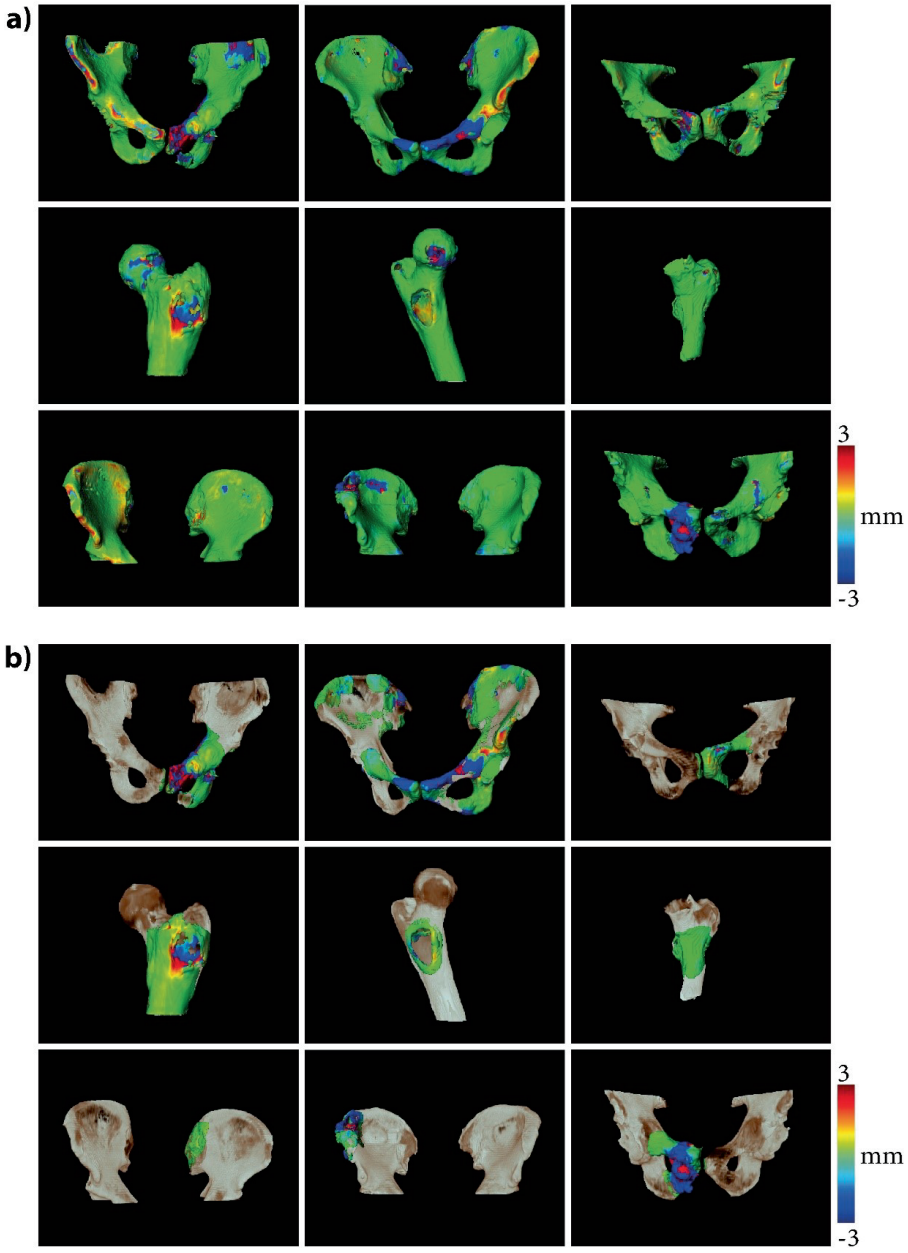

Figure 2.S1: sCT-to-CT surface distance maps of the patients images obtained in this study, (a) in the entire bone, (b) on a 3 cm margin around and including the lesion.

Figure 2.S2: Possible changes in the lesion between the acquisitions are problematic when comparing sCT (generated from treatment MR) with pretreatment CT. For example, for patient 8, such changes were documented on two subsequent CT scans acquired 2 months apart, followed by MR HIFU treatment another 2 months later. Pathophysiological changes were observed between March and May and so could be expected between May and July. Example of CT scans from patient 8:

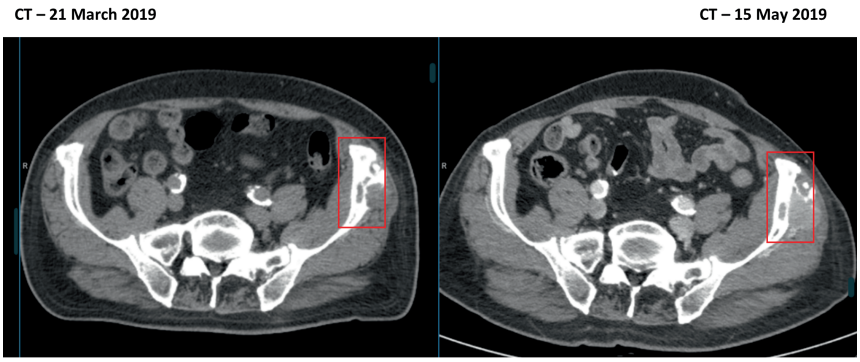

Figure 2.S2: The osteolytic progress of the lesion between 2 CT scans, leading to local changes close by and in the pelvis bone. The lesion is indicated by a red square. The CT scan acquired in May was contrast-enhanced.

Figure 2.S3: An MR image afflicted by motion artefacts could result in sCT of lower quality, especially when compared to a CT scan. This could explain the low DSC achieved in the lesion in P1. Example of pretreatment MR from patient 1:

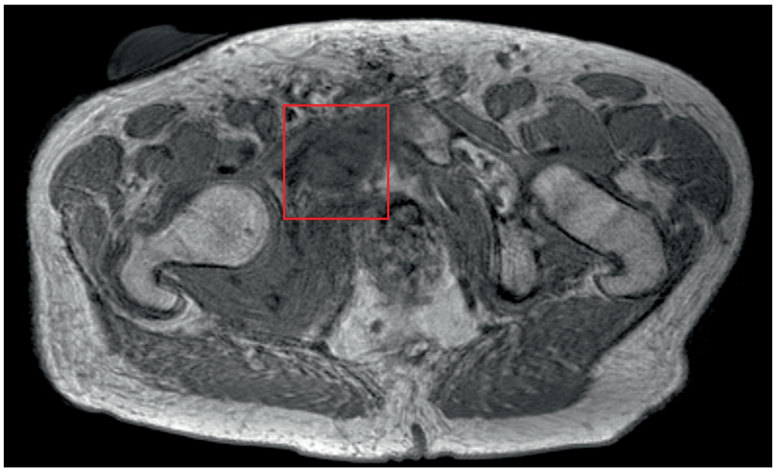

Figure 2.S3: Example of pretreatment MR image with motion artefacts (P1). The lesion is indicated by a red square.

Figure 2.S4: From Figure 2.2, the metastatic tissue is not recognized as osteolytic by the network, but it is instead reconstructed as soft tissue. It has been shown that osteoblastic lesions appear hypointense on the T1- and T2-weighted MRI scans [37] and that they could show signal loss in opposed-phase images [35]. This behavior of sclerosis on MRI may be explained by the short T_2 relaxation time due to dense mineralization of the sclerotic area. This appearance has been observed in the osteoblastic patients in this study. However, in P1, the lesion in the almost opposed phase (TE = 2.1 ms) doesn't show signal loss. This could be explained as in newly formed osteoid, water and fibro vascular tissue predominate when compared to mature sclerosis.

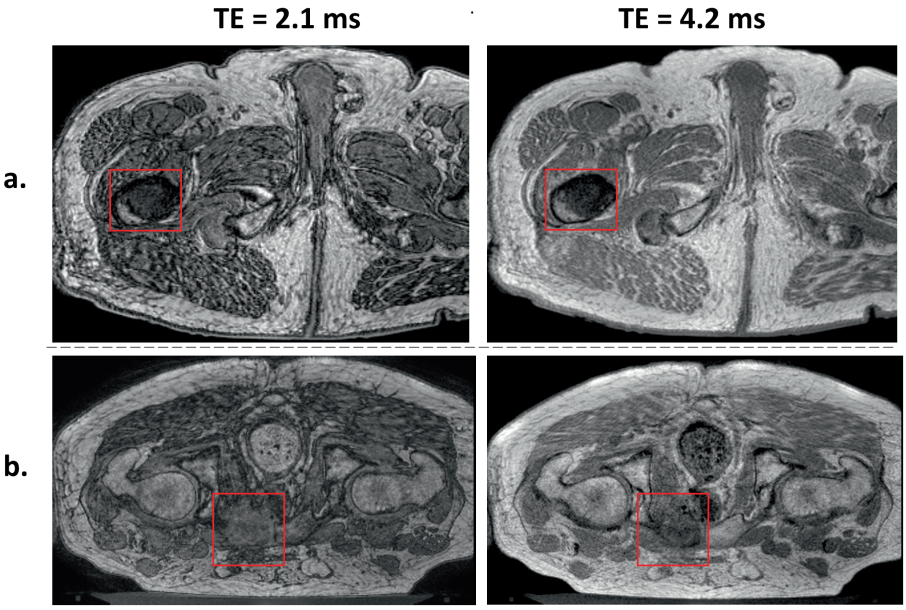

Figure 2.S4: Example of (a) almost in-phase and almost opposed -phase image of most osteoblastic lesions present in the dataset and of (b) almost in-phase and almost opposed-phase image for P9. The lesion is indicated by a red square.

3

RAPID 2D VARIABLE FLIP ANGLE METHOD FOR ACCURATE AND PRECISE T_1 MEASUREMENTS OVER A WIDE RANGE OF T_1 VALUES

Based on:
Lena B., Bos C., Ferrer C.J., Moonen C.T.W., Viergever M.A., Bartels L.W. Rapid 2D variable flip angle method for accurate and precise T_1 measurements over a wide range of T_1 values. *NMR in Biomedicine (2021)*.

"In addition to variations in the transmit RF field, another major source of error in 2D acquisitions is the nonuniform slice excitation profile which causes a large variation in flip angle within every single voxel"

(Svedin B. et al., Medical Physics, 2017) [88]

3

ABSTRACT

Purpose: To perform dynamic T_1 mapping using a 2D Variable Flip Angle (VFA) Method, a correction for the slice profile effect is needed. In this work we investigated the impact of flip angle selection and excitation radio frequency (RF) pulse profile on the performance of slice profile correction when applied to T_1 mapping over a range of T_1 values.

Methods: A correction of the slice profile effect is proposed, based on Bloch simulation of steady state signals. With this correction, Monte Carlo simulations were performed to assess the accuracy and precision of 2D VFA T_1 mapping in the presence of noise, for RF pulses with time-bandwidth products of 2, 3 and 10 and with flip angle pairs between [1°– 90°]. To evaluate its performance over a wide range of T_1, maximum errors were calculated for six T_1 values between 50 ms and 1250 ms. The method was demonstrated in in-vitro and in-vivo experiments.

Results: Without corrections, 2D VFA severely underestimates T_1. Slice profile errors were effectively reduced with the correction based on simulations, both in-vitro and in-vivo. Precision and accuracy of the method depend on the nominal T_1s, the FA pair, and the RF pulse shape. FA pairs leading to <5% errors in T_1 can be identified for the common RF shapes, for T_1 values between 50 ms and 1250 ms.

Conclusion: 2D VFA T_1-mapping with Bloch simulation-based correction can deliver T_1 estimates that are accurate and precise to within 5% over a wide T_1 range.

3.1. INTRODUCTION

An important parameter for magnetic resonance imaging (MRI) studies is the longitudinal relaxation time, T_1. It is an intrinsic tissue property, the value of which depends on the structure of the tissue at a molecular level. Quantitative T_1 mapping may help to noninvasively characterize and discriminate biological tissues. This is of interest for various organs comprising the heart [114, 115], liver and kidney [115], and the brain [116]. Methods based on 3D gradient echo (GRE) acquisitions at either multiple flip angles (FAs) or multiple repetition times (TRs) are used for T_1 mapping [90]. These techniques are usually faster than more conventional T_1-mapping sequences based on inversion recovery [117, 118].

Some applications require rapid time-resolved T_1 mapping. In T_1-based MR thermometry, it is used for temperature mapping, e.g., for monitoring of thermal therapy [4]. In dynamic contrast-enhanced (DCE) MR imaging, it provides input for pharmacokinetic analysis of contrast agent uptake and washout [119, 120]. For these applications, T_1 values may change considerably and rapidly. These changes are monitored through a series of fast repeated sequences in the same scan. For example, for T_1-based MR thermometry in fat during ablation procedures, T_1 values range between 200 and 600 ms [121]. For other dynamic contrast enhanced imaging applications, upper T_1 values of approximately 1200 ms have been reported [122–124]. For such applications, accurate and precise T_1 mapping with an adequate temporal resolution over a wide dynamic range of T_1 values is desired. Here, conventional 3D GRE-based methods are of limited use, because the temporal resolution they offer is typically insufficient. However, the methods can be sped up considerably by switching to 2D acquisition [88, 125].

In 2D, the non-uniform slice excitation profile causes errors in T_1 estimation, as has been shown for the dual-TR T_1-mapping method [125], and for the Variable Flip Angle (VFA) method [88]. Parker et al. proposed a method for simultaneous correction of slice profile effects and B_1 inhomogeneity effects for 2D T_1 mapping with dual-TR gradient echo, which uses T_1-weighted (T_1w) and proton density-weighted (PDw) images [125]. Their correction was based on the time domain simulation of the slice profile, for a range of nominal (i.e., requested by the user on the scanner interface) flip angles and a realistic RF-pulse shape. Their method, implemented for accurate multi-slice scans, was not designed for rapid T_1 mapping: their scan duration was relatively long because of the long repetition times (TR = 1500 ms) needed for the PDw scans.

For 2D VFA T_1 mapping, which uses spoiled gradient recalled (SPGR) images acquired at different FAs, the slice profile and B_1 inhomogeneity effects were simultaneously corrected with a dual-FA approach combined with a FA scaling map by Svedin et al. [88] and with a 3-FAs implementation and a B_1 map acquisition by Dieringer et al. [126].

However, the ability of these methods to correct the slice profile effect for dynamic applications, where T_1 will vary, has not been investigated.

In this chapter, we propose a correction of the slice profile effect for dynamic T_1 mapping applications, based on a look-up table (LUT) of nominal T_1 values and simulated apparent T_1s. Here, we investigated the performance of 2D VFA T_1 mapping including the correction over a wide range of T_1s. Moreover, we will study the impact of flip angle selection and excitation RF profile on the performance of the method, in terms of accuracy and precision.

3.2. THEORY

3.2.1. T_1 MAPPING USING THE VARIABLE FLIP ANGLE METHOD

The conventional 3D VFA T_1 mapping method, was proposed by Homer et al. [127]. It is based on a 3D Radio Frequency (RF) spoiled Gradient Echo (SPGR) sequence, the steady state signal of which is described by:

$$S \propto M_0 \frac{(1-E_1)sin\theta}{1-E_1 cos\theta} E_2 \tag{3.1}$$

where M_0 is the equilibrium magnetization, θ the flip angle, E_1 is defined as $\exp -TR/T_1$, E_2 as $\exp -TE/T_2^*$ [2].
Equation 3.1 can be written in a linearized form [90, 128]:

$$\frac{S}{sin\theta} = E_1 \frac{S}{tan\theta} + M_0(1-E_1) \tag{3.2}$$

which allows to estimate T_1 from the signal measurements at multiple flip angles, by determining the slope k of $S/sin\theta$ vs $S/tan\theta$ to obtain E_1.
To determine the slope, measuring the signal for at least two flip angles is required. The choice of flip angles will influence the performance of the method. It has been shown empirically [90] and analytically [129] that a flip angle pair can be found that maximizes T_1 measurement precision.

3.2.2. CORRECTION OF 2D VFA T_1 MAPPING

Truncation and apodization of RF pulses lead to deviations from the optimal rectangular slice profile [88, 125], causing non-uniform excitation in the slice selection direction. In 3D VFA, this problem is solved by phase encoding in the slice direction and excluding the partitions near the edges of the slab. In 2D, however, these slice profile effects will lead to errors in T_1 values estimated using the VFA method [88].
We propose an approach to estimate 2D VFA T_1 maps corrected for the non-uniform excitation effect, considering the full slice profile. We neglect partial volume effects by assuming that each voxel can be assigned a single T_1 value. The response of the magnetization to an excitation pulse can be described by Bloch's equations. The available magnetization at an angular frequency ω' in the rotating frame of reference, represented by $M(\omega', t)$is initially aligned with the $\mathbf{B_0}$ field, along the z-axis ($M_0 = (0,0,1)^T$). Then, it is rotated by the B_1 field of the RF pulse towards the transverse plane over a certain flip angle θ. For a circularly polarized RF field in the transverse plane, defined as $\mathbf{B_1} = \mathbf{B_1}(\mathbf{t})\hat{\mathbf{y}}'$, the motion of the magnetization in the rotating frame is described by:

$$\frac{d\mathbf{M}(\omega', t)}{dt} = \gamma \mathbf{M}(\omega', t) \times \mathbf{B}(\omega', t) \tag{3.3}$$

where

$$\mathbf{B}(\omega', t) = (0, B_1(t), \frac{\omega'}{\gamma})^T \tag{3.4}$$

(neglecting T_1 and T2 decay during the RF pulse). Thus, for a specific RF pulse ($B_1(t)$), the magnetization is obtained by integrating Equation 3.3 over time. From the resulting

magnetization, the actual flip angle $\theta(\omega')$ at a frequency ω' is calculated:

$$\theta(\omega') = tan^{-1} \frac{\sqrt{M_x(\omega')^2 + M_y(\omega')^2}}{M_z(\omega')} \tag{3.5}$$

where $M_x(\omega')$, $M_y(\omega')$ and $M_z(\omega')$ are the x, y and z components of the magnetization vector. The phase $\varphi(\omega')$ of the transverse magnetization for that frequency ω' is given by:

$$\varphi(\omega') = tan^{-1} \frac{M_y(\omega')}{M_x(\omega')} \tag{3.6}$$

Finally, the complex demodulated steady state signal is obtained by discrete summation of all magnetization vectors over a frequency range 6 times the bandwidth of the pulse, to include all the relevant side lobes:

$$\hat{S} = M_0 \sum_{n=1}^{N} \frac{(1 - E_1) sin\theta(\omega'_n)}{1 - E_1 cos\theta(\omega'_n)} e^{i\varphi(\omega'_n)} \tag{3.7}$$

where N is the number of frequency bins. To determine the relation between nominal (i.e., prescribed as input) T_1 values and T_1 estimated with 2D VFA mapping, simulations were performed for a range of nominal flip angles and for three commonly used RF pulse shapes. For an input value T_1 and two nominal FAs, the steady state signals were calculated with Equation 3.7 and used to find the apparent longitudinal relaxation time $\hat{T}_1$ using the conventional Variable Flip Angle T_1 estimation applied to the 2D VFA data, from the slope in Equation 3.2. In this way, $\hat{T}_1$ includes the effects of the non-uniform slice excitation in case of 2D acquisition (Figure 3.1-I). Finally, by repeating the simulation for a range of T_1 values a look-up table was created for $\hat{T}_1$ versus the nominal T_1. In the correction step of our method, this table is used to relate measured $\hat{T}_1$ values to the nominal T_1 values. The look-up table needs to be computed for the TR value and RF shape used in the VFA pulse sequence.

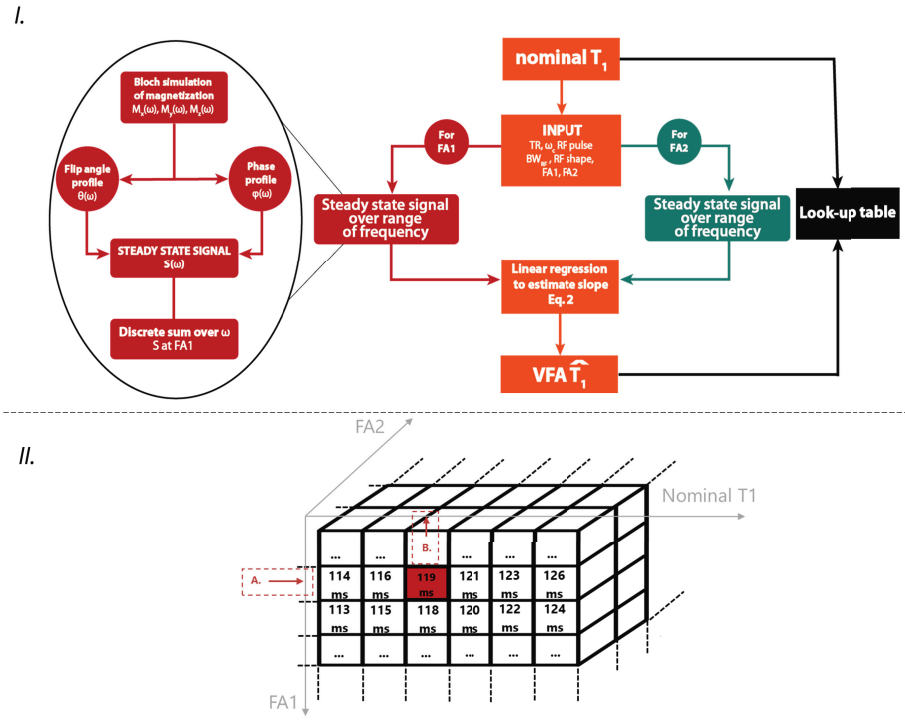

Figure 3.1: I. Flowchart of building the T_1 LUT. For each nominal the steady state signal is simulated for two nominal FAs. From the simulated signals, the apparent $\hat{T}_1$ is computed using the VFA method. The values of apparent $\hat{T}_1$ are then inserted in the table for comparison with the corresponding nominal T_1. II. LUT structure and correction procedure. The LUT is indexed by the FA pair and nominal T_1. LUT entries are apparent $\hat{T}_1$ for each combination of FA1, FA2, nominal T_1. In case of B_1+ correction the nominal FA is scaled to actual FA in the voxel. At this FA pair (Arrow A.) the apparent T_1 is matched to entries of the LUT and the corresponding nominal T_1 is looked up (Arrow B.).

3.3. METHODS

We build the look-up tables of T_1 values for three commonly used RF pulse modulations (5 central lobes of a SINC, asymmetric lobe of a SINC, Gaussian). To maintain a comparable slice thickness, all RF pulses had the same bandwidth and different durations. Each RF pulse had a specific time-bandwidth product (TBP): The SINC pulse had TBP 10, the asymmetric SINC pulse TBP 3 and the Gaussian pulse TBP 2 (Figure 3.2).

The LUT is a multidimensional array containing the calculated apparent T_1 values i.e., the T_1 values that would be measured in the presence of the slice profile effect, indexed by FA1, FA2 and nominal T_1 (Figure 3.1-II). FA values ranged between 1° and 90° with 1° step size and the nominal T_1 between 50 and 1500 ms, with 1 ms steps, yielding a total of 1450 values. The LUT had $90 \times 90 \times 1450$ entries, but it could be expanded to include TR and/or TBP, if necessary. To build the LUT, simulations were performed with TR 10 ms, slice thickness 7 mm, for every combination of two flip angles, namely FA1 and FA2, between 1° and 90°, with 1° steps; the MR parameter settings in the simulation were as in the MR experiments (see Table 3.1). The RF duration, RF B_1 amplitude and

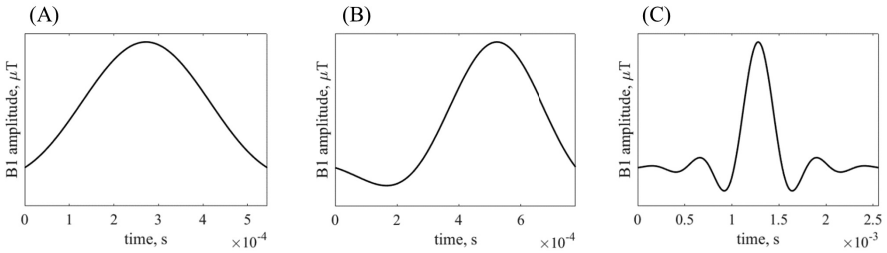

Figure 3.2: RF pulse shapes considered: Gaussian RF pulse, TBP 2 (a), Asymmetric lobe of a SINC pulse, TBP 3 (b) 5 central lobes of a SINC pulse, TBP 10 (c). In the simulations, slice thickness and RF bandwidth were maintained constant, whereas RF pulse duration was changed.

slice selection gradient strength were obtained by taking the values used by the MRI scanner for FA = 90° and subsequent rescaling for the FA considered.

Table 3.1: Imaging protocol for 2D- and 3D- VFA scans. The VFA sequence consists of two SPGR scan at flip angles 6°, 40°.

2D VFA scan		**3D VFA scan**	
Type	SPGR	Type	SPGR
Scan mode	2D	Scan mode	3D
RF pulse	Sinc Gauss, TBP 3	RF pulse	Sinc Gauss, TBP 10
TR	10 ms	TR	10 ms
TE	4.6 ms	TE	4.6 ms
FA	6°, 40°	FA	6°, 40°
Water fat shift	1.6 pixels	Water fat shift	1.6 pixels
Dynamic scan duration	2.2 s	Number of slices	7
Dummy scans	200	FOV	112 × 112
FOV	112 × 112	Voxel size	2 × 2 × 7
Voxel size	2 × 2 × 7	RF-spoiling	117°
RF-spoiling	117°	phase increment	
phase increment			

3.3.1. APPLICABILITY OF THE LINEARIZATION IN THE 2D VFA METHOD

The VFA method is based on the linearization of the steady state signal equation (Equation 3.2) to estimate T_1. In order to investigate whether this assumption still holds with non-uniform slice excitation, the behavior of $S/sin(\theta)$ vs $S/tan(\theta)$ as a function of the flip angles used (i.e., between 1° and 90°) was studied for nominal T_1s from 50 ms to 1250 ms. The signals for 3 RF shapes at different nominal T_1 values was simulated, as described in Section 3.2.2. No correction with T_1 look-up tables was applied at this stage.

3.3.2. PERFORMANCE OF 2D VFA T_1 MAPPING (OVER A RANGE OF FAS)

In order to assess the dependence of accuracy and precision of 2D VFA T_1-mapping with our proposed correction on the flip angle choice, white Gaussian noise was added

to the simulated 2D complex steady state signals, with standard deviation of the noise distribution equal to 1 and the equilibrium magnetization M_0 equal to 1000, resulting in a realistic SNR of 30 – 150 for T_1 = 250 ms. T_1 values were then computed from the noisy signals varying both FAs in the range from 1° to 90° with 1° increments. The simulation was repeated 1000 times with TR = 10 ms, for six T_1 values equal to 50 ms, 250 ms, 500 ms, 750 ms, 1000 ms and 1250 ms.

The accuracy of the 2D VFA T_1-mapping method with slice profile correction was evaluated for each combination of flip angles as the relative difference between the noisy T_1 estimates ($T_{1,estim}$) and the nominal T_1 ($T_{1,nom}$):

$$\epsilon(FA1, FA2, T_1) = 1/N \sum_{n=1}^{N} \frac{T_{1,i,estim} - T_{1,nom}}{T_{1,nom}} \times 100\% \tag{3.8}$$

where is the number of simulations. To evaluate the effect of the slice profile correction, the accuracy was evaluated with and without the correction. Similarly, the precision of the VFA T_1 mapping method was evaluated using the relative T_1 standard deviation (σ_{T_1}):

$$\sigma(FA1, FA2, T_1) = \frac{\sqrt{1/N \sum_{n=1}^{N} (T_{1,i,estim} - < T_1 >)^2}}{< T_1 >} \times 100\% \tag{3.9}$$

where $< T_1 >$ is the average value of the T_1 estimates and N is the number of simulations. To evaluate the performance of the VFA method across a T_1 range, maximum error projections (MEPs) were taken through $\epsilon(FA1, FA2, T_1)$ and $\sigma(FA1, FA2, T_1)$ volumes along the T_1 dimension. We then identified the region of FA pairs for which the MEPs of $\epsilon(T_1)$ and $\sigma(T_1)$ were below 5%.

3.3.3. EXPERIMENTAL VALIDATION

To investigate the performance of the correction method, both phantom and human volunteer experiments were performed on a clinical 1.5-T MR scanner (Philips Achieva, Best, The Netherlands) using the integrated body coil as transmitter and an 8-channel head coil as a receiver. All image processing and all analyses were done offline using MatLab 2018a (Mathworks, Natick, MA).

IN-VITRO VALIDATION OF THE 2D T_1-MAPPING CORRECTION

To evaluate T_1 mapping with 2D VFA, a validation of the method was performed in a phantom. The phantom experiments were performed on a calibrated phantom consisting of gel tubes with T_1 known to within ±3% accuracy (TO5, Eurospin II test system, Scotland). Eleven tubes with nominal T_1 values in the range of 200-1250 ms were placed on a polystyrene foam holder and scanned at 21°C.

Reference T_1 values were obtained from a 2D turbo inversion recovery (IR) spin-echo scan, with the following acquisition parameter settings: Repetition Time (TR) = 7000 ms, Echo Time (TE) = 20 ms, Matrix = 112 × 112, and variable Inversion Time (TI) = [50, 100, 200, 400, 800, 1600, 3200] ms. T_1 was calculated using the following non-linear least squares three-parameter fit function:

$$M_z(TI) = M_0[(1 - cos\theta_{inv})e^{-TI/T_1} + e^{-TR/T_1}] \tag{3.10}$$

where the three parameters fitted were the equilibrium magnetization M_0, the T_1 and the flip angle of the inversion angle θ_{inv}. Phase errors have been corrected with the method proposed by Xiang et al. [130].
For the VFA experiments, a 2D SPGR sequence was used with the parameter settings reported in Table 3.1. The RF pulse was an asymmetric SINC-gauss pulse with TBP 3, a pulse commonly used for 2D SPGR sequences.
T_1 maps were estimated with the VFA method and then corrected for slice profile effects. The relative error in T_1 estimation relative to the reference values obtained with Inversion Recovery was defined as:

$$\epsilon_{T_1} = \frac{T_{1,VFA} - T_{1,IR}}{T_{1,IR}} \times 100\% \tag{3.11}$$

where $T_{1,VFA}$ are the T_1 values estimated with 2D VFA mapping and $T_{1,IR}$ are the reference T_1 values from the IR experiment. A correction for in-plane B_1 inhomogeneities was applied. The relative error in T_1 estimates corrected for B_1 inhomogeneities was compared to the relative error without this correction. In-plane B_1 inhomogeneities were corrected using B_1 maps, acquired using the Actual Flip-angle Imaging method [131]:TR_1 30 ms, TR_2 150 ms, TE 4.40 ms, FA 60°.
The B_1 correction was applied prior to correction for the slice profile effects, as follows: the actual FA in each voxel was calculated by rescaling the nominal FA using the B_1 value for that voxel. Next, the LUT indexed by the actual FA pair in each voxel was used to correct for the slice profile effect (Figure 3.1-I).
The quantitative evaluation was based on a region of interest (ROI) placed at the center of each tube and the spatial error was assessed using the spatial standard deviation of the T_1 maps over the voxels inside the ROI.

IN-VIVO DEMONSTRATION OF THE 2D T_1-MAPPING CORRECTION

To demonstrate the method in vivo, experiments were performed in the brain of two healthy volunteers. The volunteer study was performed with the approval of the institutional review board of the University Medical Center Utrecht (NL53099.041.15), and written informed consent was obtained from the volunteer.
Experimental T_1 maps were calculated from single-slice 2D- and 3D- VFA acquisitions (Table 3.1). The parameter settings for the 2D-VFA scans and B_1 maps were the same as those for the phantom study. The qualitative evaluation was assessed comparing 2D T_1 maps with and without the slice profile correction with 3D T_1 maps. For 3D-VFA scans, the analysis has been performed on the central slice of the volume.

3.4. RESULTS

The flip angle, phase and magnetization profiles across a range of frequencies for the three RF pulses considered are shown in the supplementary material Figures 3.S1-3.S2, along with the signal vs FA curves for TBP 2, 3, and 10.

3.4.1. APPLICABILITY OF THE LINEARIZATION IN THE 2D VFA METHOD

Figure 3.3 shows the plots of $S/sin(\theta)$ vs $S/tan(\theta)$ for RF pulses with TBP 2, 3 and 10. Slice profile effects in 2D VFA cause deviations some from linearity for all TBP's. Yet,

TBP 2 and 3 show more linear behavior than TBP 10, especially at long T_1 and high FAs. The deviation from linearity leads to a change of the slope (k) as a function of the FA combination, as shown in Figure 3.4 with a fixed FA1 for T_1 = 300 and 1000 ms. The natural logarithm of the slope (ln(k)) is negative for all combinations of FAs with TBP 2 and 3, whereas it increases at higher FAs for TBP 10 and becomes positive especially with long T_1. When ln(k) at high FA becomes positive, the T_1s estimated with the VFA method turn negative, which is unrealistic, and also the slice profile correction using the LUT will fail.

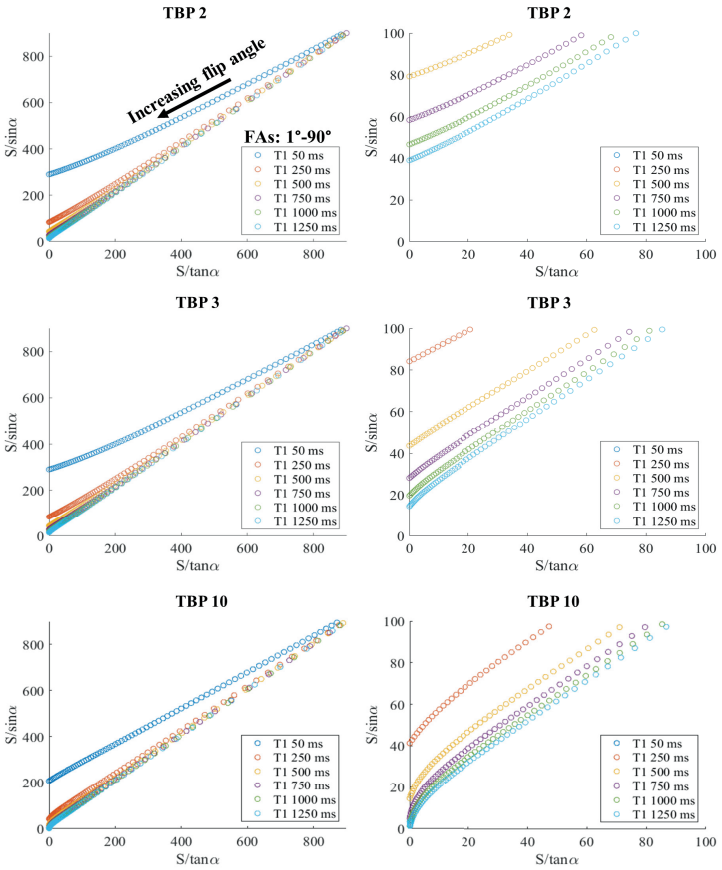

Figure 3.3: Plot of $S/sin(\theta)$ vs $S/tan(\theta)$ for simulated steady state signals with RF pulses with TBP 2, 3, 10, TR = 10 ms and T_1 = 50, 250, 500, 750, 1000 and 1250 ms. The high FAs lie closer to the origin of the graphs, as indicated by the arrow. The right column shows a magnified view to detail the behavior at high FA.

3.4.2. PERFORMANCE OF 2D VFA T_1 MAPPING (OVER A RANGE OF FAS)

Figure 3.5a shows the simulated T_1 estimates calculated without slice profile correction as a percentage of the true T_1. For nearly all flip angles, the VFA method without correction for the slice profile severely underestimates T_1. When the correction with

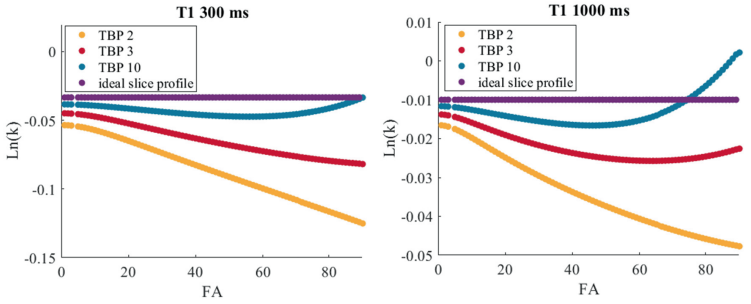

Figure 3.4: Plot of the natural logarithm of k, for TBP 2, 3, 10 and the ideal case without slice profile effects, with fixed FA1 = 4°, TR = 10 ms, and with T_1 = 300 ms (left frame) and 1000 ms (right frame).

the T_1-LUT is applied, the error in the T_1 estimate was effectively reduced, as Figure 3.5b shows. For example, at T_1 = 500 ms and an RF shape with TBP 3, a large range of FA pairs has $\epsilon_{T_1} < 5\%$ after correction.

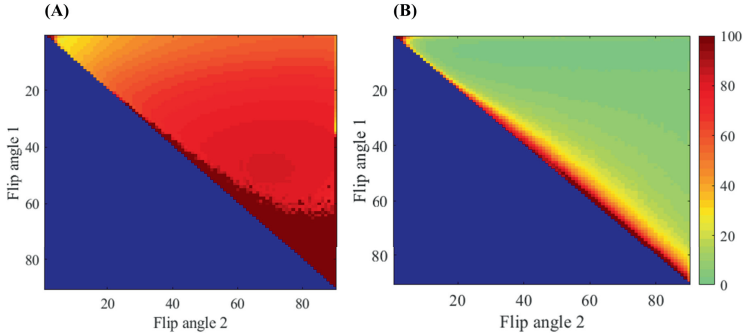

Figure 3.5: Relative error in 2D VFA T_1-mapping as a function of FA combination, without (a) and with (b) the T_1 correction with LUT. Data is shown for a single T_1 of 500 ms. Simulation input: RF pulse with TBP 3 nominal T_1 500 ms and TR 10 ms. NOTE: because of symmetry, only half of the FA combinations is presented.

An overview of the relative error ϵ_{T_1} and standard deviation σ_{T_1} is presented in Figure 3.6, for T_1 values across the range examined. The number of FA pairs with an acceptable (i.e., below <5%) ϵ_{T_1} and σ_{T_1} decreases as the nominal T_1 increases. The flip angle pairs that gave the highest accuracy (in 3.6a) and precision (in 3.6b), i.e., minimum ϵ_{T_1} and σ_{T_1}, are marked with a blue cross: as expected, they are dependent on the T_1 value. Moreover, as shown in Figure 3.6b, they differ from the flip angles calculated using the method proposed by Deoni et al. for 3D VFA [90, 129]. Typically, the minima occur for higher flip angles than the ones calculated for 3D VFA for a given T_1.
In Figure 3.7, the MEPs of ϵ_{T_1} and σ_{T_1} along the T_1 axes are shown for the 3 RF pulses. The precision and accuracy of 2D VFA T_1-mapping depend also on the RF pulses applied. Areas of FA pairs accurate within 5% and with precision better than 5% can be identified for all RF shapes, see Figure 3.7c: for some combinations of FAs,

Figure 3.6: Relative error ε_{T_1} (a) and relative standard deviation σ_{T_1} (b) in 2D VFA T_1-mapping, as a function of the flip angle combination chosen and applied to different nominal T_1. Results are for one pulse shape, and after correction using the lookup table. Simulation input: TBP: 3, nominal T_1: 50, 250, 500, 750, 1000 and 1250 ms and TR = 10 ms. The blue crosses show the minimum for each nominal T_1. For (b), the FA pair calculated using Deoni's method [90] are indicated with a red +. NOTE: color scale is different from Figure 3.5.

the two areas overlap. Moreover, errors in the T_1 estimations increase with the TBP of the RF pulse. The RF pulses with TBP 2,3 have the largest FA area where $\epsilon_{T1,max}$ and $\sigma_{T1,max}$ are below 5%. This is somewhat surprising, since these pulses have the slice profiles that deviate most from the boxcar shape.

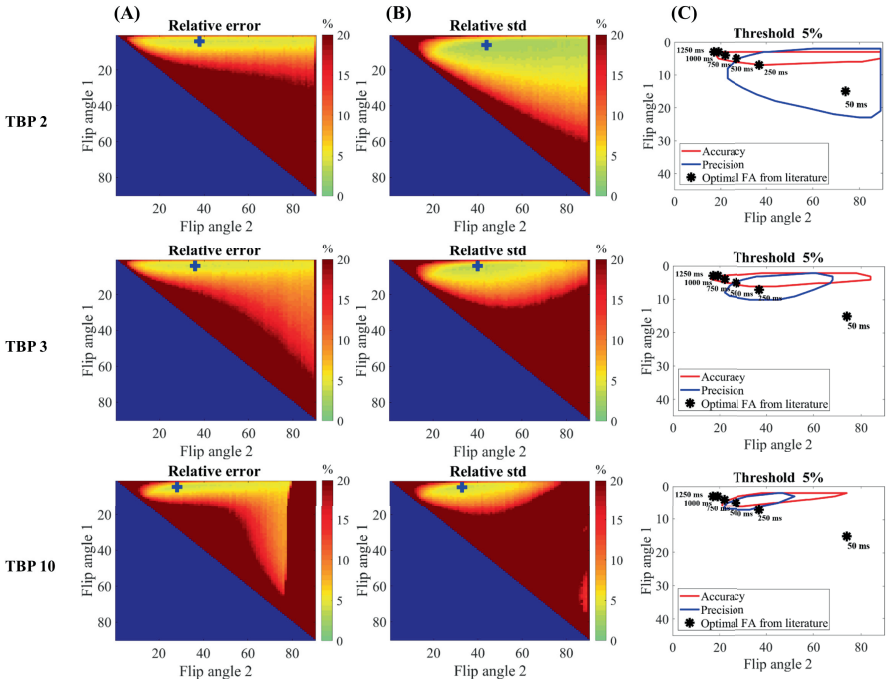

Figure 3.7: Performance of 2D VFA T_1-mapping for a range of T_1, using RF pulses with different TBP. Maps of maximum relative error $\epsilon_{T1,max}$ (a) and relative standard deviation $\sigma_{T1,max}$ (b) over 6 nominal T_1 values: the value in each location is calculated as the maximum projection over 6 nominal T_1. The blue + show the minima identified for the whole T_1 range. Contour plot identifying combinations of FA for which $\epsilon_{T1,max}$ and $\sigma_{T1,max}$ are 5% on the contour and below 5% inside (c); the FA pair, calculated using Deoni's method [90], are also reported as black for the single nominal T_1s. NOTE: the scale for FA1 in (c) is different.

3.4.3. EXPERIMENTAL VALIDATION

IN-VITRO VALIDATION OF THE 2D T_1-MAPPING CORRECTION

Figure 3.8 shows the T_1 value for each tube estimated with 2D VFA with and without corrections for slice profile effects and B_1 inhomogeneities. T_1 values estimated from each tube with and without slice profile correction and B_1 correction are summarized in Table 3.S1. Without corrections, the VFA method underestimates T_1s with 40-60% error (average error: -51.4%). The T_1 underestimation is reduced to 5%-12% with the slice profile correction (average error: -8%). The B_1 scaling factors in the tubes were between 0.91 and 0.95 (average: 0.93). The application of B_1 correction leads to a slight T_1 overestimation: range 2% to 12% (average error: 7%).

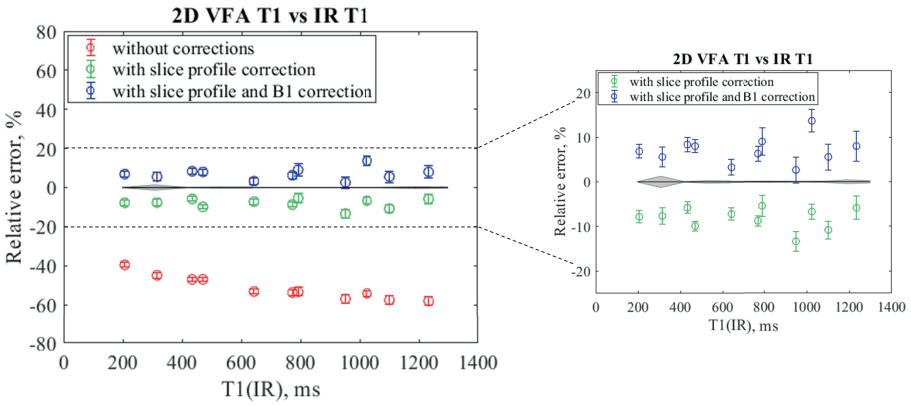

Figure 3.8: Relative error in T_1 estimation as a function of T_1. The relative errors were evaluated in 30-pixel ROIs at the center of each tube (Images acquired with TBP 3; nominal FA 6°, 40°). The 2D VFA estimates are reported without corrections (in red), with slice profile correction (in green) and with both slice profile and B_1 correction (in blue). The grey band represents the standard deviation of the IR T_1 estimation.

IN-VIVO DEMONSTRATION OF THE 2D T_1-MAPPING CORRECTION

Figure 3.9 shows the results of a comparison of T_1 maps calculated with the VFA method for the human brain at 1.5 T. For both volunteers, 2D T_1 maps without slice profile correction show T_1 underestimation in all tissues, when compared to the 3D T_1 maps. This underestimation was reduced by applying the slice profile correction. Slice profile-corrected 2D T_1 maps are generally in agreement with the 3D T_1 maps.

3.5. DISCUSSION

We have shown that 2D VFA T_1 mapping with correction for slice profile effects can deliver accurate and precise T_1 estimates within 5% error, over a large range of T_1 values (50-1250 ms). We observed that both the accuracy and the precision of such 2D VFA T_1 measurements are dependent on the two flip angles used. Moreover, also the RF pulse shape was found to have an influence on T_1 accuracy and precision. Simulations showed that for an RF pulse shape with lower TBP (i.e., the flip angle profile differs more from a boxcar function), a larger range of FA combinations can be used to arrive at accurate and precise T_1 estimates can be used. For RF pulses with a high TBP, a bias in T_1 estimation compromises the performance of the method for high flip angles.
In previous studies, it was shown that in order to maximize T_1 precision, the best choice for FAs depends on the value of T_1 [90, 129]. Since for dynamic T_1 applications good performance over a range of T_1s is needed, we investigated the accuracy and precision of 2D VFA over a T_1 range for all (relevant) FA combinations. In this study, we demonstrate that it is possible to choose FA pairs resulting in acceptable <5% errors for the full range of T_1s, from 50 ms to 1250 ms. This means that objects containing tissues with large T_1 differences or for which T_1 changes over time, can be measured using a fixed flip angle pair. Moreover, we identified the limits of applicability of this 2D VFA method: it was found that as T_1 increases, the VFA method provides realistic T_1 estimates only in the low FA regime.

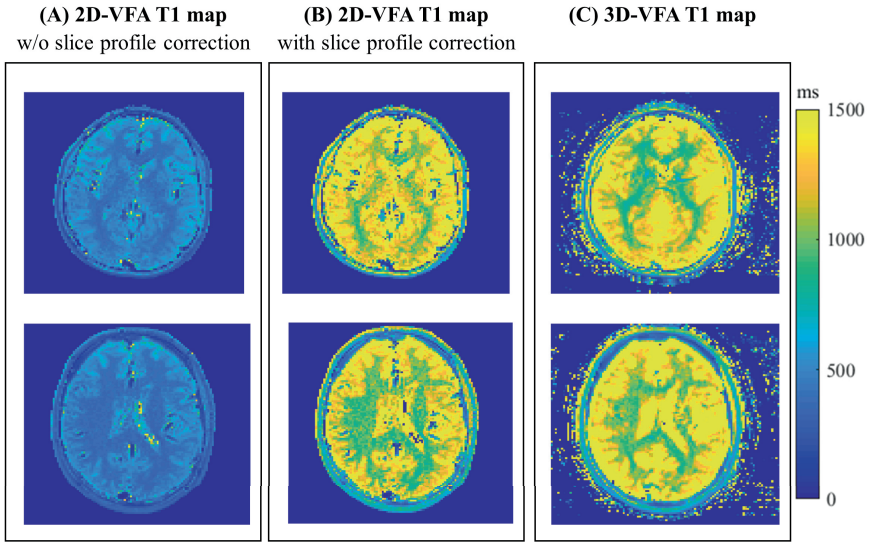

Figure 3.9: Estimated T_1 maps of a transverse slice in the brain of two volunteers (Images acquired with TBP 3; nominal FA 6°, 40°). The T_1 maps have been estimated with the 2D VFA method without (a) and with slice profile correction (b), and with the 3D VFA method (c). All the maps have been corrected for B_1 inhomogeneities.

Conceptually, this approach to T_1 quantification and the correction of the 2D slice profile effects presents some similarities with MR fingerprinting (MRF) [132]. In MRF, a signal dictionary is generated by modelling the spin behavior during the acquisition for a variety of acquisition strategies, such as balanced Steady-State Free Precession (bSSFP), Fast Imaging with Steady State Precession (FISP), RF-spoiled GRE, GRE sampling of the FID and Spin Echo (SE) sequence [132]. Although the MRF framework has shown potential for multi-parameter estimations, it is limited in terms of temporal resolution when only a specific single property (in this case, T_1) is required, as the matching procedure depends on the dictionary size and the number of voxels. In our 2D VFA method, the look-up table serves as a strongly conditioned dictionary that is. calculated once prior to the experiment. For performance reasons, it is possible to further reduce its size and only include FAs close to the nominal FA, to accommodate for B_1 inhomogeneities.
Another similar application to our approach is T2 mapping with multi-echo (ME) spin-echo (SE) sequences: this approach relies on a database of simulated echo modulation curves (EMC) for a range of T2s in a multi-spin-echo experiment, to correct for the signal contamination from stimulated and indirect echoes present with these schemes [133]. Similarly, in our case, we implemented an algorithm using Bloch simulations in order to generate the steady state signals for the 2D VFA method.
Previously, a method to correct 2D VFA T_1 mapping both for the slice profile effect and the variations in the RF transmit field has been proposed [78, 88]. The correction was based on an average flip angle assumption and required an initial T_1 estimate. This approach was tested for MR thermometry studies [78] and its properties were studied through simulation and experiments for few set T_1 values [88]. The flip angle and the

RF shape were found to have an influence on the performance of this method. In their paper, Svedin et al concluded that the area of accurate flip angle combinations widens with TBP of the RF pulse [88].
In the present study, we proposed and investigated a correction for the 2D slice profile effect, based on simulation only, including the full slice profile for the FAs chosen. Similar to Svedin, we found that FAs and TBP of the RF pulses influence accuracy and precision of our correction. However, in contrast to Svedin, our simulations showed that for more ideal RF pulse shapes, a smaller range of FA pairs can be used to compute acceptable T_1 estimates. This can be explained studying the behavior of $S/sin\theta$ vs $S/tan\theta$ as the FA increases. The VFA method is based on the linearization of the steady state equation (Equation 3.2) and estimates T_1 from the slope of this line. However, with higher TBP, deviations from linearity can be identified at high FAs. Since the curve is no longer a straight line, the slope is not constant and T_1 estimation through the VFA method will be compromised. Moreover, for high TBP pulses the signal is low at high flip angles (see Figure 3.S2), which in turn results in a low SNR. This has an effect on the precision of T_1 measurements. To overcome this problem, the signal could be acquired at low FAs, aiming for a compromise between SNR and VFA method accuracy.
Moreover, we compared the FA pair calculated from previous studies for 3D VFA [90, 129] with the ones that minimized the relative standard deviation in T_1 for the Gaussian and the SINC pulses. We found that when an RF shape with highly uniform slice profile is considered, the optimal flip angle pair and the pair calculated with methods from the literature [90, 129] show good agreement. This is understandable, since these previous studies derived and investigated FA pairs for the 3D VFA method, for which the non-uniform slice excitation is resolved through phase encoding in slice-direction. For the 3D case, it is possible to identify a pair of FA which maximizes T_1 precision for a specific T_1 [90]. In 2D, the relatively uniform slice profile offered by high TBP pulses approaches this ideal case, which could be advantageous when measuring an approximately known T_1. For dynamic T_1 applications, however, rapid changes should be detected over a substantial T_1 range. In this case, we found that the low TBP pulses, which deviate more from an ideal boxcar slice profile, are more forgiving and therefore more suitable for applications where T_1 is unknown.
For 2D VFA, the FAs that minimize errors are both higher for lower TBP. The shift in the higher FA (FA2) is greater. A possible explanation is an increased contribution from parts of the signal profile with lower effective flip angle for these low TBP pulses.
We observed from Figure 3.7c, that with the FA pair estimated with Deoni's method [90] for T_1 = 250 ms (approximately, the T_1 of fat at 20 °C at 1.5 T), errors in T_1 estimation for a wide range of T_1s are less than 5% with all the RF pulses considered. This could be relevant for other applications with dynamic changes in T_1 in adipose tissues, such as MR thermometry in fat. For example, with thermal therapy, e.g., MR-guided High-intensity Focused Ultrasound (MR-HIFU), fat can be heated up to 70°C, and its T_1 value may reach ≈ 600 ms. Another application involving rapid T_1 changes is DCE imaging of the breast [123].
Although we have studied the accuracy and precision of T_1 estimation using the 2D VFA method for different RF shapes and over a range of T_1 values, some factors limit the generalizability of this approach. First, we assumed single T_1 values per voxel. It

would be interesting to study the influence of partial volume effect in mixed voxels. Moreover, the assumption of a single relaxation component does not hold for a variety of biological tissues, like human white matter and grey matter. It has been shown that the SPGR signal in the brain is more completely characterized by a summation of two or more relaxation components, arising from a fast relaxing (due to myelin) and a slow relaxing species [134, 135].

In our phantom study we observed differences between the VFA T_1 estimates with slice profile and B_1 corrections and the reference T_1 estimates from IR. The VFA method is known to overestimate T_1 values [136, 137]. A number of causes for this have been reported, including incomplete spoiling of the transverse magnetization in SPGR sequences [138] and improper accounting for noise in the VFA fitting [139], and the variation of the flip angle within the body, caused by inhomogeneities in the RF transmit field [136]. Moreover, it has been shown that even small B_1 variations (i.e., less than 10%, as our case), can result in considerable bias in accuracy in T_1 values, estimated with VFA method [136].

In our experiments, performed at 1.5 T, we found that slice profile correction addresses most of the bias in T_1 estimation, whereas the impact of B_1 error was less significant. In applications where time-resolved scanning is used to measure dynamic changes in T_1, such as with T_1-based MR thermometry, B_1 correction may be optional. However, B_1 inhomogeneities worsen at higher field strengths.

In addition, the VFA method assumes that magnetization is in steady state (i.e., the signal behaves as described in Equation 3.1). This is typically accomplished by setting a proper RF-spoiling phase increment and including a sufficient number of dummy pulses to account for the time lost by transitioning between the steady states belonging to FA1 and FA2.

Lastly, as mentioned, it is known that incomplete elimination of the transverse magnetization in SPGR sequences can be a source of T_1 measurement errors [138]. At this stage, our simulations assumed perfect spoiling, which may not always be achieved in practice.

3.6. CONCLUSION

We proposed a correction for non-uniform 2D slice excitation in 2D VFA-T_1 mapping. The correction is based on Bloch simulation of the magnetization over the full slice profile for common RF waveforms. We have shown that accurate and precise 2D VFA measurements over a large range of T_1 values can be obtained with this correction. We studied the influence of FAs and RF shape on the 2D VFA method and we found that a larger area of FA pair with acceptable (<5%) errors in T_1 accuracy and precision is available for RF pulses with low TBP.

3.7. SUPPLEMENTARY MATERIALS

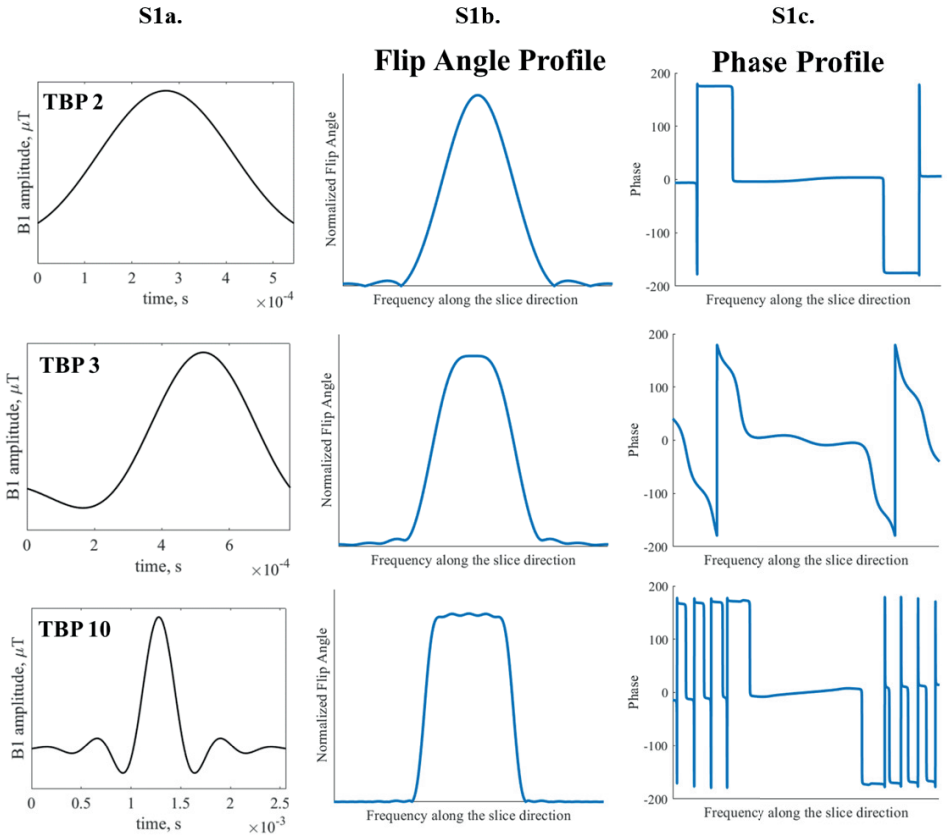

Figure 3.S1: Flip Angle (S1b) and Phase profile (S1c) at 40° flip angle, T1 = 250 ms, for Gaussian RF pulse, Asymmetric SINC pulse and SINC pulse, reported in (S1a).

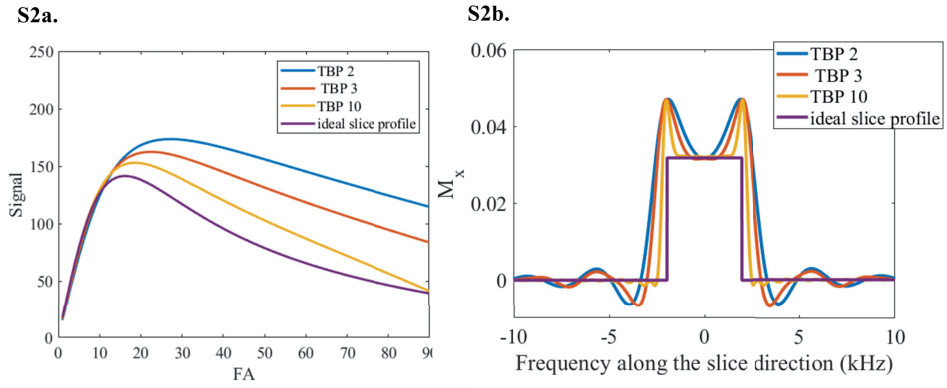

Figure 3.S2: (S2a) Signal as a function of flip angle. Comparison of the simulated steady state signals for TBP 2, 3 and 10, with the theoretical behavior of the steady state signal, as it would be generated by an RF pulse with ideal slice profile (i.e. rectangular slice profile, Equation 3.1) for T1 = 250 ms. (S2b) Real component of magnetization Mx as a function of frequency at 40° flip angle.

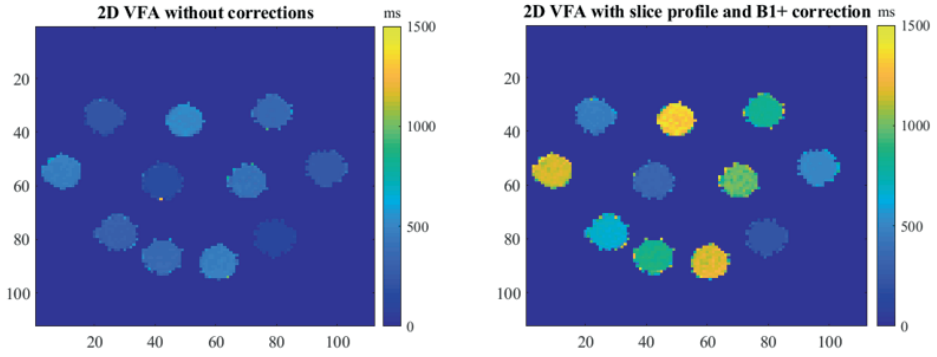

Figure 3.S3: T1 maps from the in vitro experiment with and without the slice profile and the B1 correction.

Table 3.S1: T1s in tubes estimated with 2D VFA method compared to reference values from IR experiment, with and without correction for the slice profile effect and B1 mapping correction. All the estimates are reported in ms.

IR T_1	IR σ_{T_1}	2D-VFA T_1 no correction	2D-VFA σ_{T_1} no correction	2D-VFA T_1 slice profile corrected	2D-VFA σ_{T_1} slice profile corrected	2D-VFA T_1 slice profile + B1 corrected	2D-VFA σ_{T_1} slice profile + B1 corrected
206	0.5	124.5	1.4	189.9	2.8	220.1	3
314.9	0.7	173.5	2.7	290.8	5.8	332.4	6.7
433.1	0.2	229.5	2.6	408	5.6	469.3	6.7
469.5	0.6	249	2.9	423.1	5.1	507.1	6.9
641.8	0.8	300.5	3.9	595.6	9.1	662.7	11.1
771.1	0.6	356.5	4.9	703.8	8.8	819.6	12.8
790.6	1	369.1	8.1	747.9	18.7	862	24.1
950.2	1.9	408.61	8.9	823.2	21.1	975.1	27.4
1024.9	2.8	468.1	9.8	956.4	16.8	1163.1	31.6
1102	4.4	470.2	6.9	982.8	21.5	1164.9	25.9
1234.6	15.6	517.7	11.5	1162.5	28.7	1333.5	37.7

4

INTERLEAVED WATER AND FAT MR THERMOMETRY FOR MONITORING HIFU ABLATION OF BONE LESIONS

Based on:
Lena B., Bartels L.W., Ferrer C.J., Moonen C.T.W., Viergever M.A., Bos C. Technical Note: Interleaved water and fat MRT for monitoring HIFU ablation of bone lesions. in *Magnetic Resonance in Medicine (2021)*.

"The ability to monitor temperature changes in adipose tissue is crucial as many thermal therapies are carried out in regions of the body where mixtures of aqueous and adipose tissues are present. Although the fatty regions themselves are usually not targeted for heating, the thermal energy often passes through or diffuses into these areas. "

(Todd N. et al., Magnetic Resonance in Medicine, 2013) [78]

ABSTRACT

Purpose: To demonstrate that interleaved MR thermometry can monitor temperature in water and fat with adequate temporal resolution. This is relevant for High-Intensity Focused Ultrasounds (HIFU) treatment of bone lesions, which are often found near aqueous tissues, as muscle, or embedded in adipose tissues, as subcutaneous fat and bone marrow.

Methods:Proton resonance frequency shift (PRFS)-based thermometry scans and T_1-based 2D Variable Flip Angle (2D-VFA) thermometry scans were acquired alternatingly over time. Temperature in water was monitored using PRFS thermometry, and in fat by 2D-VFA thermometry with slice profile effect correction. The feasibility of interleaved water/fat temperature monitoring was studied ex vivo in porcine bone during MR-HIFU sonication. Precision and stability of measurements in vivo were evaluated in a healthy volunteer under non-heating conditions.

Results: The method allowed observing temperature change over time in muscle and fat, including bone marrow, during MR-HIFU sonication, with a temporal resolution of 6.1 s. In vivo, the apparent temperature change was stable on the time scale of the experiment: In 7 minutes the systematic drift was < 0.042°C/minute in muscle (PRFS after drift correction) and < 0.096°C/minute in bone marrow (2D-VFA). The standard deviation of the temperature change averaged over time was 0.98°C (PRFS) and 2.7°C (2D-VFA).

Conclusion: Interleaved MR thermometry allows temperature measurements in water and fat with a temporal resolution high enough for monitoring HIFU ablation. Specifically, combined fat and water thermometry provides uninterrupted information on temperature changes in tissue close to the bone cortex.

4.1. INTRODUCTION

MRI-guided High-Intensity Focused Ultrasound (MR-HIFU) allows non-invasive treatments of various conditions [28] by thermal ablation and its effectiveness for treatment of patients with painful bone metastases has been clinically demonstrated [36]. Pain reduction in these patients is achieved by ablation of the periosteum in the proximity of the metastases. MRI is a reliable guidance technique for HIFU, due to its excellent soft-tissue contrast and its capacity to map tissue temperature changes [4]. Temperature mapping is used to ensure that sufficient energy is delivered to reach an adequate thermal dose in the target zone, while preventing damage to surrounding healthy tissues. In clinical procedures, proton resonance frequency shift (PRFS)-based thermometry has become the most employed MRT technique for aqueous tissues [5, 140, 141]. Key factors are that the proton resonance frequency of hydrogen nuclei in water molecules varies linearly with temperature [142] and is almost independent of tissue type. Moreover, PRFS thermometry has an easy implementation with rapid gradient echo sequence [143].

For the treatment of bone lesions, existing clinical protocols also rely on PRFS thermometry. Therefore, during treatments, temperature information is only available in voxels containing aqueous tissues, like muscle or tumor tissue [5]. Pure adipose tissues, as subcutaneous fat, and mixed adipose tissues, as bone marrow, are often found in and around bones. Thus, frequently, a mixture of fat- and water-based tissues is present in the target area. Moreover, the energy deposition within the ultrasound beam path can cause unwanted injuries in the area closest to the transducer [144]. Therefore, the heating should be monitored also in the subcutaneous fat [76, 145]. For these reasons, temperature monitoring in both water and fat is desired for treatment of bone lesions.

The low water content and the absence of hydrogen bonding between fat molecules compromise the performance of PRFS thermometry in adipose tissues [5]. Alternative methods have been proposed to monitor temperature in fat, most of which have focused on T_1 [121, 146] of which the temperature coefficient (in ms/°C) has been shown to be similar for the most prominent fat peak in different adipose tissues [147]. To monitor temperature in an environment with both water and fat, Hey et al. proposed a simultaneous PRFS/T_1 measurement technique using the Variable Flip Angle (VFA) method. Aiming for real-time thermometry, they implemented the method using 2D GRE-EPI sequences [77]. However, in 2D, the nonuniform flip angle profile in the slice direction causes errors in T_1 estimates and compromises the accuracy of mapping in fat [88, 125].

In more recent methods for simultaneous PRFS/2D-VFA thermometry [78], a rescaling factor was applied to the FAs, to correct both for slice profile effects and for B_1 inhomogeneity. The rescaling factor was estimated experimentally for given T_1 values and was assumed to apply for all FAs between 5°and 90°. However, in these methods, PRFS thermometry was performed with short echo time (TE) [77, 78], which limits the precision in PRFS temperature maps. Simultaneous measurements of PRFS and T_1 need to balance the precision of both measurements, leading to compromises for the echo time and the flip angle choice.

Here, we propose a 2D water-fat MR thermometry method based on an interleaved framework [148], in which two sequences are independently optimized for the two tis-

sue types: temperature in aqueous tissues is monitored using a PRFS sequence and in fat by using 2D-VFA scans. The 2D-VFA settings are chosen to deliver accurate and precise T_1 estimates over a range of T_1, and T_1 maps are corrected for slice profile effects based on simulation that include the full slice profile [149]. The potential of this technique to provide temperature information in all soft tissues for monitoring MR-HIFU ablation of bone lesions was tested in ex vivo experiments. The stability of the method was investigated under in vivo conditions.

4.2. METHODS

All experiments were performed with a clinical 1.5T MR scanner (Philips Achieva, Best, The Netherlands). Image processing was done offline using MatLab 2018a (Mathworks, Natick, MA).

4.2.1. IDENTIFICATION OF WATER AND FAT VOXELS

Prior to temperature mapping, it is crucial to identify water and fat voxels, to select which of the two temperature readouts will be applied. A 3-point Dixon image was acquired to provide water and fat images [150, 151]. Voxelwise, fat signal fraction maps were estimated by using $S_{Fat}\% = \frac{S_{Fat}}{S_{InPhase}} \times 100$, where $S_{InPhase}$ and S_{fat} are the signal intensities in the reconstructed in-phase and fat image, respectively. An empirically chosen threshold, was then used to select the voxels in adipose tissues, i.e., subcutaneous fat and bone marrow, as identified on anatomical images.

4.2.2. CALCULATION OF TEMPERATURE MAPS

A framework allowing fast switching between pulse sequences was used to interleave acquisition of one PRFS scan with one 2D-VFA scan, which consists of two T_1-weighted (T_1w) images at different flip angles (Figure 4.1). For temperature monitoring we acquired a set of 5 reference PRFS phase maps and 5 reference VFA T_1 maps before heating and continued acquiring interleaved PRFS and 2D-VFA images during the heating and cool-down phases (Figure 4.1A).

VFA-BASED FAT MR THERMOMETRY

T_1 maps for fat thermometry were obtained via the linearized form of the steady-state signal equation:

$$\frac{S}{sin\theta} = E_1 \frac{S}{tan\theta} + M_0(1 - E_1) \tag{4.1}$$

where S is the magnitude signal of a spoiled Gradient Echo (GRE) image, $E_1 = e^{-TR/T_1}$, M_0 is the equilibrium magnetization and θ is the flip angle. After acquiring the signal at 2 FAs, T_1 was estimated from Equation 4.1 by determining the slope of $S/sin\theta$ vs $S/tan\theta$ [90].

Since the method was applied in 2D, a correction for the slice profile effect was applied [152, 153]. We corrected the VFA T_1 maps by means of a T_1 look-up table (LUT), obtained by Bloch simulations including slice profile effects. Briefly, for an input T_1 value and two FAs, the steady state signals were calculated and used to find the apparent longitudinal relaxation time using the conventional VFA T_1 estimation. The apparent T_1 includes the effects of the non-uniform slice excitation. Finally, by repeating the

simulation for a range of T_1 values, and FAs, a look-up table was created from which a slice-profile corrected T_1 can be retrieved based on the apparent T_1. In this procedure, B_1 inhomogeneity is compensated for by scaling the FAs. A LUT with scan parameters as applied in the experiment was generated once prior to the MRT experiment.
The temperature change (ΔT) maps, defined as the difference between the temperature at a time point t_n and the initial temperature, are inferred from the T_1 maps (Figure 4.1B), according to:

$$\Delta T_{fat}(t_n) = \sum_{i=1}^{n} \frac{B}{\ln \frac{A}{T_1(t_i)}} - \frac{B}{\ln \frac{A}{T_1(t_{i-1})}} \tag{4.2}$$

where $T_1(t_i)$ is the T_1 at a time point t_i and $T_1(t_{i-1})$ is the T_1 at a previous time point t_{i-1}. A (ms) and B (°C) are fit parameters from the exponential relation describing the dependence of T_1 on temperature, with A = 2.59×10^5 ms and B = 2.09×10^3 °C as determined for breast adipose tissues at 1.5 T by Baron et al. [121].

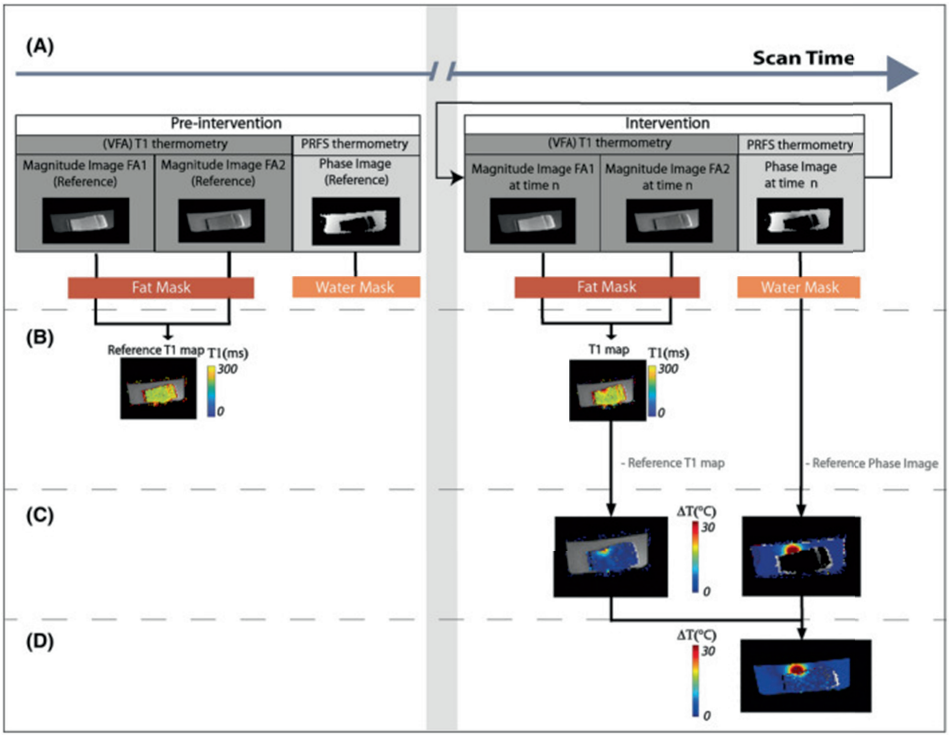

Figure 4.1: A: Fat and water images acquired with the interleaved framework (magnitude images at two FAs for 2D-VFA MRT and phase images for PRFS MRT). B: 2D-VFA T_1 mapping. C: 2D-VFA-based and PRFS-based MRT calculation. D: Fusion of MRT images.

PRFS-BASED WATER MR THERMOMETRY

Temperature change (ΔT) maps in water were determined from the phase images of a spoiled GRE scan with EPI. The temperature change is obtained by subtracting the reference phase $\varphi(t_0)$, at $t = t_0$ before the onset of temperature change, from the current

phase at time t, $\phi(t)$, during heating:

$$\Delta T_{water}(t) = \frac{\varphi(t) - \varphi(t_0)}{\gamma \alpha TE B_0} \tag{4.3}$$

where γ is the gyromagnetic ratio, α is the temperature coefficient of the shielding constant (0.010 ppm/°C), B_0 is the magnetic field strength, and TE is the echo time (Figure 4.1C). A correction for phase drift was applied [4, 5]: drift was estimated from the average phase value in an unheated region from the PRFS scans. From this value, the temperature drift ΔT_{drift} was estimated using Equation 4.3 and subtracted to correct the temperature change maps.

4.2.3. EX VIVO MR-HIFU HEATING EXPERIMENT

Interleaved MRT was tested in an ex vivo experiment using HIFU heating. Experiments were performed on a clinical HIFU platform (Sonalleve MR-HIFU V2; Profound Medical, Mississauga, Ontario, Canada). Images were acquired using the integrated 2-element coil inside the tabletop of the HIFU system and a 16-element flat array coil. The phantom consisted of a water tank, in which an excised lower hind leg of a pig was immersed (Figure 4.2) in degassed water. The intrinsic focus of the ultrasound transducer is an ellipsoid with dimensions of $2 \times 2 \times 7 mm^3$, defined by the -3 dB level, where the longest dimension is along the ultrasound beam direction. MR thermometry was performed for 7 minutes. The heating experiment consisted of 50s before heating, 60s of HIFU sonication at 1.2 MHz with a constant acoustic power of 40 W and a cool-down period of 350 s.

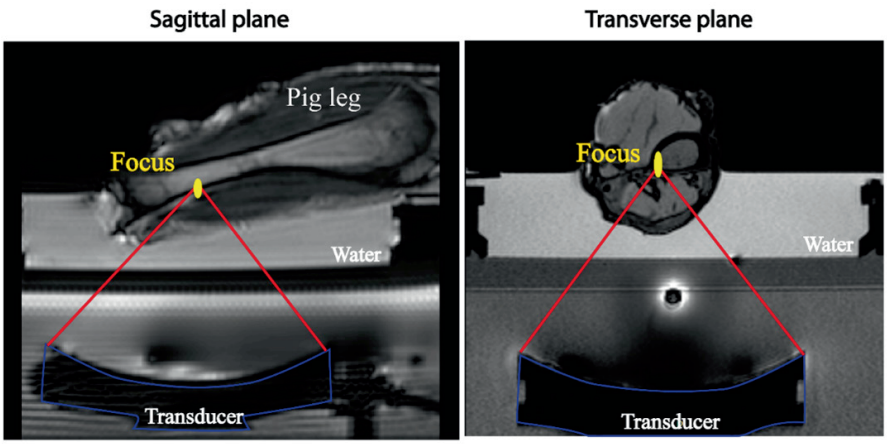

Figure 4.2: Experimental setup for the ex vivo experiment. The ultrasound transducer is outlined in blue and the ultrasound beam path in red. The imaging slice was positioned to match the focal location (in yellow).

A transverse temperature mapping slice was positioned through the focus. For PRFS-MRT, sequence parameter settings included binomial water selective excitation, TE =19 ms, TR= 37 ms, flip angle (FA) = 20°, EPI factor = 11, phase encoding bandwidth 40

Hz/pixel. For VFA-MRT, TE =4.6 ms, TR= 10 ms, FA = 6°- 40°, readout bandwidth 136 Hz/pixel. For both sequences, $200 \times 200 mm^2$ FOV was used, with an acquired voxel size of $2 \times 2 \times 7 mm^3$; number of dummy excitations for dynamics = 150, RF spoiling phase increment = 117°. Temperature maps were generated 6.1 seconds apart, i.e., the duration of a cycle of two 2D-VFA scans and one PRFS scan. In-plane B_1 inhomogeneities were corrected using B_1 maps, acquired using the Actual Flip-angle Imaging method [131]: TR1 30 ms, TR2 150 ms, TE 4.40 ms, FA 60°.

4.2.4. NON-HEATING DEMONSTRATION ON A VOLUNTEER

An in vivo demonstration was performed in one healthy volunteer without heating, with the approval of the institutional review board of the University Medical Center Utrecht (NL53099.041.15), and written informed consent was obtained from the volunteer. A transverse MRT slice was positioned in the lower leg of the volunteer. The same sequences and parameter settings as in the phantom experiment were used. A 16-element receive coil was used for signal reception.
Water and fat regions were set using 3-point Dixon images [150, 151], as before. Using the method described above, 2D-VFA-based temperature maps were calculated in fat. To assess precision, a map of the temporal ΔT_{fat} standard deviation was generated.
Finally, the capability of the proposed method to spatially resolve temperature changes (i.e., as a temperature mapping technique) was evaluated. To this end, we first applied a rotationally symmetric Gaussian filter with standard deviation of 1 pixel for spatial low-pass filtering of the calculated temperature change maps. The range and the drift of the apparent temperature variations were characterized with their 10^{th} (P10) and 90^{th} (P90) percentile values and the slope of the linear regression of the estimates over the 7 minutes scan duration. P10, P90, and the slope of the linear fit were evaluated in 3 voxels each, in the muscle and the bone marrow.

4.3. RESULTS

4.3.1. EX VIVO MR-HIFU HEATING EXPERIMENT

By using 2D-VFA-MRT, it was possible to detect the temperature changes in fat caused by HIFU heating. The temperature evolution was followed in three locations (Figure 4.3A): two voxels in the bone marrow at different distances from the focal point and one voxel in an adipose tissue layer near the focal point (Figure 4.3B). A temperature rise of 20°C was seen in the bone marrow behind the cortex. The three curves show that the voxel closest to the focal point has the largest temperature change, whereas in the other locations, a lower temperature change is detected.
Close to the focal point, two voxels in muscle and bone marrow show a temperature peak ≈120 s after the beginning of the experiment (Figure 4.3C). In the cool-down phase, the behavior of these voxels differs substantially: the temperature in fat decreases rapidly and returns to baseline, whereas the muscle maintains an elevated temperature after the sonication ended.

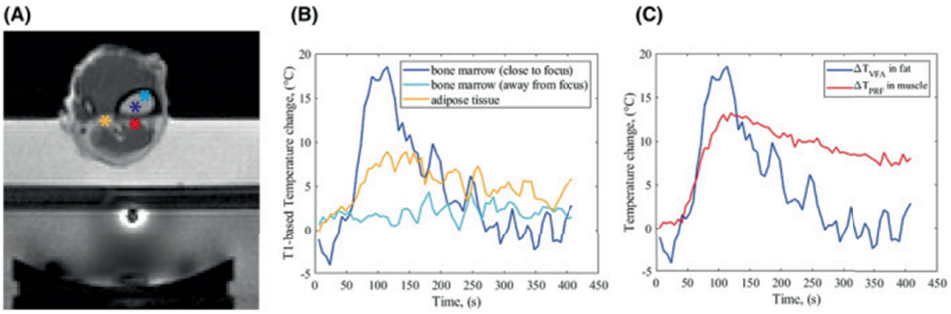

Figure 4.3: Combined water and fat thermometry during a HIFU sonication experiment. A: the asterisks indicate the location of the voxels considered. B: 2D-VFA-based temperature changes (°C) vs time estimated in fat voxels. C: Temperature changes vs time estimated using 2D-VFA-based MRT in fat and using PRFS-based MRT in muscle.

4

The combined water-fat temperature change map at 120s, Figure 4.4C, shows a heated region that is continuous across the water-fat boundaries. A temperature rise of over 20°C was detected in the focal point area. Between 6 mm and 10 mm from the focal point, the detected temperature increase was still over 10°C. These observations are consistent with heat transfer from a region of intense heating at the bone cortex, which served as a heat source for surrounding tissues. However, in the cortical bone no temperature information was available, owing to a lack of MR signal.

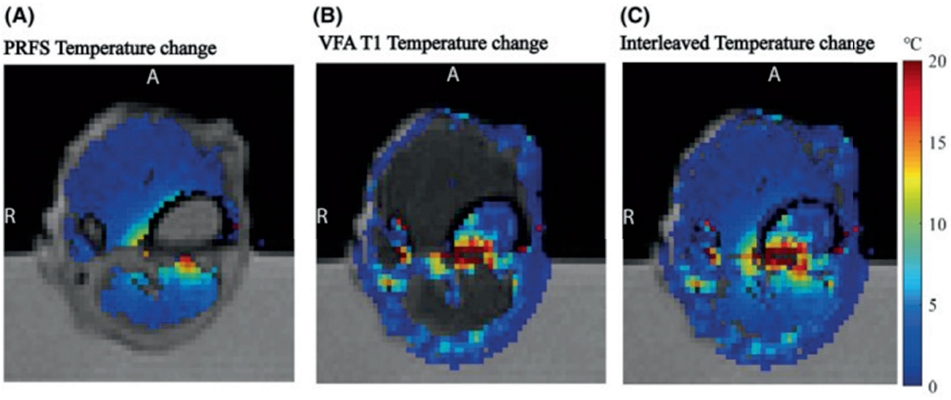

Figure 4.4: Temperature change maps at the temperature peak. A: from PRFS in water voxels. B: from 2D-VFA T1 in fat voxels. C: Overlaying the two maps, a temperature change map from the interleaved thermometry is provided.

4.3.2. NON-HEATING DEMONSTRATION ON A VOLUNTEER

The temporal standard deviation map of ΔT_{fat} in fat voxels of a volunteer leg shows that $\sigma(\Delta T_{fat}) < 1$ °C in the subcutaneous fat and 2-3°C in the bone marrow (Figure 4.5A). We observed that $\sigma(\Delta T_{fat})$ is high where SNR is low, probably due to differences in coil sensitivity. Moreover, $\sigma(\Delta T_{fat})$ increased up to 8°C at the fat-muscle interfaces, probably caused by partial volume effects.

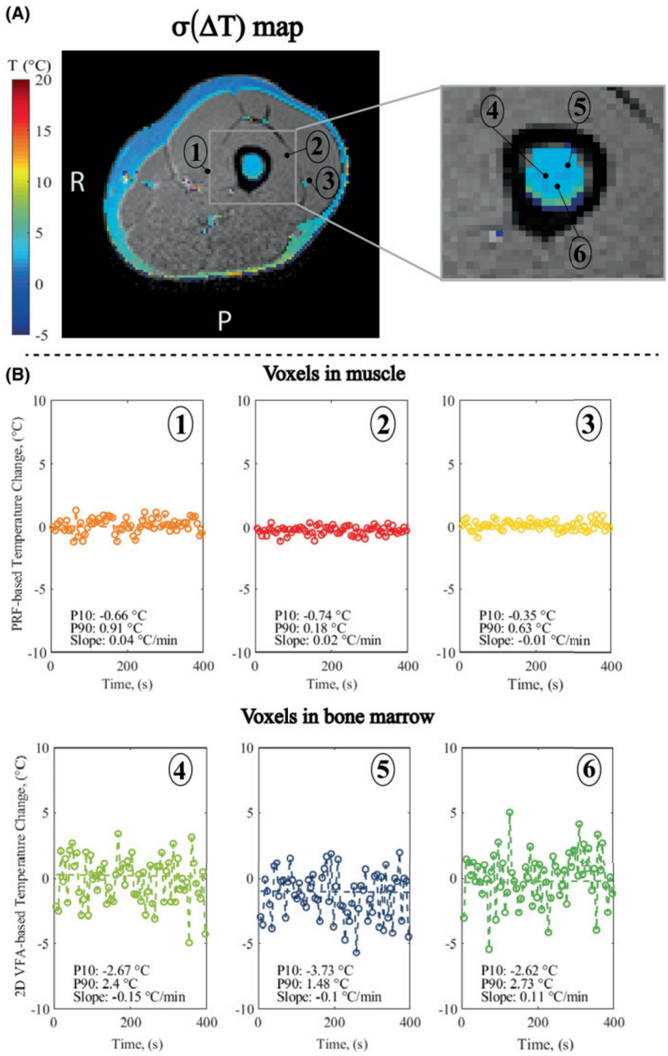

Figure 4.5: A: Temporal SD map of VFA-based temperature change in fat voxels of a transverse slice, located on the lower leg of a volunteer. B: Temperature change estimates, after spatial averaging with a gaussian filter, in the volunteer study without heating: 2D-VFA-based temperature changes in three voxels in the bone marrow and PRFS-based temperature change in three voxels in the muscle.

Since the method is envisioned to be used as a mapping technique, the stability of temperature changes was estimated for individual locations (Figure 4.5B). For all the estimates, the temperature drift was below 0.5°C/minute. The spread of the apparent temperature variations at the individual timepoints was further characterized by P10 and P90. For 2D-VFA-MRT, P10 was found between -2.5°C and -3.7°C, P90 between 1.5°C and 2.7°C. For PRFS-MRT, P10 was found between -0.74°C and -0.35°C, P90 between 0.18°C and 0.91°C.

4.4. DISCUSSION

In this study we have demonstrated the use of an interleaved scanning approach that enables monitoring temperature changes both in aqueous tissues (with PRFS- MRT) and in adipose tissues (with 2D-VFA- MRT). This method could aid monitoring HIFU treatments of bone metastases, for which both adipose and aqueous tissues can be found in the vicinity of the target. The feasibility of this approach was investigated in an MR-HIFU sonication experiment on an ex vivo porcine bone phantom. The method was shown to provide temperature measurements in nearly all tissues in the slice, both fatty tissues, and in any voxels containing sufficient water signal. Finally, the method was shown to be precise and stable enough for being used as a mapping technique in an in vivo experiment, with a temperature standard deviation below 3°C in the bone marrow and negligible systemic temperature drift identified over the scan duration.

With interleaved MRT, it becomes possible to monitor complex heating behavior. In our experiment, this approach allowed to detect temperature change caused by transfer of heat generated by the intersection of the US beam with the cortex [154] into the tissues surrounding the focal area.

MRT is generally used to measure temperature change rather than absolute temperature. Therefore, for the utility of the method, precision and stability over time change here are key parameters. Based on the precision measurements in bone marrow in vivo, we expect that temperature rises of the order of 3°C can be detected. Moreover, the temperature estimates in our experiments were computed continuously for 7 minutes, which resembles the time window of the HIFU sonication protocol (pre-scanning, sonication [33], cool-down [76]) in clinical care. During this time, the 90th percentile of apparent temperature change observed in the single voxels in bone marrow was 1.5-2.7°C, which was likely caused by noise in the 2D-VFA source images. For HIFU ablation, the aim is to achieve temperatures above 60°C in the target area (i.e., temperature changes of more than 23°) [155]. Therefore, with the precision and the stability observed in our experiment, we expect that this method could improve the monitoring of temperature changes caused by HIFU ablation in the anatomy imaged.

Adding fat temperature information is relevant for treatment of bone metastases and tumors, where both the target and the surrounding area can contain adipose tissues [156]. Temperature mapping in water and fat may improve monitoring of heating also during other clinical applications of HIFU in target areas containing aqueous and adipose tissues, such as breast [121] and pancreas [157].

While this study has demonstrated the temperature monitoring ability of the proposed technique, there are several limitations that must be addressed before this sequence may be offered for clinical use.

First, the image processing and temperature estimations were performed offline and, therefore, the potential of interleaved MRT to perform real-time treatment monitoring has not been tested yet. To apply interleaved MRT, water and fat masks were used. However, in case of motion during the scan session, a mismatch of fat and water voxels can occur between the mask (created prior to MRT) and the images from MRT scans. For our use case, i.e., MRT for HIFU therapy of bones, this is less problematic as patients are usually sedated but for other applications this mismatch could be mitigated by registration techniques or dynamic updates of the mask image, e.g., using a multi-echo MRT pulse sequence, as was used by Poorman et al. [87].

The selection of the water and fat regions is key in view of the poor results of T_1 thermometry in voxels with mixed water and fat contributions. Here, a visualization approach based on masks was adopted to avoid partial volume effects. However, the problem could also be solved in acquisition, with fat/water suppression and water–fat separation methods [158].
Moreover, fat thermometry relies on the VFA approach, which is known to be susceptible to B1 inhomogeneties [123]. In this work, we acquired a B1 map to correct for B1 inhomogeneities. However, in case of more homogeneous B1 fields, B1 corrections might be omitted to save time.
Finally, the 6 s overall acquisition time of the technique described here imposes a minimum duration on the heating time, to enable temperature monitoring. In particular the time required to reach the steady state adds to the scan time for the VFA method. This issue has been addressed by Svedin et al. [159], who proposed to only acquire dynamic images at one flip angle during the MRT experiment, thus improving the VFA temporal resolution.

4.5. CONCLUSION

In conclusion, interleaved PRFS and 2D-VFA T_1 thermometry enables temperature monitoring in fat and water for MR-HIFU treatments, showing the heat distribution inside and outside the bone across tissues of different composition. As such, the method holds potential for monitoring MR-HIFU in patients with bone lesions, thus contributing to the safety of treatments.

5

THE INFLUENCE OF FAT LAYER THICKNESS AND SONICATION SETTINGS ON THE ENERGY DENSITY ON BONE SURFACE DURING MR-GUIDED FOCUSED ULTRASOUND ON BONE

Based on:
Lena B., Breuer B.J.T., Ferrer C.J., Bošnački D., Ramaekers P., Moonen C.T.W., Viergever M., Bos C., Bartels L.W. The influence of fat layer thickness and sonication settings on the Energy Density on Bone Surface during MR-guided focused ultrasound on bone. Submitted to *Physics in Medicine and Biology*.

"The EDBS is not sensitive to the limitations of MRI-based PRF thermometry and can serve as a parameter of treatment success independent of thermal dose predictions."

(Bitton R. et al., Investigative Radiology, 2021) [83]

ABSTRACT

Objective: In the context of palliative MR-guided High-Intensity Focused Ultrasound (HIFU) treatments of bone metastases, the Energy Density on Bone Surface (EDBS) parameter has shown correlation with pain relief in patients, making it a possible suitable candidate for prediction of the therapy outcome. In this work, an investigation of the calculation of EDBS and how it depends on different sonication protocols and anatomies during HIFU experiments is presented.

Approach: The EDBS, describing the energy flux arriving at the bone surface, cannot be measured in patients. Thus, in this study, a raytracer simulator was used to investigate the variation of the energy on the bone surface as a function of sonication protocol and pre-focal tissue composition. A simplified geometrical model, less heavy in computational times, was also tested, using the advanced simulator as reference. Moreover, MR thermometry performed during actual sonications provided experimental data to verify the simulation results. The experiments consisted of HIFU sonications using different sonication duration and power of a phantom mimicking differing thickness of muscle and fat in front of the bone. For all experiments, the energy on the bone surface was calculated with the two models and the temperature was measured with MR thermometry.

Main results: Both the raytracer and the geometrical method could be used to simulate changes in the energy values. Moreover, with the same energy emitted from the transducer, lower energy is delivered in the focal zone and lower temperature is reached at the target when a fat layer is present in the US beam, with the lowest values for the thickest prefocal fat layer.

Significance: in the future, EDBS may play a role in executing therapy. In this scenario, the presence and thickness of prefocal fat should be considered, as it influences the amount of energy that reaches the bone surface. This effect has also been confirmed experimentally.

5.1. INTRODUCTION

MRI-guided High Intensity Focused Ultrasound (HIFU) therapy is a noninvasive procedure that has shown promising results for pain palliation in patients with bone metastases [1, 2]. Its primary mechanism of action is thought to be thermal ablation of the nerves that produce pain, inside and in proximity of the lesion [3]. Since these nerves are in the proximity of the bone, the bone is targeted during HIFU treatments of bone metastases, exploiting the high acoustic absorption and relatively low thermal conduction of bone to cause critical thermal damage to the adjacent nerves [4]. To this aim, the treatments use different sonication strategies, and sonication protocols of varying power, duration, number and positioning of the individual sonications [5]. Moreover, the tissue composition between the transducer and the target lesion varies per anatomy and per patient, in terms of amount of fat and muscle [6].

Since pain relief is expected to manifest within days from the procedure, the therapeutic outcome is still unknown at the end of a therapy session. It would be beneficial to have an indicator available during the treatment that could be used to maximize therapy efficacy. Such an indicator should be predictive of pain response and should be applicable regardless of the possible variations of sonication protocols and patient anatomy.

A possible image-based indicator is the measurement of temperature and thermal dose [5], that can both be derived from MR temperature maps. Such maps are typically measured by means of Proton Resonance Frequency Shift (PRFS) MR thermometry [7, 8] and the thermal dose can be calculated from time series of temperature maps [9, 10]. However, PRFS thermometry is limited by the lack of temperature information in cortical bone and fat, and by its sensitivity to motion [11, 12]. Other methods have shown promising results for measuring temperature in water and fat during ablation [13], but their temporal resolution is still not suitable to monitor temperature changes during short sonication durations. Therefore, MRT-based indicators seem less suitable candidates for predicting pain relief for procedures on bone metastases. Moreover, an MR imaging-based evaluation of the ablation zone through the Non-Perfused Volume (NPV), as is common for MR-HIFU ablations of uterine fibroids [14], is not straightforward when ablating thin nervous layers.

In a recent study, Bitton et al. suggested the use of an estimate of the amount of ultrasound energy delivered to the target as an indicator [15]. They showed that the energy density on the bone surface (EDBS) showed correlation with pain relief in patients, making it a possible suitable candidate for prediction of the therapy outcome. In that study, EDBS was calculated as the total acoustic energy that reaches the bone during the treatment procedure divided by the targeted surface area on the bone [15]. It was not explained which assumptions, model and conditions were used to calculate EDBS values. Since the results presented in that study were promising, an investigation of the calculation of EDBS and how it depends on conditions and parameter settings during HIFU treatment of bone metastases was warranted.

The EDBS parameter describes the time integral of the acoustic intensity arriving at the bone surface over the duration of the sonication, and therefore can be expressed in J/mm^2. A direct measurement of this parameter cannot be performed in patients, but it can be estimated by simulation or calculation. Advanced HIFU simulators are suitable tools to estimate local energy and EDBS values. Moreover, such simulators allow

investigation of the influence of varying single parameter settings on the energy flux. However, HIFU simulations have long computational times, which hampers their on-the-fly application during clinical procedures. An option to calculate EDBS that may be more suitable for eventual clinical use could be to use simplified physical models. The aim of this work was to study how the energy density on bone surface depends on different sonication protocols for a number of predefined anatomical models. An raytracer simulator was used as a reference to investigate the influence of sonication protocols and geometry/anatomy on the acoustic energy flux reaching the bone target. The analysis was performed also with a highly simplified US model. To verify the findings of the simulations, an experimental demonstration through actual HIFU sonications was performed, in which temperature was monitored with MR thermometry to show the effect of local energy deposition on tissues. These MR-HIFU experiments were performed under the same varying conditions as those applied for the simulations and calculations.

5.2. MATERIALS AND METHODS

Here, first, the tools used for this investigation are presented in more details and then the experiments are described.

5.2.1. THE TOOLS

THE ENERGY MODELS

In Bitton et al., EDBS was calculated as:

$$EDBS = \frac{\sum E_S(J)}{SA_{ROT}} \tag{5.1}$$

where E_S is the energy delivered on the bone surface in joules per sonication that hits this surface, and SA_{ROT} is the surface area on the bone within the region of treatment [15]. Both the energy and the bone surface are subject of definition choices. In their paper [15], the authors did not describe in detail the way the delivered energy was calculated. The region of treatment and a set of contours defining the bone surface were manually drawn on pretreatment MR images in the planning HIFU software [1].
In practice, the sonicated bone surface area, which depends on the sonication strategy chosen [5], is defined by the intersection of the US beam path with the bone.
In this study, the energy that reaches the surface of the bone was calculated using two approaches:

- A ray tracing model, based on simulations of US pressure fields from a multi-element HIFU transducer [16, 17].
- A simplified geometrical model, which accounts for the influence of acoustic attenuation in different tissues layers under the assumption that all US energy is contained within a cone beam that converges to the focal point.

THE ENERGY ON BONE SURFACE FROM THE RAYTRACER MODEL

The raytracer model accounts for the propagation of shear and longitudinal waves in isotropic solids and fluids. Ultrasound waves leaving a circular transducer element are

modelled as a set of individual rays, each with a phase, a wave vector and a power level [16, 17]. Each ray is generated with a random direction and attributed a fraction of the total power emitted by the transducer element. The Far Field Approximation for the pressure pattern emitted by the transducer element [16] is used to calculate the power fraction for a certain ray, which depends on the angle between the propagation direction of the ray and the normal vector on the transducer surface.
Within a single material type the rays propagate along straight lines and power attenuation is calculated using the acoustic attenuation coefficient of this material. When a ray encounters an interface, refracted and reflected rays are generated with direction, power and phase (and polarisation in case of solids) determined by Snell's law and the solutions to the acoustic Fresnel equations.
In this model, a volumetric region is gridded into cubes in which the properties of the rays are recorded. When a ray intersects a cube, the power and phase associated to the ray are used to calculate the acoustic intensity. In cubes containing fluids, the complex pressures based on the associated amplitudes of all the incoming rays are calculated and added, to model the interference between waves (see Modena et al. [16] for further details). The resulting sum of complex pressures p_{tot} is then used to calculate the time averaged acoustic intensity $\langle I \rangle$ (in W/mm^2) through:

$$\langle I \rangle = \frac{|\mathrm{p}_{tot}|^2}{2\mathrm{c}\rho} \tag{5.2}$$

where c is the speed of sound and ρ is the density. This is a good approximation in situations where ultrasound waves are only longitudinal, as is the case in fluids, soft tissues and tissue-mimicking gels, when assuming that, because of the directionality of the beam, all rays hit one side of the cube at a small angle to the surface normal. From this acoustic intensity, I (in W/mm^2), the energy density (in J/mm^2), was by integration over the sonication duration:

$$\varepsilon_D = \int_{T_0}^{T} I\,dt = I\Delta T \tag{5.3}$$

for sonications of constant I and duration ΔT. Finally, defining a surface area S, the energy delivered on that surface (in J) was calculated as:

$$E_{rt} = \int_S \varepsilon_D dS \tag{5.4}$$

THE ENERGY ON BONE SURFACE FROM THE GEOMETRICAL MODEL

In the geometrical model (Figure 5.1), the ultrasound beam is modelled as a 3D cone. Moreover, the transducer is modelled as mono-element, i.e. the whole transducer surface is oscillating in phase.
The constant power **P** radiated from the transducer surface **S** with the acoustic intensity I in each surface element *ds*, i.e., portion of the transducer surface, is defined as:

$$P = \int_{\mathbf{S}} \mathbf{I}(\mathbf{s}) \cdot \mathrm{d}\mathbf{s} \tag{5.5}$$

It is convenient to evaluate the modelling of the transducer in spherical coordinates, with the origin at the focus, and θ the polar angle and ϕ the azimuthal angle, respectively. A spherical transducer (Figure 5.1a) with focal length R and an aperture defined

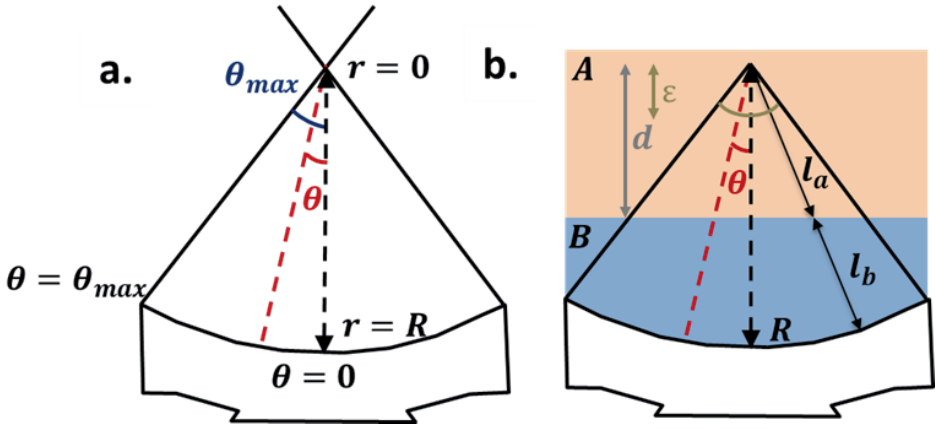

Figure 5.1: Schematic representation of the ultrasound beam with focal length R and apex angle $2\theta_{max}$ without media (a) and with two media between transducer and focus (b).

by the apex angle $2\theta_{max}$ has a surface area S of:

$$S = R^2 \int_0^{2\pi} d\phi \int_0^{\theta_{max}} \sin\theta d\theta = R^2 2\pi(1-\cos\theta_{max}) \tag{5.6}$$

Using Equation 5.6, the intensity at the transducer surface is

$$I(R,\theta_{\max}) = I_{emit} = \frac{P_{emit}}{S_{emit}} = \frac{p_{emit}}{R^2 2\pi(1-\cos\theta_{\max})} \tag{5.7}$$

where P_{emit} is the emitted acoustic power from the transducer as whole.
For a geometry with two parallel layers of materials A and B both perpendicular to the beam axis between the transducer and the focal point, and d the distance between the focal point and the A/B-interface at $\theta = 0$, the thickness of the material A is $l_a(\varepsilon,\theta) = d/cos\theta - \varepsilon$ and of the material B is $l_b(\theta) = R - d/cos\theta$ for each θ, with ε the distance between the focus and a spherical surface S_{deliv} that may be arbitrarily close to the focus in material A (Figure 5.1b). With $\mu_{(i,a)}$ and $\mu_{(i,b)}$ the intensity acoustic attenuation coefficients of the two materials, the ratio R_p of the powers emitted from the transducer and delivered on the spherical surface is:

$$\begin{aligned} R_p &= \frac{P_{deliv}(\varepsilon,\theta)}{P_{emit}} = \frac{\int I_{deliv} dS_{deliv}}{\int I_{emit} dS_{emit}} \\ &= \frac{\varepsilon^2 \int_0^{2\pi} d\phi \int_0^{\theta_{\max}} \sin\theta d\theta \frac{R^2 I_{emit}}{\varepsilon^2 e^{-\mu_{i,a} l_a(\varepsilon,\theta) - \mu_{i,b} l_b(\theta)}}}{R^2 \int_0^{2\pi} d\phi \int_0^{\theta_{\max}} \sin\theta d\theta I_{emit}} \\ &= \frac{\int_0^{\theta_{\max}} \sin\theta d\theta e^{-\mu_{i,a} l_a(\varepsilon,\theta) - \mu_{i,b} l_b(\theta)}}{\int_0^{\theta_{\max}} \sin\theta d\theta} \end{aligned} \tag{5.8}$$

with $dS_{deliv} = \varepsilon^2 d\phi sin\theta d\theta$ and I_{deliv} the delivered attenuated intensity at this surface. In the remainder of the paper, the model is extended to include more than two

materials. The acoustic energy at a distance ε to the focal point (with $\varepsilon < d$) using this geometrical model then is:

$$E_{geo} = \int_0^t P_{deliv}\,dt = \int_0^t P_{emit} \cdot R_p\,dt = P_{in} \cdot R_p \cdot \Delta T \tag{5.9}$$

for a constant emitted power for a fixed duration Δt.

THE PHANTOM

The phantoms in this study (shown in Figure 5.2) were created to mimic layers of fat adipose tissue and muscle in front of the bone typically seen when treating a bone lesion in a patient.

To mimic differing thickness of muscle and fat in front of the bone, a phantom with interchangeable layers was built. The main part of the phantom (referred to as "core") consisted of a cylindrical 2% agar silica gel with 16 cm diameter and 7 cm length, doped with 0.02% manganese chloride to shorten its longitudinal relaxation time to approximately 500 ms. A hollow bone of 9.5 cm length, 2.5 cm external diameter and with a bone thickness of 0.5 cm was obtained from a lower hind leg of a pig from a butcher, after removal of muscle, fat and marrow. The bone was embedded in and filled with the gel. The bone ends were marked with cuts, to facilitate reproducible positioning in all experiments. The interchangeable part of the phantom (referred to as the "pre-focal component") either consisted of a layer of doped agar-silica gel or commercially available pork fat from the butcher, (Figure 5.2a). The thickness of these layers was chosen to be in the range of subcutaneous fat thickness expected in patients with bone metastases (e.g., Figure 5.2b), thus approximately 1 and 3 cm.

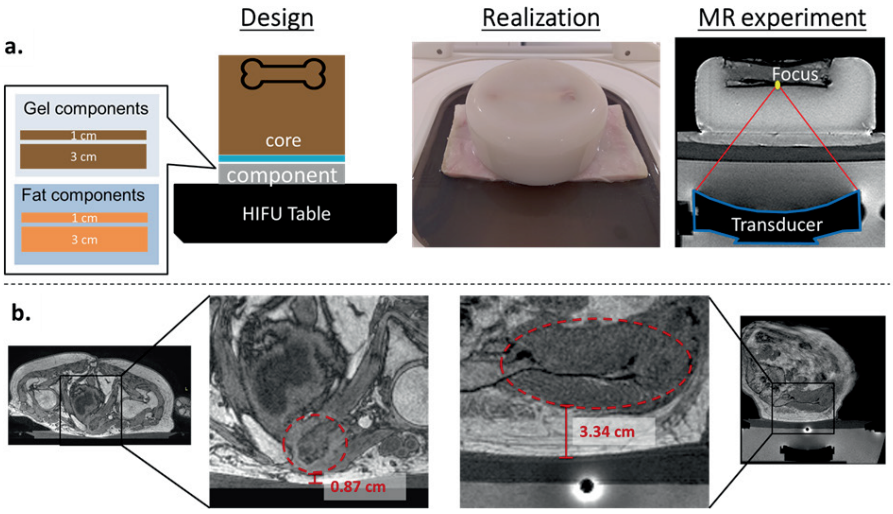

Figure 5.2: a. Experimental setup for the phantom experiment. The ultrasound transducer is outlined in blue and the ultrasound beam path in red. The imaging slice was positioned to match the focal location in the transverse plane (in yellow). Moving from the transducer towards the target, the US beam cone intersects with the following layers: castor oil, water from the Direct Skin Cooling (DISC) device in the MR-HIFU system [18], fat (when present) and agar gel with 2% silica. b. Typical MRI images from patients showing pre-focal tissue distributions with fat thickness of ≈1 cm and ≈3 cm. Targeted metastases were within the red dotted ellipses.

THE MR-HIFU PROTOCOLS

MR IMAGING

MR imaging was performed to image the phantoms for the simulation and to monitor temperature during HIFU heating experiments. All MR acquisitions were performed on a clinical 1.5T MR scanner (Philips Achieva, Best, The Netherlands) equipped with a clinical MR-HIFU system (Sonalleve MR-HIFU V2; Profound Medical, Mississauga, Ontario, Canada). MRI signals were acquired using the integrated 2-element RF receive coil inside the tabletop of the MR-HIFU system and a 3-element flat array coil, positioned on top of the phantom.

The temperature evolution was monitored with 3D PRFS thermometry, using a stack of 15 partitions centered on the focus, based on a gradient-recalled echo imaging sequence with Echo Planar Imaging (EPI) read out [18]. Sequence parameter settings included binomial water selective excitation, TE = 19 ms, TR = 45 ms, flip angle (FA) = 23°, EPI factor = 11, field of view (FOV) = 210 × 178 × 22.5 mm^3, acquired voxel size = 2.0 × 1.8 × 3.0 mm^3, and reconstructed voxel size = 1.3 × 1.3 × 1.5 mm^3. Bandwidth was 44 Hz/Px in the readout direction and 541 Hz/Px in the EPI phase-encoding direction. The acquisition of one 3D volume required 3.5 s. To model the geometry of the phantoms for the simulations, high-resolution 3D MR images of the phantoms with 1 and 3 cm fat component were acquired. The high-resolution scans were T_1-weighted (T1w-) Gradient Echo (GRE) sequences, with TE = 4.60 ms, TR = 30 ms, FA = 20°, FOV= 220 × 200 × 180 mm^3, acquired voxel size = 0.5 × 0.5 × 2.0 mm^3.

Using the open-source software 3D Slicer [19], the 3D MR images were segmented into bone, agar gel and agar or fat identified as "prefocal component". Tetrahedral volume meshes were then created from these segmented images using the segment Mesher extension, which internally uses the open-source software Cleaver [20] and labelled according to the tissue. From the labelled volumes, triangulated meshes were created for the interfaces between different tissues.

HIFU TRANSDUCER

For our simulation and MR experiments, the phased array HIFU transducer of the clinical MR-HIFU system was used, which consisted of 256 elements placed on a spherical shell (14 cm radius of curvature, 14 cm aperture diameter), and was operating at 1.2 MHz. The focus of the ultrasound transducer was an ellipsoid with dimensions of 2 × 2 × 7 mm^3, where the longest dimension is along the ultrasound beam direction. The focus was placed on the interface of the bone cortex and the gel. The transducer was in a reservoir filled with castor oil.

5.2.2. SIMULATION AND MEASUREMENTS UNDER VARYING REALISTIC CONDITIONS

To study the influence of tissue composition on the energy on bone surface and temperature, all experiments were performed with the "core" phantom placed on top of a different "prefocal component" layer:

- Core phantom with the 1 cm gel component;

- Core phantom with the 1 cm fat component;
- Core phantom with the 3 cm gel component;
- Core phantom with the 3 cm fat component.

To study the influence of US settings on the energy on bone surface and temperature, for each phantom, three sonication protocols were used, consisting of low power and long duration, medium power and middle duration, high power and short duration (Table 5.1), all with the same total emitted acoustical energy per sonication of 1.44 kJ.

Table 5.1: Power, duration and energy emitted from the transducer of the sonication protocols in the experiment.

Power [W]	**Time [s]**	**Emitted Energy [J]**
30	48	1440
60	24	1440
90	16	1440

SIMULATIONS

An overview of the physical properties used in the acoustic simulations is given in Table 5.2 [21–23].

Table 5.2: Acoustic material properties used in the simulations.

Medium	**c [m/s]**	ρ **[kg/m^3]**	μ_a **[Np/m]**
Castor Oil	1430	1070	1.04
Water	1500	997	0.02
Fat	1478	950	27
Agar with 2% silica	1491	1019	5.76

c = speed of sound (m/s), ρ = density (kg/m^3), μ_a= ultrasound amplitude attenuation coefficient (Np/m).

THE RAYTRACER SIMULATOR

The raytracing simulations were repeated for the 4 phantom combinations, approximating the surface boundaries between media by triangular meshes of two phantoms (1 and 3 cm of prefocal component). Acoustic intensities were mapped into a sampling region around the focal point big enough to cover the target area with dimensions $38 \times 53 \times 38$ mm^3 and isotropic spatial resolution of 0.48 mm.

The energy on the bone surface was calculated in a region of interest (ROI) defined on a coronal slice of the volumetric ε_D energy density map, situated at approximately 2 mm from the focal point, in the gel in front of the bone (Figure 5.3a). The same circular ROI of 148 voxels was used in all experiments (Figure 5.3b). Knowing the surface area S_i of one side of a single cubic voxel and the energy density ε_D of the N pixels in the ROI, the energy on bone surface from the raytracer follows from the discretization of Equation

5.4:

$$E_{rt} = \sum_{i=0}^{N} \varepsilon_{Di} S_i \tag{5.10}$$

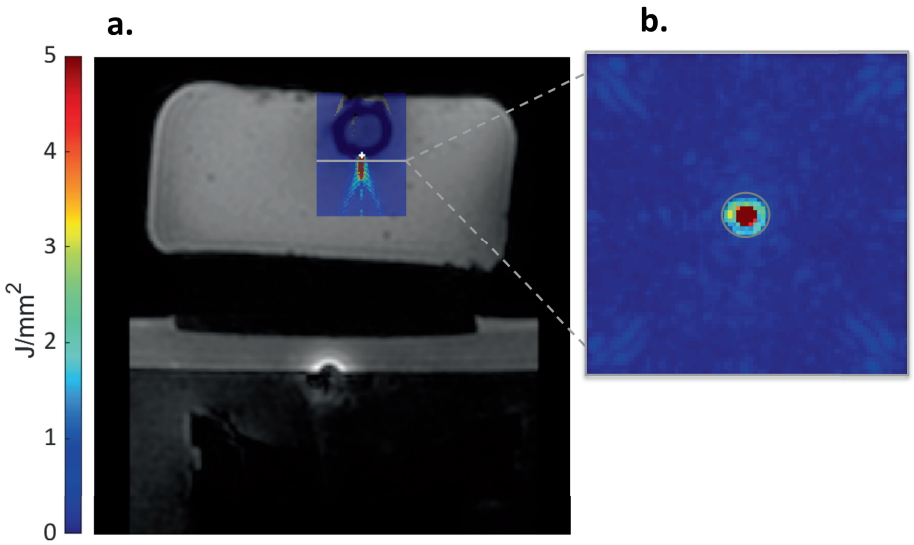

Figure 5.3: a. Overlay of an MR image from a phantom with the energy density (time integral of intensity per voxel) map in a transverse slice through the beam axis. The grey line shows the location of the coronal energy density map close to the surface of the bone and the white + the planned focus. b. Coronal energy density map. In grey the ROI chosen.

THE GEOMETRICAL MODEL

The geometrical model (see paragraph 5.2.1) was extended to include either 3 or 4 materials in the beam path, in the simulation experiments without and with fat, respectively. The focal distance R was the same for all experiments and the distances between the various interfaces and the focal point were measured in the high-resolution 3D MR images. Using the intensity attenuation coefficient, the energy on the bone surface was calculated for each experiment.

MR-HIFU EXPERIMENTS

Prior to thermometry experiments. Acoustic coupling between the core and the prefocal component was established using a mixture of degassed ultrasound transmission gel and water (in a ratio of 1:3). It was verified that the interfaces between the HIFU membrane and the phantom and between the phantom layers were free from air bubbles, using a fast T1w-GRE sequence.

Thermometry experiments. The position of the intrinsic focus was checked using the markers on the bone to put the bone in the same position in all experiments, with different layers of gel and fat. A test sonication with a 2-mm HIFU cell of 15 W for 16 s was performed to check the temperature increase in front of the bone. The thermometry

experiment consisted of a fixed pre-heating period of 30 s, variable period of HIFU sonication (between 16 and 48 s) at 1.2 MHz with a constant acoustic power and a variable cool-down period for sonication duration (between 462 and 494 s) to keep the total duration of the experiment constant. MR thermometry was performed during the whole experiment for 9 minutes. This scheme was repeated 3 times per sonication protocol, with a 20-minute resting time between sonications to allow the temperature in the focal area to return to baseline for the next measurement.
After thermometry experiments. The temperature change at time t was obtained by subtracting a reference phase image, acquired before the onset of temperature change at time t_0, from the phase image acquired at time t during heating:

$$\Delta T_{water}(t) = \frac{\varphi(t) - \varphi(t_0)}{\gamma \alpha TE B_0} \tag{5.11}$$

where $\varphi(t)$ is the phase at time t, $\phi(t_0)$ is the reference phase map before heating, γ is the gyromagnetic ratio (267.52 Mrad/s/T), α the temperature coefficient of the shielding constant (-0.010 ppm/°C), TE the echo time and B_0 the field strength [18]. The reference phase map was calculated by averaging 3 pre-heating phase maps. A correction for phase drift was applied [7, 24]: drift was estimated from the average phase value in an ROI of 67 voxels in an unheated region in the gel of the phantom from the PRFS scans. The phase error due to drift was subtracted to correct the temperature change maps.
From the temperature maps, we created voxelwise maximum temperature projections through the $T(x, y, z, t)$ volume in the t-direction for all phantoms and sonication protocols. These maps give an indication of the maximum temperature reached in the focal area during the whole experiment.

COMPARISON OF ENERGY AND TEMPERATURE

The energy values on the bone surface calculated from simulation were compared for different phantoms and sonication protocols to identify the main differences between the outputs of the geometrical and the raytracer model. To be able to compare experimental results to simulations, the calculated energy reaching the bone surface and temperature increase observed for different fat layer thicknesses were normalized by dividing by the values obtained for the cases without fat.

5.3. RESULTS

5.3.1. SIMULATIONS OF THE EXPERIMENTS

Comparing the different intensity distributions simulated with the raytracer in Figure 5.4, it is observed that acoustic intensity levels for the experiments with fat are lower than those without fat in the US beam path. This effect is more evident in the 3 cm case.

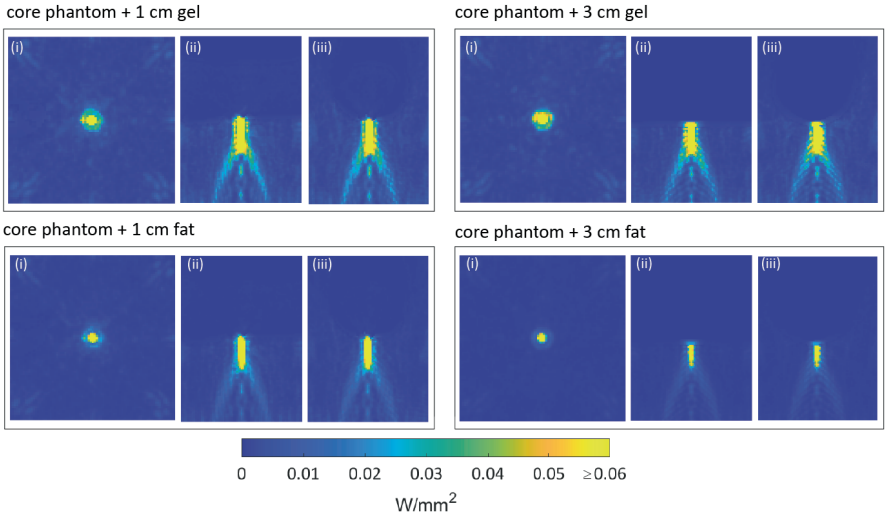

Figure 5.4: Raytraced acoustic intensity distributions on the US beam path in the (i) XZ-plane, (ii) YZ-plane, (iii) YX-plane, with Z being the B_0 direction, for the experiments with different prefocal tissues and thicknesses. The YZ- and YX-plane are centered in the focal point, whereas the XZ-plane is approximately 2 mm distant from the focal point and thus, from the bone.

The energy density distributions on the bone are shown in Figure 5.5. Less energy reaches the targeted bone surface when a layer of fat between transducer and focus is present. The results of the calculation of the energies on the bone surface with the raytracer are summarized in Table 5.3.

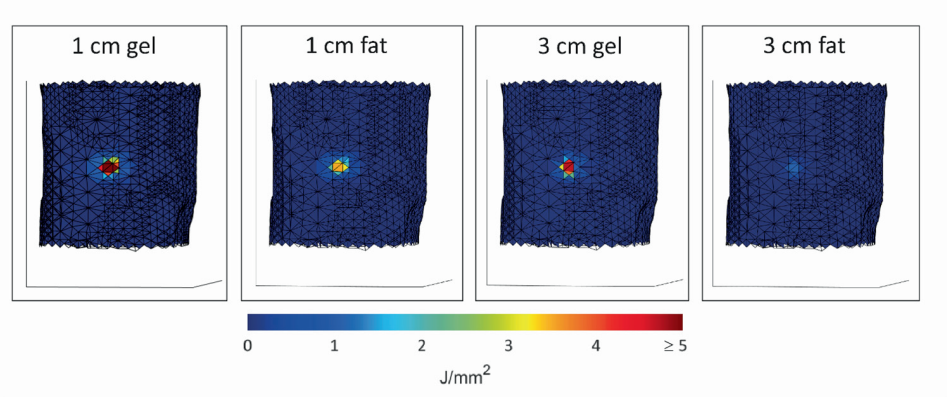

Figure 5.5: Simulated energy density maps from the raytracer overlayed on surface meshes of the bone for the experiments with different prefocal tissues and thicknesses on the US beam path.

Calculations of the energy reaching the bone surface based on the geometrical model are summarized in Table 5.3. With the same energy emitted from the transducer, lower energies were calculated for the experiments with fat in the US beam path compared to the ones without fat, with the lowest value for 3 cm fat.

5.3.2. MR-HIFU EXPERIMENTS

The drift error observed in the MRT experiments, including pre-heating and cooling down, was approximately 4-5 °C.
With a sonication protocol of power 30 W and duration 48 s, temperature rises above 25 °C were measured using MR thermometry in the focal area for phantoms with only gel in the US beam path (Figure 5.6). The maximum temperature increase was 15 °C when 1 cm of fat was inserted and approximately 5 °C with 3 cm of fat.
A similar effect has been observed also with 60 W sonications of 24 s and with 90 W sonications of 16 s (Figure 5.6 for 3-cm phantoms and Figure 5.S2 in Supplementary Materials for 1-cm phantoms). For all sonication protocols, lower focal temperatures were measured when fat was present in the phantom. Thus, the variations observed per measurement point (the standard deviation in the graphs) with the 3-cm fat phantom were smaller compared to measurements with the other phantoms. This is likely a temperature gradient effect, as the SD in an ROI scales with the temperature changes.
Repeating each experiment 3 times, similar results were obtained as shown by the vicinity of the lines in the graphs 6 and by the maximum temperature measurements in Figure 5.7.

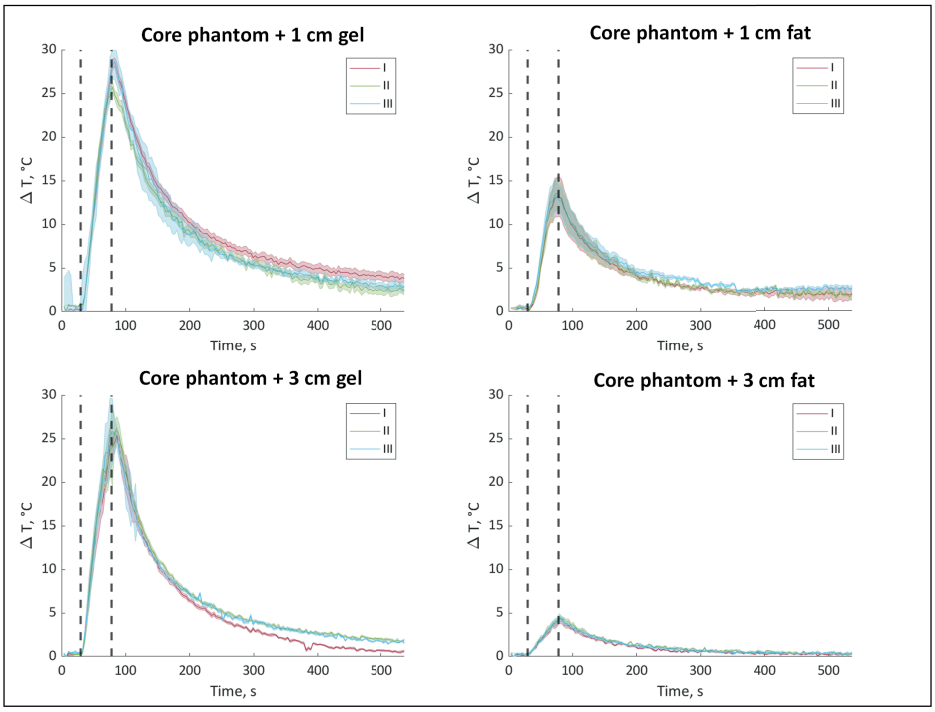

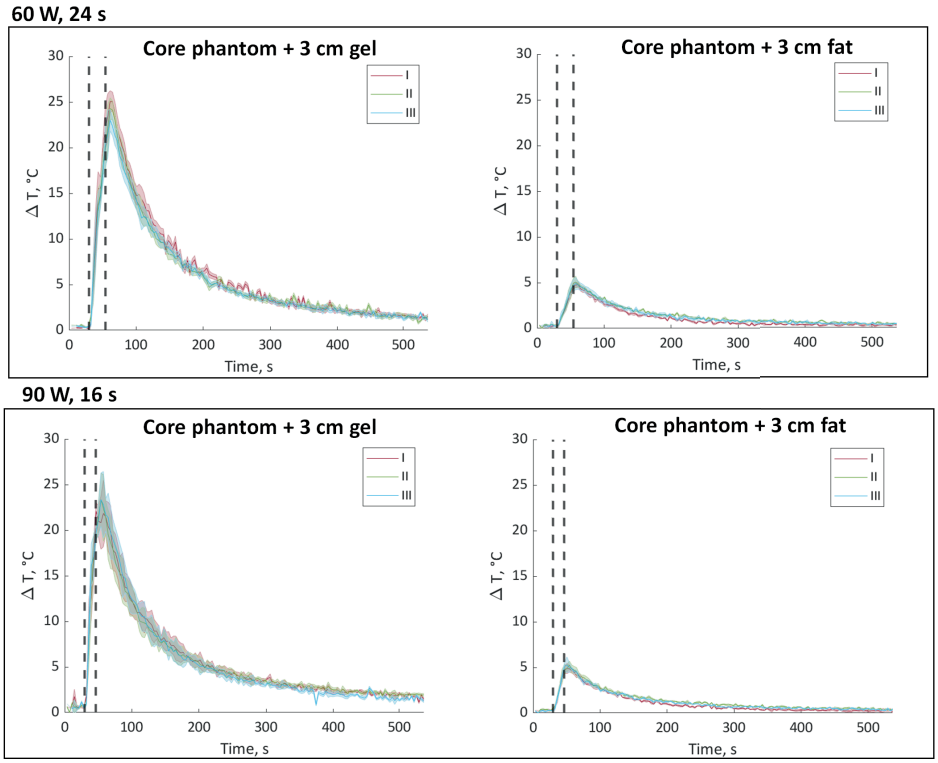

Figure 5.6: Mean (thick line) ± standard deviation (shaded area) of the temperature change over time measured with MRT in a 3D ROI (7x2x6 voxels) in the focal area in the gel during and after sonications of 30 W-48 s in 4 phantoms and sonications of 60 W-24s and 90 W-16 s in 2 phantoms. The dashed lines indicate the start and the end of the sonications. Each sonication was repeated 3 times per phantom experiment.

The maximum temperature increases on MR temperature maps for different protocols and phantoms are shown in Figure 5.8. The quantitative MRT results in a 3D ROI in the focal area (7 × 2 × 6 voxels) can be found in Table 5.3. The maximum temperature rises in the focal area are consistently different per phantom. With prefocal fat layers, the temperature elevations in the focal area were considerably lower. However, the different sonication protocols did not result in evident quantitative changes in temperature in the focal area. Minor temperature variations for different sonication protocols are shown in Figure 5.S3.

5.3.3. COMPARISON OF ENERGY AND TEMPERATURE

The energy values in an ROI just in front of the bone calculated with the geometrical and the raytracer approach are reported in Table 5.3 for each experiment. The values calculated with the geometrical approach are 6-7 times bigger than those from the raytracer, which is not surprising since this model assumes all energy emitted from the transducer to remain within the US transducer cone. This is not realistic, as ultrasound waves interact with tissues not only through absorption (taken into account in the geometrical model) but also with reflection, refraction and scattering. However,

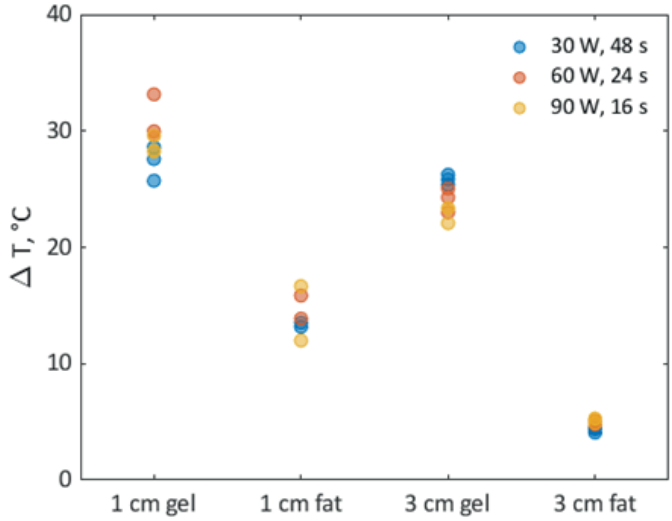

Figure 5.7: Maximum temperature increase for each phantom experiment. Repeated experiments are indicated with the same color. Each sonication was repeated 3 times per phantom experiment, except for the experiment with 1 cm gel.

both calculations show a dependence on the fat thickness: the highest energies were found for the experiments without fat, with a small decrease with 1 cm fat and a bigger decrease with 3 cm fat.
This change has also been observed in the temperature results in the focal area, reported in Table 5.3. Small temperature differences are visible per sonication protocol. Phantoms with fat showed a slightly higher temperature change with the sonication of shorter duration, which was not observed in the phantoms with gel only. However, it is difficult to assess whether they represent a real effect as the precision of PRF-MRT is approximately 1 °C.
Since the energy arriving near the bone is driving the temperature rise in that area, we evaluate the ratios of energy and temperature with and without fat layers. As shown in Table 5.3, both the geometrical and the raytracer method show similar changes in energy ratios when fat is present. We observed that the ratios of temperature show close agreement to ratios of energy, for both the geometric and the raytracer model. This means that in the search for an estimator able to detect changes in the amount of energy arriving at the bone, both simulation models could be used, the geometrical model having the advantage of being faster and simpler.

Table 5.3: Energy on the bone surface, maximum temperature change and ratio of energies and temperature without and with fat of different thicknesses in the beam path for the experiments with different sonication protocols, prefocal tissues and thicknesses on the US beam path. The energies were calculated in a ROI in front of the bone with the geometrical and the raytracer method and the maximum temperature changes in the focal area were measured with MR thermometry.

Phantom Type	**Sonication Protocol**	**Emitted Energy [J]**	**Energy on Bone Surface [J]**		**Max ΔT (°C)***	**E / E_{Gel} on Bone Surface**		**ΔT / $ΔT_{Gel}$**
			Raytracer	***Geometrical***		***Raytracer***	***Geometrical***	
1 cm gel	*30 W, 48 s*	1440	78.0	580.6	27.6 ± 1.7	1^	1^	1^
	60 W, 24 s				28.0 ± 1.6			1^
	90 W, 16 s				28.2 ± 1.3			1^
1 cm fat	*30 W, 48 s*	1440	41.5	279.6	13.4 ± 0.2	0.53	0.48	0.49
	60 W, 24 s				14.9 ± 1.2			0.53
	90 W, 16 s				15.2 ± 2.3			0.54
3 cm gel	*30 W, 48 s*	1440	70.3	475.6	25.8 ± 0.4	1^	1^	1^
	60 W, 24 s				24.1 ± 1.0			1^
	90 W, 16 s				23.0 ± 0.7			1^
3 cm fat	*30 W, 48 s*	1440	15.9	105.8	4.3 ± 0.2	0.23	0.22	0.17
	60 W, 24 s				4.9 ± 0.2			0.20
	90 W, 16 s				5.2 ± 0.2			0.23

*average ± std among repeated sonications
^ by definition

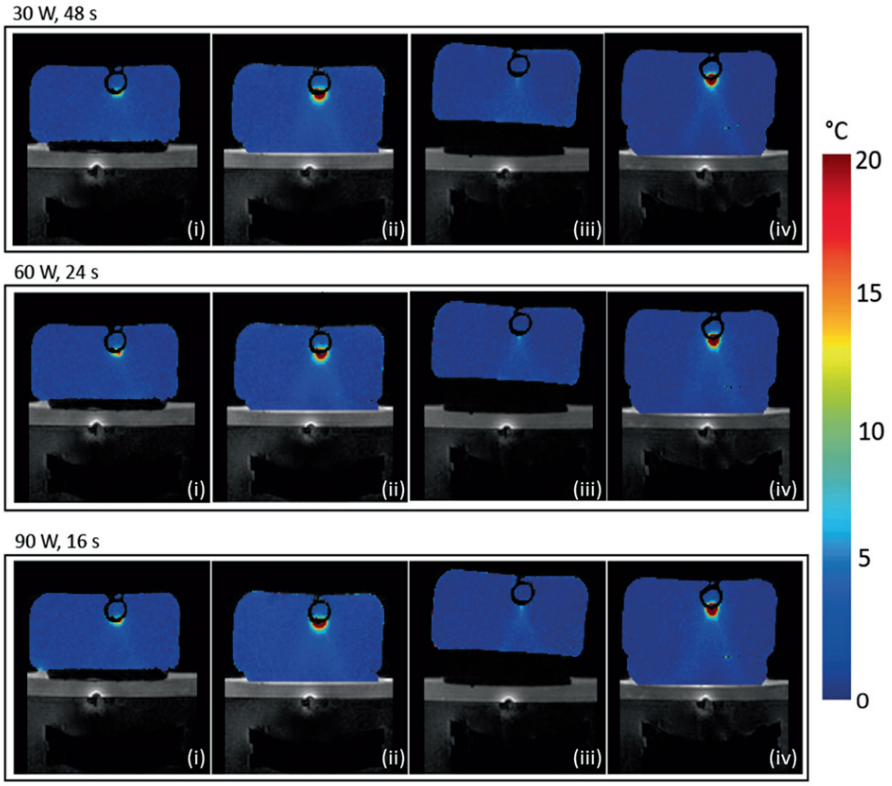

Figure 5.8: Maximum temperature increase in a transverse slice through the focus, measured with PRF-thermometry, overlayed with magnitude MR images for different sonication protocols. Phantom: core phantom + (i) 1 cm fat component, (ii) 1 cm gel component, (iii) 3 cm fat component, (iv) 3 cm gel component. Temperature information was not available in fat.

5.4. DISCUSSIONS

The palliative treatment success of bone metastases is determined by pain relief for the patient. However, pain relief cannot be assessed directly after the procedure. In our work, the main focus was on the energy on the bone surface. Since a direct measure of the energy is not possible in patients, it was calculated with a raytracer simulator. However, such a simulator is less usable in clinical settings, thus a simplified model was also used to estimate the energy on the bone surface. With the current analysis, we showed that both the raytracer and the geometrical method could be used to simulate changes in the energy values. Moreover, the presented results show that lower energy is delivered in the focal zone and lower temperature is reached at the target when a fat layer is present in the US beam. This means that when using EDBS the presence and thickness of prefocal fat should be taken into account, as it influences the amount of energy that reaches the bone surface. This effect has also been confirmed experimentally.

During a treatment session, EDBS estimates may be useful for different purposes: as an indicator of the expected effect after sonications and as tool to optimize the treat-

ment prior to sonications. In the first use-case, the EDBS estimates serve to evaluate sonications as an alternative for temperature or thermal dose. They can be especially useful when temperature maps are of limited quality and cannot be used for that purpose. In the second case, as possible tool to optimize the treatment, multiple scenarios can be envisioned. One scenario would be to first perform a test sonication while measuring the temperature elevation at the target with MR temperature mapping. If a clear temperature rise is observed in the target area close to the bone, then the ΔT observed during the test sonication can be used to derive the settings for power and sonication duration for the therapeutic sonications, which would aim at reaching a temperature elevation > 55 °C for a few seconds at the target. If a clear temperature rise cannot be observed during the test shot, because of the limitations of PRFS thermometry in and around bone [12], then the optimization of the delivered energy could be based on EDBS estimates. In this case, a calculation tool that can relate EDBS to the expected temperature rise for different fat and muscle layer thicknesses would be required. Such a tool could be based on reference cases, with known anatomical geometries, for which the temperature rise during sonications could well be measured. It remains to be investigated whether a simple model to estimate EDBS, like the model used in this study, would be suitable for this purpose in realistic patient cases and how variation in the composition of the metastasis, the geometry of the tissue layers in front of it, and cortical bone properties would influence the estimates.

The ratios found between energies without and with fat were comparable to the temperature ratios measured using PRFS thermometry. In scenarios without perfusion, like in this study, and in the presence of negligible heat diffusion, a linear relationship between energy and temperature rise is expected, since draining factors in the bioheat equation are then negligible [25]. However, in the experiments, small variations in temperature per sonication protocol were visible. These may be related to the partial volume effects in the temperature maps, and heat diffusion effects. For long sonication protocols, heat diffusion reduces the steepness of the temperature gradients and hence reduces the underestimation of the maximum temperature reached in the focus, by averaging over the (small) ROI.

In this phantom study, we found no evident preference towards sonications of long or short duration. In-vivo, however, this may be different. It has been observed in swine models that especially in soft tissues with high perfusion, sonications of higher power and shorter duration are preferred to maximize heating in the focal point while avoiding accumulative heating in the prefocal tissues [26]. Moreover, another study showed that for sonications on the bone, the short duration, high-power sonication produced a larger ablation zone compared to the long duration, low-power sonications [27].

The current analysis investigated the EDBS for single point sonications. However, in clinical procedures, electronic beam steering is applied to cover a target area and/or to control the size and location of the focal point of the ultrasound beam. The utility of the geometrical model for electronically steered sonications remains to be demonstrated, since the modelling of the US beam should be extended to a skewed and moving 3D cone.

In this work, the simulations were carried out assuming small incident angles. In practice, this assumption may not always hold; in these cases, the incident angle should be included in the models for calculating EDBS [28, 29].

In general, the uncertainties in the attenuation coefficient in fat is one of the main obstacles in applying the simulation methods and can lead to differences in the results, as reported in Figure 5.S1 where raytracer acoustic simulations with the attenuation coefficient in porcine fat are compared to those with human fat. In general, large discrepancies in the fat attenuation coefficient (between 5.65 and 27 Np/m at 1.2 MHz) are present in published data [22, 31–33]: this is probably due to the fact that the data were measured only in ex vivo tissues, at a range of different temperatures, in different states post excision, from different types of fat. One of the reasons for these large discrepancies is that fat changes substantially ex vivo over time [34]. In this study, we used fat from a butcher processed in order to obtain homogeneous fat layers of uniform thickness, necessary for the phantoms.
Performing real-time patient-specific ray tracer simulations during a therapy session is currently not realistic because they are highly time consuming. Stochastic ray tracer simulations are dependent on the number of rays used, and thus require a minimum number of rays to be included. Finally, the results may depend on the choice of the raytracer. The raytracer used in this study was selected based on its availability to our team, however, other acoustic simulators, e.g. angular spectrum of plane waves, could be considered instead [30]. Moreover, in this phantom study, the segmentation of tissues was straightforward, but in realistic patient cases, the results will also depend on the accuracy of the anatomical model created from the segmentations.
In conclusion, in the future, EDBS may play a role during the treatment session in executing therapy. For its proper use, we showed in this study that it is necessary to take into account the composition and the ultrasound properties (impedance, speed of sound, attenuation, ...) of the tissues between transducer and focus. Moreover, in this phantom setup, we did not observe variations in maximum temperature change nor qualitative variations in temperature distribution for different sonication protocols with the same emitted energy.

5.5. SUPPLEMENTARY MATERIALS

Figure 5.S1: Acoustic intensity maps simulated with the raytracer are shown for the experiments with 1-cm prefocal fat in Figure 5.S1, using two attenuation coefficients in fat: in human fat [21] and in porcine fat [22]. Differences between the two maps are clearly visible in the US beam path, the largest differences are observed in the focal area.

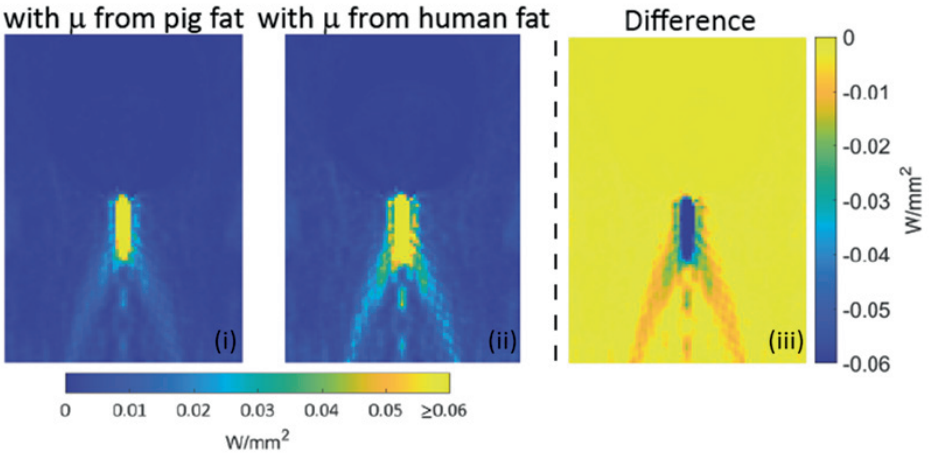

Figure 5.S1: Raytraced acoustic intensity distributions on the US beam path for the experiments with 1-cm fat as prefocal tissue in YX-plane, with Z being the direction, centered in the focal point, using (i) the attenuation coefficient in porcine fat [22] and (ii) the attenuation coefficient in human fat [21]. In (iii), the difference map is shown.

Figure 5.S2:

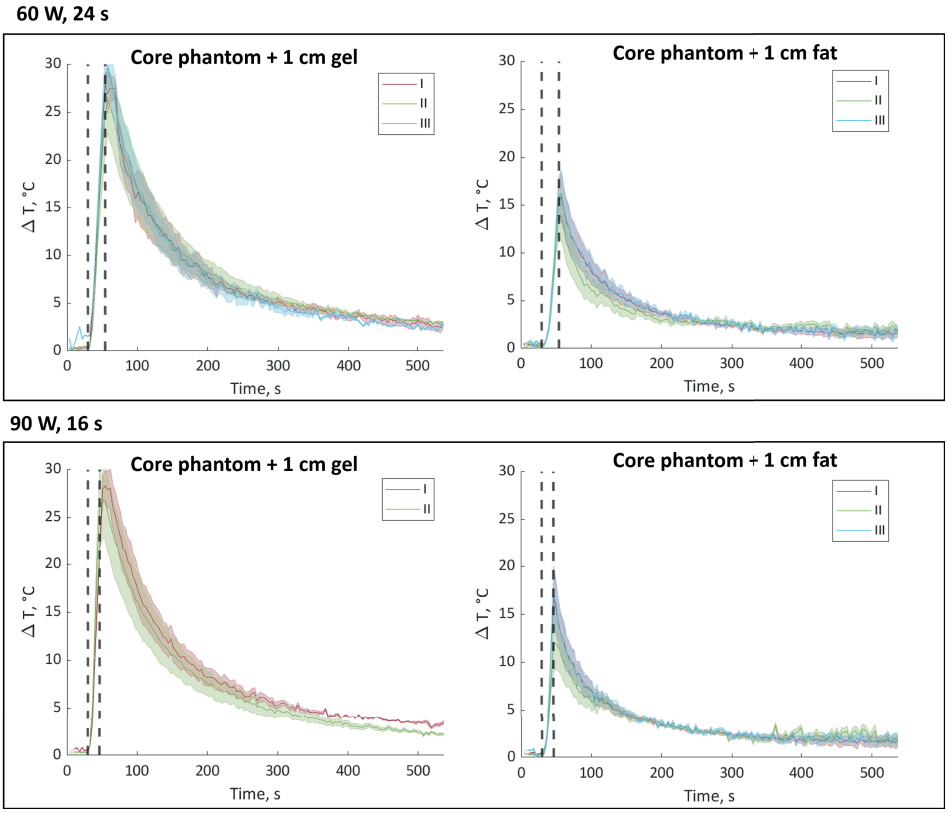

Figure 5.S2: Mean ± standard deviation of the temperature change over time measured with MRT in a 3D ROI (7 × 2 × 6 voxels) in the focal area in the gel during and after sonications of 60 W-24 s and 90 W-16 s in 2 phantoms. The dashed lines indicate the start and the end of the sonications. Each sonication was repeated 3 times per phantom experiment except for the experiment with 1 cm gel and 90 W-16s.

Figure 5.S3: For the phantom with 3-cm fat component, moderate temperature rises were observed in the prefocal area especially with sonication power of 30 W and duration 48 s (Figure 5.S2). This could be related to the higher US absorption of fat, which may have caused temperature rises in the fat and leads to heating in the gel in front of the focal area. This effect was stronger for sonications of longer duration.

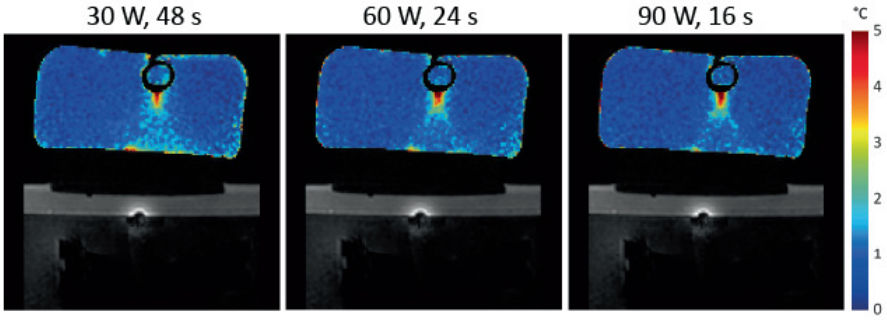

Figure 5.S3: Maximum temperature projection of transverse PRF-thermometry maps in the gel overlayed with magnitude MR images centered in the focal point for different sonication protocols. Phantom: core phantom + 3 cm fat component. Temperature information was not available in fat. NOTE: temperature scale is different from Figure 5.8

.

6

General Discussion

The MR-guided High-Intensity Focused Ultrasound (MR-HIFU) technique has the potential to revolutionize treatments of many diseases. In various hospitals worldwide, many scientists have been and still are working on different HIFU applications. This thesis presents contributions to improve bone metastases treatments, aiming to overcome some technological hurdles, identified on the therapy workflow. For the identified hurdles, solutions have been proposed, reported and discussed in the previous chapters and are summarized in the General Summary. General considerations of the proposed solutions in each therapy phase, their possible implementation in the clinics and future perspectives of this work in the field are discussed below.

6.1. TECHNICAL CONSIDERATIONS

"I have yet to see any problem, however complicated, which, when you looked at it in the right way, did not become still more complicated."
(Anderson P., Astounding Science Fiction, 1957) [179]

Therapy Planning
The therapy workflow of HIFU procedures on bone metastases consists of planning, monitoring, and evaluation of the treatment. Palliative HIFU treatments take advantage of bone heating to treat the nociceptive nerves in and around the lesion [39]. Therefore, it is extremely important to assess the bone distribution. This assessment is not trivial considering the heterogeneity of cortical bone distribution in bone metastases. Currently, during the HIFU procedure, the physician defines the region of treatment and identifies the skin and the bone cortex on the MR images in the treatment position. In combination with these MR images, the physician often reviews available cross-sectional imaging scans such as CT and MR (acquired prior to treatment, often not in treatment position) or calls for additional cross-sectional imaging to identify and confirm the location of the lesion. To simplify treatment planning, MRI-based bone visualization can be used to visualize bony and soft tissues in the treatment position. In this way, a facilitated depiction of the bone distribution is possible while discriminating aqueous and adipose tissues. This visualization could be achieved through the use of Ultrashort Echo Time (UTE) / Zero Echo Time (ZTE) sequences, especially thanks to recent developments [180]: Bone contrast has been improved combining UTE with effective suppression techniques (adiabatic inversion recovery, water- and fat-suppressed proton projection imaging, rescaled echo subtraction) [181]. However, such sequences are not always accessible in clinical practice, as their use requires changes in the MR hardware. A solution for MRI-based bone visualization which does not imply changes in the hardware is the use of synthetic CT (sCT) images, that has shown potential for HIFU treatment planning of transcranial procedures [96]. Combined sCT and MRI images enable the visualization of both bone and soft tissue and their use has been found feasible also for treatment planning of bone metastases (**Chapter 2**). The bone distribution resulted from both osteolysis and ossification is visible on sCT, demonstrating the suitability of such an approach to visualize bone lesions with CT-like contrasts to guide the treating physician while planning the treatment, because of the short sCT generation time (< 2min). The feasibility of the sCT approach was shown in the hip region, as femoral and pelvic bones are the most common sites for bone lesion treatments. The generalizability of the approach to less common sites for bone lesion treat-

ments as shoulder and ribs remains to be studied.
Synthetic CT studies are currently limited by the need of properly registering corresponding MR and CT data to provide a good model. This is challenging for palliative MR-HIFU procedures of bone metastases as only a small portion of patients with bone metastases are eligible for HIFU treatments and, often, CT and MR are not acquired in the same position. To assess whether the proposed neural network is adequate for clinical care or require further improvement, a clinical study testing the prospective use of sCT is warranted. In this type of study, sCT images could be generated prior to tissue sonication, with the patient in treatment position and they could be made available to physician, together with the pre-treatment scans.

Therapy Monitoring
Currently, the treatment is monitored with MR thermometry (MRT) based on the Proton Resonance Frequency Shift (PRFS) method. Although this method is easy to implement and clinically available, it only provides temperature estimates in aqueous tissues. However, adipose tissues such as bone marrow and subcutaneous fat are often present near bone lesions. Temperature monitoring in fat, besides water, could aid treatment efficacy and safety, allowing monitoring of the temperature increase in both adipose and aqueous tissues in the target area and avoiding unwanted thermal damage in the surrounding healthy tissues. Approaches for MRT in water and fat present in the literature exploit a combination of the PRFS method in water with T_1-based methods in fat. However, the T_1-based methods are often too slow to monitor the rapid temperature changes during HIFU ablation. A solution for rapid time-resolved T_1-mapping is the use of the Variable Flip Angle (VFA) method in 2D (**Chapter 3**). This method was found suitable to obtain accurate and precise T_1 estimates with a single flip angle pair over a wide range of T_1 values. This is relevant in the context of temperature monitoring, for which T_1 varies with temperature. In its current implementation, more than half of the total scan time of the 2D-VFA sequence is used to reach the steady-state of the magnetization, necessary to avoid errors in T_1 accuracy. However, strategies that manipulate the magnetization prior to steady state have been proposed to significantly decrease the total scan time [182–186]. The use of linearly increasing flip angles during magnetization preparation prior to data acquisition was found effective to consistently reduce the transient time [183]. The magnetization preparation consisted of several RF pulses with flip angles linearly increased to the flip angle chosen for the acquisition. This type of FA train may be applied to achieve faster steady state in the acquisition of the scans at two FAs of the 2D VFA method. This is particularly relevant for low FAs, which requires longer before reaching the steady state. Such train was also found to work for a wide range of T_1 [184], thus it would be interesting to try this strategy in the context of temperature monitoring.
Because of the T_1 dependence on temperature, the 2D-VFA T_1 method can be used to monitor the temperature in fat (**Chapter 4**). Various models for the absolute temperature dependence of T_1 have been described in literature, based on linear or exponential relationships [77, 78, 121, 187–189]. However, usually, only changes over a limited range of temperature (between the body temperature at 37°C, up to ablation temperature of 70°C) are measured with MRI. Although the absolute T_1-temperature relationship may differ, the relationship between T_1 change and temperature change

is similar in fat, as shown in different adipose tissues [189] and in breast samples [121]. Therefore, it is not expected that the choice of model would significantly change the results.

Interleaving PRFS and 2D-VFA T_1 thermometry enables temperature monitoring in water and fat during MR-HIFU sonications (**Chapter 4**). The interleaved acquisitions of PRFS and T_1 allow optimizing the sequences to obtain adequate precision for both measurements, minimizing trade-offs in the MR acquisition parameters. To minimize partial volume effects, it would be interesting to apply water suppression and water–fat separation methods to the interleaved sequence [158]. In case fat and water suppression techniques are not or cannot be used, combining the interleaved MRT with a multi-echo solution may be advantageous [87]. First, in a multi-echo approach the earlier echoes provide high SNR for T_1 determination, while the later echoes increase the precision of the PRFS method. Second, for applications in which motion is problematic, the multi-echo approach can be used to generate masks during the procedure to dynamically identify water and fat voxels. However, it may still be hard to disentangle motion-induced phase changes from temperature-related changes. Finally, the phase of fat may be used to assert the presence of field disturbances or drift and correct for them.

In addition, the T_1 information of fat is beneficial also to correct PRFS estimates in water for errors caused by heating-induced field distortions [190, 191].

In its current implementation, the temporal resolution of the interleaved MRT is 6s, which is not yet suitable to monitor the rapid temperature change induced by short-duration sonications of 16s, currently used in clinical procedures. Its temporal resolution should be improved before it can be approved for clinical use and coded into the clinical system. Strategies to improve the spatiotemporal resolution of PRFS/VFA-T_1 thermometry have been investigated in the last decades. They exploit non-Cartesian acquisition schemes, such as radial or golden-angle stack of stars [89, 192] and/or undersampling [193, 194], in combination with advanced reconstruction or a partial Fourier transform along the Cartesian-encoded slice direction and the use of a k-space-weighted image contrast filter [195]. A recent study proposed the use of a single reference variable flip angle for 3D simultaneous water and fat MRT [159]. This could be an immediate and easy approach to implement with the 2D interleaved MRT and it may reduce the acquisition time below 2s. However, a study of the potential problems of 2D acquisitions like the slice profile effect and an optimization of the sequence parameters, as FAs and TR, for single reference variable flip angle is needed.

Evaluation of Therapy Progress

At present, technical target indicators during the treatment, as temperature above a threshold, are based on MRT. However, MRT information from fat and bone are missing. A target indicator that does not rely on incomplete or partial data from MRT is preferable to predict the efficacy of the treatment. In this context, the acoustic energy (density) on the bone Surface (EDBS) was found to correlate with pain relief and, accordingly, with treatment success [83]. However, EDBS cannot be measured in patients. It was shown that a HIFU simulator based on ray tracing and a simple geometrical model, more suitable for clinical settings, may provide EDBS estimates (**Chapter 5**). These models allow study over the influence of different treatment conditions like son-

ication protocols and tissue compositions on EDBS. Among these conditions, it was found that when a fat layer is present in the US beam, consistently lower energies were delivered in the focal zone and lower temperatures were measured at the target. Hence, during the planning phase it is important not only to identify the bone distribution (**Chapter 2**) to target the beam, but also to evaluate the thickness of prefocal fat to set the emitted transducer energy. In fact, a target EDBS could be set prior to sonication. Knowing the thickness of prefocal fat from MR images, simulations could be used to adjust sonication power and duration, to reach the target EDBS.
Because of its correlation on a group level with pain relief [83], EDBS seems promising for implementation in clinical care, and for its use, the tissue composition between transducer and focus should be taken into account (**Chapter 5**). However, the proposed models investigated EDBS for single point sonications. During sonications, electronic beam steering may be applied to better control the size and location of the ablation zone of the ultrasound beam. The modelling of EDBS from electronically steered sonication cells would bring this parameter closer to clinical applications. Once this modelling will be implemented, the next step is validation for its use within a treatment session in a clinical study to know its potential as predictor of treatment efficacy.

6.2. FUTURE PERSPECTIVES

"One never notices what has been done; one can only see what remains to be done"
(Curie M., letter to Curie's brother, 1894)

In this thesis, technical developments to help HIFU clinical procedures have been proposed, developed and evaluated offline. Online implementation and evaluation of the suggested methods during HIFU treatments are natural next steps, taking into account the full complexity of the clinical procedures. After validation, the execution of a therapy workflow including the proposed methods, ideally as automated as possible, is important for their clinical adoption. Figure 6.1 shows a typical and a proposed therapy workflow for HIFU treatments on bone metastases.
After a patient has been found eligible for the HIFU treatment, a test session may be needed prior to the treatment, to test possible positionings of the patient for the treatment and to visualize the lesion on the MR-HIFU system. After the patient has been anesthetized, the treatment session starts with the positioning of the patient in the MR-HIFU system by physicians and technicians. Then, MR images are acquired to find the position that allows adequate acoustic window to the lesion. To find a suitable position, these initial steps are often repeated a variable number of times. After a suitable positioning has been achieved, the treatment is planned setting locations and energies of the sonications. Instead of combining MR with pretreatment CT scans for a facilitated placement of the sonications, synthetic CT images generated from treatment MR may be used to provide a more immediate depiction of the bone distribution in the lesion (**Chapter 2**). To set the energies of the sonications for the specific patient anatomy and tissue distribution, a target EDBS can be set, and the sonication protocols can be tuned for the aimed EDBS threshold (**Chapter 5**). At this point, the ablation of tissues can start. For monitoring the treatment, the interleaved PRFS-T_1 thermometry can aid offering a more complete overview of the temperature distribution both in soft tissues and in adipose tissues as subcutaneous fat and bone marrow (**Chapter 3-4**). If a clear

temperature rise is observed at the target, temperature maps are evaluated to assess whether suitable thermal damage was reached at the target (as rule of thumb, temperature above 55°C) or in case the temperature threshold was not achieved, to derive the settings for power and sonication duration for following therapeutic sonications. If a temperature rise in not clearly observed, then the optimization of the delivered energy could be based on EDSB estimates (**Chapter 5**). Finally, at the end of the treatment, the predictions of treatment outcome may be based instead of on MRT only, also on EDBS. This is especially useful in case of low-quality thermometry images. The treatment ends either when the time is up, adequate thermal damage has been achieved or when the target EDBS has been reached. After the treatment, the therapy outcome is assessed observing whether patients experience pain relief.
Before this proposed workflow could be implemented, in practice more steps are needed. In the remainder of this chapter, the role of the technology presented in this thesis and its possible implementation in the future are described in more detail.

The role of sCT for HIFU procedures on bone metastases
Synthetic CT images may have potential utility in the treatment planning phase, providing a qualitative image of the bone distribution with the patient in treatment position. However, some challenges need to be surmounted for the regular use of sCT in clinical HIFU procedures. Normally, sCT models are trained for specific applications, thus they depend on the input data, both in terms of anatomies involved and MR acquisition parameters. However, for clinical use, the models should be sufficiently robust to be able to accommodate input data with slightly different sequence parameters. To which extent this would be possible remains to be investigated.
Although it is unlikely that sCT would completely replace CT in HIFU procedures, in the context of palliative procedures on bone metastases, sCT imaging opens new perspectives for the visualization of bone and soft tissue for treatment planning [180].
Finally, more steps are necessary for the widespread adoption of sCT. First, sCT models must be approved by ethical regulators and integrated in clinical vendor systems or an AI deployment infrastructure should be connected to the Picture Archiving and Communication System (PACS) [196]. Then, the tools should be made available and taught to clinicians. Since AI-based images should be interpreted with care, practitioners need to be trained. These challenges will eventually be overcome, but their pace will be much slower than the continuous development of technology.

The role of MR for HIFU procedures on bone metastases
One of the biggest advantages that MR guidance brought to HIFU procedures is the ability to monitor temperature. MRT is a key tool for clinicians, as it allows to check the heat deposition on tissues. Currently, temperature monitoring is still limited in clinical care, but methods for combined water and fat MRT are increasingly investigated to broaden its scope of applicability. The main hurdle in combined MRT is its temporal resolution, which is low compared to PRFS thermometry. To date, 2D encoding remains the reference method for fast imaging, rendering approaches like interleaved MRT appealing for MRT applications. Once higher temporal resolution of 2D MRT is achieved, 2D temperature maps could be acquired from multiple orthogonal planes and interpolated to obtain 3D temperature distributions [197].

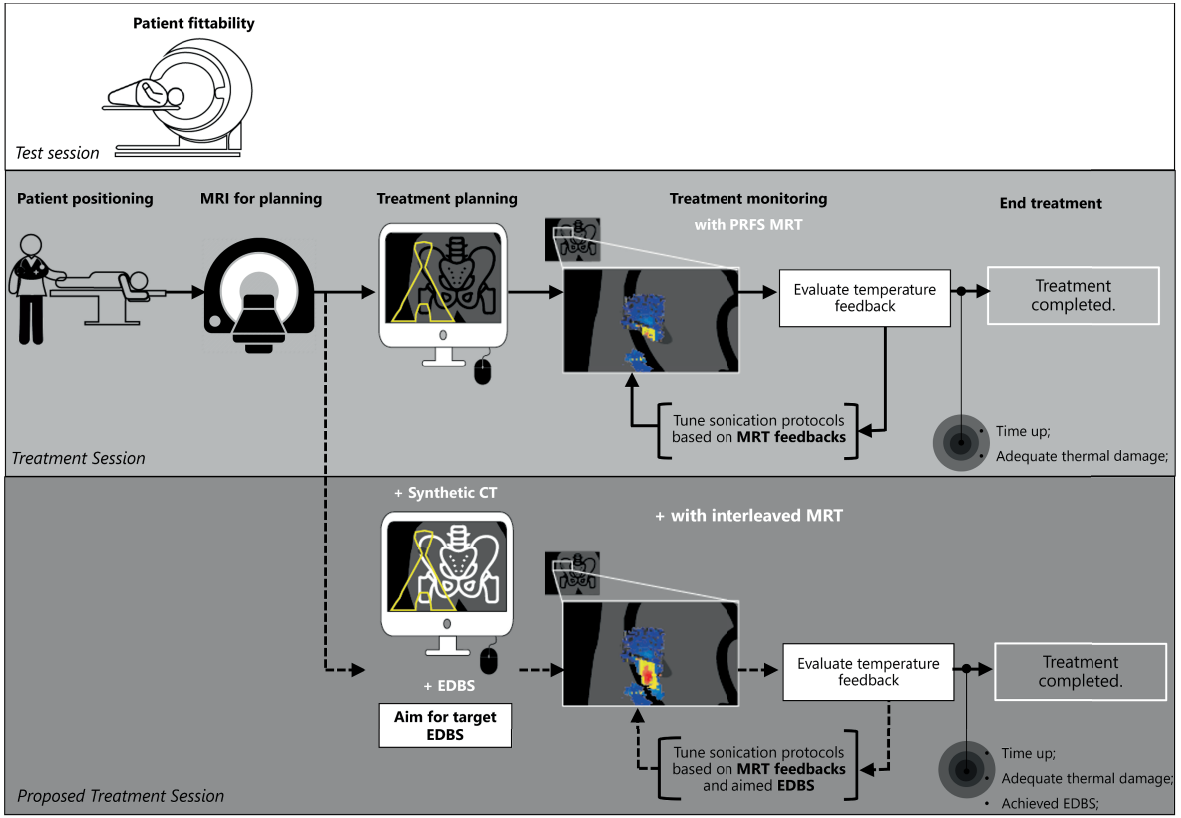

Figure 6.1: Illustration of the therapy workflow for HIFU treatments on bone metastases: before the treatment session, a test session may be planned to visualize the lesion and test possible treatment positioning. The treatment procedure starts with patient positioning and acquisition of MR images to check the position. Afterwards, planning and monitoring of the treatment take place: both therapy stages could be improved with the technology developed in this thesis. Prior to the ablation procedure, synthetic CT images may help in planning the sonications (**Chapter 2**) and a target EDBS could be set and used to tune the sonication energies (**Chapter 5**). During ablation, temperature could be monitored in water and fat with the interleaved thermometry (**Chapter 3-4**). At the end of the treatment, not only MRT, but also EDBS may be helpful to predict treatment outcome.

Furthermore, if the low temporal resolution of combined MRT could be improved, MR images can be used to predict the treatment effect from thermal tissue changes. Consequently, beside investigations of EDBS, as proposed in Chapter 5, image-based indicators should also be investigated. Potential image-based predictors have been proposed in the last few years, but their clinical relevance is yet to be validated [82, 83, 198, 199]. Diffusion-weighted MRI (DWI) contrast has shown promising preliminary results in preclinical and clinical studies [82, 198, 199]. The preclinical studies suggested that DWI can detect lesion formation [198] and changes in the muscle overlying the periosteum [199]caused by ablation, while the clinical study showed correlation between the apparent diffusion coefficient with pain relief [82].
However, these studies focused on tumor volume ablation, which is not considered to be the primary mechanism of pain palliation in HIFU procedures. Moreover, for the intraoperative use of DWI, a trained eye is required to evaluate differences in the DWI maps within few minutes after the sonication.
Faster postprocedural feedback may be provided by the "black band" feature [83], a rim around the bone of treated lesions visible on subtracted contrast-enhanced T_1-weighted images. It is thought to represent the devascularization of the periosteum. Its specificity as an indicator of pain relief is to be investigated, yet, the black band feature may provide useful information in the treatments of osteoblastic metastases.

The role of simulation for HIFU procedures on bone metastases
Simulation tools can be beneficial at multiple stages of the therapy.
Advanced simulators of HIFU procedures enable studies of the influence of single parameters on the output. Such a task is challenging in practice because of the intra-experimental variations. In Chapter 5, a raytracer simulator was used to investigate the influence of sonication power and duration, and of the thickness of prefocal fat on the acoustic energy near the bone target. Similar simulators have been used to study the impact of other relevant characteristics, such as the transducer shape [166] or of the angle of incidence [200], which otherwise would be hard to disentangle from the output (temperature or energy). Therefore, although raytracer tools may be less applicable in clinical practice owing to lengthy computational time, they are crucial tools for researchers to gain an understanding of the correlation and dependence of the parameters modelled.
While it is unlikely that simulation tools could completely substitute real measurements, it is easy to imagine scenarios in which hybrid approaches may combine simulation with per-treatment data. At the beginning of the treatment, one or more test sonications of low power are performed to confirm the accessibility of the US beam path into the target area. Information from test sonications as sonication power and duration as well as temperature estimates in the target, may be given as input to simulation to adjust the remainder of the sonications protocols to ensure suitable temperature rise at the target. During the treatment, simulation could be used to fill the gaps of MR thermometry. Temperature estimates measured with MRT could be given as input to a simulation model that calculate temperature in the voxels where MRT is not applicable, e.g., in bone, regions with low SNR or fat, if only PRFS- MRT is used. However, for its actual use in clinical procedures, a ray-tracing model should be able to compute the results in a short computation time (in the order of seconds). Another important

requirement is the knowledge of the acoustic and thermal tissue parameters. This is a known problem in the simulation field, since the temperature evolution predicted by the model depends strongly on the choice of the input parameter values (e.g., the US absorption coefficient).
Finally, other simulation tools could aid prior to the treatment to ensure whether the patient fits into the MR bore in treatment position, whether the lesion is reachable by ultrasound and whether an adequate acoustic window can be realized. Currently, these checks normally take place in the test session and the treatment day and in case the requirements cannot be met, can lead to delay or even cancellation of the whole procedure.
In order to enhance clinical adoption, it is important to avoid cancellations and/or delays of the procedures, leading to extra costs and waste of energies, and to reduce the number of patients excluded from HIFU treatments because of their physical dimensions. A trained eye could judge the patient suitability for the treatment (i.e., fit in the MRI bore), but this approach heavily relies on experience and opinion of the physician. Tools/algorithms may help researchers and physicians in this context. An algorithm has shown potential to predict the tumor coverage in two different positions for HIFU treatments in the pelvis from referral images [201]. Such an algorithm may be extended to include different possible treatment positions, by applying rigid rotations to the pelvis and trochanters. In this way, it could provide initial predictions about the patient suitability for the treatment knowing the MR bore size and the patient's body-mass-index and distribution of mass in patients. However, this type of models would be readily used as re-affirmation of the "known" cases rather than for the ones in doubt. Other solutions may take advantage of augmented reality, recently investigated to enable adequate target positioning outside the MRI scanner, improving the patient positioning workflow for the HIFU procedure [202].
The problem of patients not fitting into MR-HIFU systems could be solved at a higher level. Vendors can design HIFU tables that allow more freedom of movements to the patient or build MR-systems with larger bores compatible with the HIFU technology. Finally, hospitals when investing in interventional MRI with MR-HIFU might consider buying MRI scanners with large bore, as currently practised for radiotherapy.

Future Clinical Perspectives
The work realized in this thesis was part of a project funded by the Dutch Cancer Society and the Dutch Research Council with domain Applied and Engineering Sciences: Pain Reduction Of Metastases by THErmal UltraSound (PROMETHEUS). This project aimed at developing technology to improve the workflow of HIFU treatments on bone metastases. As for most of the works in a multidisciplinary environment, real improvements are made when people with different expertise collaborate. For this reason, both researchers and clinicians have been involved in the PROMETHEUS project. When research and clinics are combined, they can inspire each other: clinicians can identify the main problems in patient care, while researchers can provide some feasible solutions.
This thesis provided some solutions to specific problems. More technical problems have been discussed in the previous sections, while some open clinical challenges in the HIFU field are reported below.

First, the MR-HIFU technology is not yet suitable to treat patients with metastases in the spine, which is a common location of painful bone metastases. This is currently a big limitation, as most of the patients with painful bone metastases have lesions at this anatomical region [203]. At the moment, safety concerns prevent the treatment of spinal lesions, as thermal damage to spinal cord and/or nerve root could result in sever neurological deficits. Moreover, metastases in this region are often difficult to access by the ultrasound beam. Therefore, methods for accurate treatment monitoring and, possibly, for treatment behind the bone are required. If these methods could be implemented, HIFU procedures might gain interest also for oncological applications in the spine. Currently, non-surgical treatments of bone tumors on the spine consist of chemo- or radio- therapy. However, both therapies affect the bone marrow composition (both pathological and healthy) and may sometimes lead to complications [204]. In this context, it would be interesting to study the effect of HIFU on bone marrow composition, especially considering its attractiveness as radiation-free technique.
Additionally, the potentiality of HIFU as primary treatment for pain palliation and local tumor control has been debated. One study proposed HIFU as safe and effective primary treatment for pain palliation and with a potential role for local tumor control [65]. However, this study did not include a comparison with EBRT or a combination of EBRT and HIFU, which is now under investigation [70]. For this aim, data are being collected within the FURTHER trial, funded by the European Commission. To date, results of pre-FURTHER, the predecessor of the running FURTHER, trial showed that the combination of EBRT and HIFU is feasible and safe for patients [70]. Beside safety and efficacy, also the cost effectiveness of each treatment modality should be considered. This type of analysis may be interesting to assess the real value of such treatment modalities, to promote access to this technology and to provide further evidence for ongoing coverage expansion for certain patients. For example, when treatments are successful, HIFU improves the quality of life of patients [66] and is more cost effective over 2 years than medication only for pain palliation [205]. This may seem surprising, as HIFU, especially MR-HIFU, is expensive, but many factors as the increase in physical functioning, decrease of symptoms and pain relief after HIFU, need to be included in the analysis. Analysis of the cost effectiveness for EBRT, HIFU or a combination of both should then be evaluated.
Besides EBRT, HIFU treatments may benefit from therapeutic combination with other modalities, including cementoplasty [206, 207]. Together, they could promote bone consolidation, which is often needed in fragile patients.

The work in this thesis was performed to improve bone metastases procedures. However, many of the principles presented can be extrapolated for palliative care of low back pain, as lumbar facet joint arthrosis, and for ablation of benign tumors, as osteoid osteoma, and desmoid tumors. This might be especially relevant for osteoid osteoma procedures with the Profound Medical Sonalleve system, which were recently FDA approved [208]. This regulatory approval is the first to directly impact paediatric patients. Hopefully, widening the applicability of HIFU implies that many researchers and PhD students, after this author, will keep working on HIFU applications, which could be more easily available to an increasing number of patients. Following the natural path

of science, paved not with full stops, only commas,

"A work of science is never finished, only abandoned"
(Bhat I., Conversation with office mates, 2020)
- freely adapted from Leonardo da Vinci -

7

APPENDICES

English Summary
Nederlandse Samenvatting
Riassunto in Italiano
Bibliography
List of Publications
Acknowledgements
About the author

ENGLISH SUMMARY

High-Intensity Focused Ultrasound (HIFU) has the potential to treat many diseases non-invasively. Focusing an ultrasound beam onto a target in the human body can create a focal volume where the intensity is high enough to create rapid heating by absorption of ultrasound energy. This mechanism can be used to non-invasively ablate lesions, which is the concept of focused ultrasound surgery. In a palliative setting, it can also be exploited to ablate nerves that cause or conduct pain. HIFU can be combined with MR imaging (MR-HIFU) for image guidance of the treatment procedure. MRI is typically employed for treatment planning and targeting, to monitor the temperature in and around the lesion during the heating procedure, and to assess direct treatment effects.

In the work performed in this thesis, methods for MR-guided HIFU treatments have been investigated in the context of palliative treatments of bone metastases. Bone metastases are among the most common types of metastases, and they mostly arise from primary tumors as breast, prostate, and lung cancers. Bone metastases can be very painful, when the metastatic mass compresses and infiltrates the nerves in and around the bone.

Up to now, the standard modality for treatment of painful bone metastases has been local external beam radiotherapy (EBRT) combined with opioids. This therapy aims at eliminating tumor proliferation and reducing tumor-induced bone loss. However, it typically takes weeks after EBRT before pain relief is experienced. In addition, EBRT is not always effective (from literature, thirty percent of patients do not respond to EBRT) and re-irradiation is not always possible. For these reasons, MR-HIFU gained interest in the last decades as an alternative, fully non-invasive, treatment option, that may provide fast and durable pain palliation. The technique allows faster pain relief respect to EBRT, as it aims at directly ablating the nerves that cause the pain. It has shown promising results and further improvements in the technology will help to progress towards more wide-spread clinical adoption.

The work laid down in this thesis was aimed at improving some key technical aspects in the therapy workflow of MR-HIFU procedures on bone metastases. In particular, each chapter of this thesis focuses on a different need per treatment stage:

Treatment stage	**Question**	**Proposed solution in..**
Therapy planning	Where is the lesion located? How is the cortical bone distribution in and around the lesion?	***Chapter 2***
Therapy Monitoring	Are ablation temperatures reached in the lesion? No unwanted heating outside the target zone?	***Chapter 3 & 4***
Evaluation of Therapy progress	Is there a feature that can predict pain relief already during the treatment session? And how should this feature be used?	***Chapter 5***

During the therapy planning phase, MR images of the patient in treatment position are acquired to find the most suitable access for ultrasound to reach the target. For effective treatment planning the distribution of cortical bone in and around the lesion needs to be known, as bone is often targeted to ablate the periosteal nerves overlying the bone. The cortical bone distribution is more readily available on Computer Tomography (CT) images than on MR images, since MRI is more suitable to image soft tissues. However, a CT scan is not always acquired prior to HIFU treatment and even when it is, the patient's position and anatomy will differ between the CT and HIFU sessions. In **Chapter 2**, a method is described for improved depiction of bone, while maintaining adequate soft tissue contrasts. The method concerns the creation of images with CT-like contrast, called synthetic CT, from MR images. It is shown that this allows an easy interpretation of the bone distribution in treatment position, both in metastatic lesions with new bone formation, as well as for cases with bone erosion. MR images were used to discriminate aqueous and adipose tissues surrounding the lesion. This combined visualization has the potential to improve the planning stage of MR-HIFU procedures.

During the treatment procedure, ultrasound sonications are performed to ablate the target. In this phase, it is important to reach a threshold temperature, while avoiding unwanted heating of surrounding healthy tissues. MR thermometry (MRT) techniques can be used for temperature mapping during the sonications, but the MRT method currently available on clinical MR-HIFU systems can only be used for temperature monitoring in aqueous tissues. In practice, bone metastases are often found in proximity of fat-containing tissues, as bone marrow or subcutaneous adipose tissue. For this reason, **Chapters 3 and 4** focus on a method for combined MR thermometry in water and fat. In **Chapter 3**, a method for rapid time-resolved mapping of the longitudinal magnetic relaxation time (T_1) was proposed. It was shown that this method can deliver accurate and precise T_1 estimates, over a large range of T_1 values, and that it can be applied in-vivo. This is useful in the context of MR thermometry in fat, as methods based on the MR relaxation times have shown promising results to provide quantitative temperature information in adipose tissues. In **Chapter 4**, the rapid T_1 mapping method described in chapter 3 was used to monitor the temperature in fat and it was interleaved with water-based thermometry. Interleaved water and fat MR thermometry was used for monitoring an MR-HIFU ablation in an environment with both water and fat in the target zone. Moreover, the precision and the stability of the method for its use as a mapping technique in vivo have also been investigated.

Since pain relief is expected to manifest within days from the procedure, the therapeutic outcome is still unknown at the end of a therapy session. An MR imaging-based evaluation of the ablation zone, as is common for MR-HIFU ablations of uterine fibroids, is not straightforward when ablating thin periosteal layers. Thus, a feature or an indicator that could predict pain relief already during the treatment session is desired. Recently, the Energy Density on the Bone Surface (EDBS) has been proposed as promising candidate in this sense. For the use of this parameter during treatment sessions, it is important to know how it depends on conditions that typically vary between patient cases. Thus, in **Chapter 5**, an advanced HIFU simulator was used to investigate the influence of sonication protocols and tissue composition on EDBS estimates. A simplified model, with much shorter computation times and therefore potentially

more suitable for application in a clinical setting, was also tested, using the advanced simulator as reference. Both methods could be used to assess differences in the energy values for various combinations of conditions. Most notably, it was found that the thickness of the fat layer typically seen in the beam path between the transducer and the target zone considerably influences the amount of energy that reaches the bone. When considering to used EDBS estimates in clinical practice, the model for estimating EDBS should therefore take the fat layer into account.

NEDERLANDSE SAMENVATTING

High-Intensity Focused Ultrasound (HIFU) heeft het potentieel om vele ziekten niet-invasief te behandelen. Het focussen van een bundel van ultrasone golven op een doelwit in het menselijk lichaam kan een brandpuntsvolume creëren waarvan de intensiteit hoog genoeg is om een snelle verhitting te bewerkstelligen door absorptie van ultrasone energie. Dit mechanisme kan worden gebruikt voor niet-invasieve ablatie van laesies, wat het concept is van gefocusseerde ultrasone chirurgie. In een palliatieve setting kan het ook worden gebruikt voor de ablatie van zenuwen die pijn veroorzaken of geleiden. HIFU kan worden gecombineerd met MR-beeldvorming (MR-HIFU) voor beeldgeleiding van de behandelprocedure. MRI wordt typisch gebruikt voor het plannen en richten van de behandeling, om de temperatuur in en rond de laesie tijdens de verhittingsprocedure te monitoren, en om directe behandelingseffecten te beoordelen. In het werk dat voor dit proefschrift werd uitgevoerd zijn methoden voor MR-geleide HIFU-behandelingen onderzocht in de context van palliatieve behandelingen van botmetastasen. Botmetastasen behoren tot de meest voorkomende soorten metastasen en komen meestal voort uit primaire tumoren zoals borst-, prostaat-, en longkanker. Botmetastasen kunnen zeer pijnlijk zijn, in het bijzonder wanneer de uitgezaaide massa de zenuwen in en rond het bot samendrukt en infiltreert. Tot nu toe was de standaardbehandeling van pijnlijke botmetastasen lokale uitwendige radiotherapie (EBRT) in combinatie met opioïden. Deze therapie is gericht op het elimineren van tumorproliferatie en het verminderen van tumor-geïnduceerd botverlies. Het duurt echter meestal weken na EBRT voordat pijnverlichting wordt ervaren. Daarnaast is EBRT niet altijd effectief (uit de literatuur blijkt dat dertig procent van de patiënten niet op EBRT reageert) en is herbestraling niet altijd mogelijk. Om deze redenen heeft MR-HIFU de afgelopen decennia belangstelling gekregen als een alternatieve, volledig niet-invasieve behandelingsoptie, die een snelle en duurzame pijnverlichting kan bieden. Deze techniek maakt een snellere pijnverlichting mogelijk ten opzichte van EBRT, omdat zij gericht is op directe ablatie van de zenuwen die de pijn veroorzaken. MR-HIFU heeft veelbelovende resultaten opgeleverd en verdere verbeteringen van de technologie zullen helpen om vooruitgang te boeken in de richting van een bredere klinische acceptatie. Het werk dat in dit proefschrift is beschreven is gericht op het verbeteren van enkele belangrijke technische aspecten in de therapie-workflow van MR-HIFU-procedures voor botmetastasen. Ieder hoofdstuk van dit proefschrift richt zich in het bijzonder op een andere behoefte per behandelfase:

Behandelfase	**Vraag**	**Voorgestelde oplossing in...**
Therapie Planning	Waar bevindt de laesie zich? Hoe is de corticale botverdeling in en rond de laesie?	***Hoofdstuk 2***
Therapie Monitoring	Worden de ablatietemperaturen in de laesie bereikt? Geen ongewenste verwarming buiten het doelwit?	***Hoofdstuk 3 & 4***
Evaluatie van Therapievoortgang	Is er een kenmerk dat pijnverlichting al tijdens de behandelsessie kan voorspellen? En hoe moet dit kenmerk worden gebruikt?	***Hoofdstuk 5***

Tijdens de therapieplanningsfase worden MR-beelden van de patiënt in behandelingspositie verkregen om het meest geschikte traject voor de ultrasone bundel te vinden om het doelwit te bereiken. Voor een effectieve planning van de behandeling moet de verdeling van corticaal bot in en rond de laesie bekend zijn, aangezien bot vaak wordt gebruikt als doelwit voor de ablatie van periostale zenuwen die over het bot liggen. De corticale botverdeling is makkelijker te zien op computertomografie (CT)-beelden dan op MR-beelden, aangezien MRI meer geschikt is om zachte weefsels in beeld te brengen. Er wordt echter niet altijd een CT-scan gemaakt voorafgaand aan de HIFU-behandeling, en zelfs als dat wel het geval is zullen de positie en anatomie van de patiënt verschillen tussen de CT- en HIFU-sessies. In **Hoofdstuk 2** wordt een methode beschreven om een betere weergave van bot, met behoud van voldoende contrast van zachte weefsels, te bewerkstelligen. De methode betreft het maken van beelden met CT-achtig contrast, synthetische CT genaamd, uit MR-beelden. Er wordt aangetoond dat dit een gemakkelijke interpretatie van de botverdeling in behandelingspositie mogelijk maakt, zowel bij gemetastaseerde laesies met nieuwe botvorming, als voor gevallen waar er sprake is van boterosie. MR-beelden worden gebruikt om waterige- en vethoudende weefsels rond de laesie te onderscheiden. Deze gecombineerde visualisatie heeft het potentieel om de planningsfase van MR-HIFU-procedures te verbeteren. Tijdens de behandelingsprocedure worden ultrasone sonicaties uitgevoerd om ablatie van het doelwit te bewerkstelligen. In deze fase is het belangrijk om een drempeltemperatuur te bereiken, terwijl ongewenste opwarming van omliggende gezonde weefsels wordt vermeden. MR-thermometrie (MRT)-technieken kunnen worden gebruikt voor het in kaart brengen van de temperatuur tijdens de sonicaties, maar de MRT-methode die momenteel beschikbaar is op klinische MR-HIFU-systemen kan alleen worden gebruikt voor temperatuurmetingen in waterige weefsels. In de praktijk worden botmetastasen vaak gevonden in de nabijheid van vethoudende weefsels, zoals beenmerg of onderhuids vetweefsel. Om deze reden richten **Hoofdstukken 3 en 4** zich op een methode voor gecombineerde MR-thermometrie in water en vet. In **Hoofdstuk 3** wordt een methode voorgesteld voor het snel in kaart brengen van de longitudinale magnetische relaxatietijd (T_1). Er wordt aangetoond dat deze methode accurate en precieze T_1-schattingen kan opleveren over een groot bereik van T_1-waarden, en dat deze in vivo kan worden toegepast. Dit is nuttig in de context van MR-thermometrie in vet, aangezien methoden op basis van de MR-relaxatietijden veelbelovende resultaten hebben opgeleverd om kwantitatieve temperatuurinformatie in vetweefsel te verschaffen. In Hoofdstuk 4 wordt de snelle T_1 mapping methode, zoals beschreven in hoofdstuk 3, gebruikt om de temperatuur in vet te monitoren en wordt deze "interleaved" (afwisselend tussengevoegd) met op water gebaseerde thermometrie. Deze

"interleaved" water en vet MR-thermometrie werd gebruikt voor het monitoren van een MR-HIFU-ablatie in een omgeving met zowel water als vet in de omgeving van het doelwit. Verder zijn ook de precisie en de stabiliteit van de methode voor gebruik als een mapping-techniek in vivo onderzocht.
Aangezien pijnverlichting zich naar verwachting binnen enkele dagen na de procedure zal manifesteren, is het therapeutische resultaat aan het einde van een therapiesessie nog onbekend. Een op MR-beeldvorming gebaseerde evaluatie van de ablatiezone, zoals gebruikelijk is voor MR-HIFU-ablaties van myoom, is niet eenvoudig voor de ablatie van dunne periostale lagen. Een kenmerk of een indicator die pijnverlichting al tijdens de behandelsessie zou kunnen voorspellen is derhalve gewenst. Onlangs is de Energy Density on the Bone Surface (EDBS) voorgesteld als een veelbelovende kandidaat in deze context. Voor het gebruik van deze parameter tijdens behandelsessies is het belangrijk om te weten hoe deze afhangt van verschillende condities die doorgaans variëren tussen patiëntgevallen. Daarom werd in **Hoofdstuk 5** een geavanceerde HIFU-simulator gebruikt om de invloed van sonicatieprotocollen en weefselsamenstelling op EDBS-schattingen te onderzoeken. Een vereenvoudigd model, met veel kortere rekentijden en daardoor mogelijk geschikter voor toepassing in een klinische setting, werd ook getest, waarbij de geavanceerde simulator als referentie werd gebruikt. Beide methoden zouden kunnen worden gebruikt om verschillen in de energiewaarden voor verschillende combinaties van omstandigheden te beoordelen. De meest opvallende uitkomst van deze studie was dat de dikte van de vetlaag die typisch wordt gezien in het traject van de ultrasone bundel tussen de transducer en het doelwit, de hoeveelheid energie die het bot bereikt aanzienlijk beïnvloedt. In de overweging om EDBS-schattingen in de klinische praktijk te gebruiken moet het model voor het schatten van EDBS daarom rekening houden met de vetlaag.

RIASSUNTO IN ITALIANO

Gli ultrasuoni ad alta intensità (chiamati HIFU dall'inglese) sono promettenti per curare molte malattie in modo non invasivo. Focalizzare gli ultrasuoni in un punto del corpo umano permette di creare una regione di intensità così alta da generare calore molto rapidamente tramite l'assorbimento dell'energia degli ultrasuoni. Questo meccanismo può essere utilizzato per l'ablazione non invasiva (cioè la rimozione senza dover tagliare il paziente) delle lesioni, che è il concetto della chirurgia focalizzata con ultrasuoni. In poche parole, gli ultrasuoni focalizzati possono letteralmente bruciare i tumori. Inoltre, gli ultrasuoni focalizzati possono essere usati anche per cure palliative e in questo caso, aspirano a bruciare i nervi che causano il dolore. HIFU può essere combinato con la risonanza magnetica (tecnica chiamata MR-HIFU), per aiutare a visualizzare l'interno del paziente durante il trattamento. Qui, la risonanza magnetica viene in genere utilizzata sia per pianificare il trattamento e identificare dove bruciare, ma anche per misurare la temperatura durante la procedura, per valutare gli effetti diretti del trattamento (cioè, assicurandosi che la temperature raggiunga 55°C nel tessuto bersaglio e non surriscaldi i tessuti sani).
L'autrice di questa tesi si è concentrata a studiare metodi per interventi con HIFU guidati dalla risonanza magnetica, nel contesto di cure palliative delle metastasi ossee. Questo è importante perché le metastasi ossee sono tra i tipi più comuni di metastasi e derivano principalmente da tumori molto comuni come tumori al seno, alla prostata e ai polmoni. Le metastasi ossee possono essere molto dolorose, perché la massa tumorale spesso comprime i nervi che si trovano dentro e intorno all'osso.
Finora, la cura standard per il trattamento di dolorose metastasi ossee è stata la radioterapia locale a fasci esterni (tecnica chiamata EBRT) combinata con oppioidi.
Questa terapia mira a fermare il tumore e ridurre la rottura dell'osso causata dal tumore. Tuttavia, in genere servono settimane dopo l'EBRT prima che il paziente possa finalmente provare sollievo dal dolore. Inoltre, l'EBRT non è sempre efficace (da altri articoli scientifici sappiamo che il trenta per cento dei pazienti non risponde all'EBRT) e ridare nuovamente il trattamento al paziente tramite re-irradiazione non è sempre possibile. Per questi motivi, MR-HIFU ha guadagnato interesse negli ultimi decenni come alternativa, completamente non invasiva, che può fornire un rapido e duraturo sollievo dal dolore. La tecnica agisce più velocemente di EBRT perchè va a bruciare direttamente i nervi che causano il dolore. HIFU ha mostrato risultati promettenti e ulteriori studi e miglioramenti nella tecnologia aiuteranno a progredire verso un'adozione clinica più diffusa.
Il lavoro svolto in questa tesi era finalizzato al miglioramento di alcuni aspetti tecnici chiave nelle procedure MR-HIFU sulle metastasi ossee. In particolare, ogni capitolo di questa tesi si concentra su una diversa esigenza per fase di trattamento:

Fase di trattamento	**Domanda**	**Soluzione proposta in...**
Pianificazione	Dove si trova la metastasi? Quanto osso intero c'è intorno?	***Capitolo 2***
Monitoraggio	Si è raggiunta una temperature alta nel target? C'è stato surriscaldamento di tessuti sani?	***Capitolo 3 & 4***
Valutazione del progresso	C'è un parametro che può predire il sollievo del dolore? Si può usare durante l'intervento? E come può essere usato?	***Capitolo 5***

Durante la fase di pianificazione della terapia, vengono acquisite le immagini di risonanza del paziente in posizione non stardard, ma un po' inclinato sulla tavola contenente gli ultrasuoni, per trovare l'accesso più idoneo agli ultrasuoni per raggiungere il bersaglio. Per un'efficace pianificazione, è necessario sapere dove si trova l'osso vicino o intorno alla metastasi, poiché l'osso, in quanto solido e facile da scaldare, viene spesso fatto surriscaldare per bruciare i nervi intorno. Le ossa si vedono meglio nelle immagini di tomografia computerizzata (TAC) rispetto alle immagini di risonanza, perchè la risonanza magnetica è più adatta per l'immagine di tessuti molli, come muscoli, cervello, grasso, tumori. Tuttavia, una TAC non viene sempre acquisita prima dell'intervento con HIFU e anche quando lo è, la posizione e l'anatomia del paziente sono diverse tra le sessioni TAC e HIFU. Nel **Capitolo 2**, viene descritto un metodo per una migliore visualizzazione dell'osso, pur mantenendo un buon contrasto dei tessuti molli. Il metodo consiste nella creazione di immagini con contrasto simile alla TAC, chiamate finte TAC, generate con computer da immagini di risonanza. Abbiamo dimostrato in questo capitolo che questo permette di trovare facilmente le ossa con il paziente storto sulla tavola da ultrasuoni. Questo sia per le metastasi che formano nuovo osso, sia in quelle che lo distruggono, dato che purtroppo esistono entrambi i tipi di metastasi. Le immagini di risonanza sono ancora presenti ed utilizzate per vedere meglio i tessuti contenenti acqua e grasso che circondano la lesione. Questa combinazione ha il potenziale di migliorare la pianificazione delle procedure MR-HIFU.

Durante il vero e proprio trattamento, si eseguono le cosidette sonicazioni ad ultrasuoni per bruciare il bersaglio. In questa fase è importante raggiungere una temperatura di soglia (55°C), evitando il surriscaldamento indesiderato di tessuti sani circostanti. Esistono tecniche che permettono di misurare la temperature con la risonanza magnetica (chiamata MRT), ma il metodo MRT attualmente disponibile in clinica può essere utilizzato funziona solo per tessuti con maggioranza d'acqua. In pratica, le metastasi ossee si trovano spesso in prossimità di tessuti contenenti grasso, come il midollo osseo dentro le ossa o il tessuto grasso sottopelle. Per questo motivo, i **Capitoli 3 e 4** si concentrano su un metodo per la termometria a risonanza magnetica combinata per tessuti acquosi e grasse. Ora si fa un po' più tecnica la questione (scusa mamma). Nel **Capitolo 3** è stato proposto un metodo per la mappatura rapida del tempo di rilassamento magnetico longitudinale (T_1). È stato dimostrato che questo metodo può fornire stime accurate e precise di T_1, su un ampio intervallo di valori T_1, e che può essere applicato in vivo. Perché questo è utile? Perché altri studi hanno dimostrato che metodi basati sui tempi di rilassamento sono promettenti per misurare la temperatura nel grasso. Per questo, nel C**apitolo 4**, abbiamo utilizzato il

metodo di mappatura rapida T_1 descritto nel**Capitolo 3** per monitorare la temperatura nel grasso. E per aggiungerci le informazioni nei tessuti a maggioranza d'acqua, abbiamo alternato il metodo T_1 per il grasso con un metodo di termometria per tessuti a base d'acqua. La termometria alternata di metodi per acqua e grasso è stata utilizzata per monitorare un'ablazione MR-HIFU in un fantoccio fatto con acqua e grasso. Inoltre, sono state studiate anche la precisione e la stabilità del metodo per il suo utilizzo come tecnica di mappatura nelle persone.
Il sollievo dal dolore normalmente si manifesta entro pochi giorni dalla procedura, per cui al termine di una sessione di terapia, l'esito è sconosciuto. Una valutazione basata sulle immagini di risonanza, come è comune per le ablazione MR-HIFU di tumori come i fibroma uterini, non è semplice quando si bruciano nervi sottili. Pertanto, sarebbe desiderabile una caratteristica o un indicatore che possa predire il sollievo dal dolore già durante la sessione di trattamento. Recentemente, l'Energy Density on the Bone Surface (EDBS) è stato proposto come candidato promettente in questo senso. Per l'utilizzo di questo parametro durante gli interventi, è importante sapere come esso dipenda da condizioni che tipicamente variano da caso a paziente. Pertanto, nel **Capitolo 5**, è stato utilizzato un simulatore avanzato per studiare l'influenza dei protocolli di sonicazione (durata e potenza della bruciatura) e della composizione dei tessuti sulle stime EDBS. È stato inoltre testato un modello semplificato, con tempi di calcolo molto più brevi e quindi potenzialmente più adatto all'applicazione in ambito clinico, utilizzando come riferimento il simulatore avanzato. Entrambi i metodi potrebbero essere utilizzati per valutare le differenze nei valori energetici per varie combinazioni di condizioni. In particolare, è stato riscontrato che lo spessore dello strato di grasso tipicamente visto nel percorso del raggio tra il trasduttore ad ultrasuoni e la zona bersaglio influenza considerevolmente la quantità di energia che raggiunge l'osso. Quando si considera l'utilizzo delle stime EDBS nella pratica clinica, il modello per la stima dell'EDBS dovrebbe quindi tenere conto dello strato di grasso.

BIBLIOGRAPHY

1. Teng Q (2013) Structural biology: Practical NMR applications
2. Brown RW, Cheng YCN, Haacke EM, et al (2014) Magnetic Resonance Imaging: Physical Principles and Sequence Design: Second Edition
3. Winter L, Oberacker E, Paul K, et al (2016) Magnetic resonance thermometry: Methodology, pitfalls and practical solutions. International Journal of Hyperthermia 32:63–75. https://doi.org/10.3109/02656736.2015.1108462
4. Rieke V, Pauly KB (2008) MR thermometry. Journal of Magnetic Resonance Imaging 27:376–390
5. Odéen H, Parker DL (2019) Magnetic resonance thermometry and its biological applications – Physical principles and practical considerations. Progress in Nuclear Magnetic Resonance Spectroscopy 110:34–61.
https://doi.org/10.1016/j.pnmrs.2019.01.003
6. Germain D, Chevallier P, Laurent A, Saint-Jalmes H (2001) MR monitoring of tumour thermal therapy. Magnetic Resonance Materials in Physics, Biology and Medicine 13.
https://doi.org/10.1016/S1352-8661(01)00123-5
7. Zhang X, Landgraf L, Bailis N, et al (2021) Image-Guided High-Intensity Focused Ultrasound, A Novel Application for Interventional Nuclear Medicine? Journal of Nuclear Medicine 62:. https://doi.org/10.2967/jnumed.120.256230
8. Kremkau FW (1979) Cancer therapy with ultrasound: A historical review. Journal of Clinical Ultrasound 7:287–300
9. Maxwell A, Sapozhnikov O, Bailey M, et al (2012) Disintegration of Tissue Using High Intensity Focused Ultrasound: Two Approaches That Utilize Shock Waves. Acoustics Today 8:. https://doi.org/10.1121/1.4788649
10. Hijnen N, Langereis S, Grüll H (2014) Magnetic resonance guided high-intensity focused ultrasound for image-guided temperature-induced drug delivery. Advanced Drug Delivery Reviews 72
11. Evans KD, McClure A (2016) Using High-Intensity Focused Ultrasound as a Means to Provide Targeted Drug Delivery. Journal of Diagnostic Medical Sonography 32
12. Mesiwala AH, Farrell L, Wenzel HJ, et al (2002) High-intensity focused ultrasound selectively disrupts the blood-brain barrier in vivo. Ultrasound in Medicine and Biology 28:. https://doi.org/10.1016/S0301-5629(01)00521-X
13. Negishi Y, Yamane M, Kurihara N, et al (2015) Enhancement of blood–brain barrier permeability and delivery of antisense oligonucleotides or plasmid DNA to the brain by the combination of bubble liposomes and high-intensity focused ultrasound. Pharmaceutics 7:. https://doi.org/10.3390/pharmaceutics7030344
14. Deckers R, Moonen CTW (2010) Ultrasound triggered, image guided, local drug delivery. Journal of Controlled Release. https://doi.org/10.1016/j.jconrel.2010.07.117
15. Locke G, Pichardo S, Staruch R, et al (2020) A Phase I Prospective Clinical Trial Using Volumetric Magnetic Resonance-Guided High Intensity Focused Ultrasound (MR-HIFU) Hyperthermia (HT) Combined with Radiotherapy and Chemotherapy for Recur-

rent Rectal Cancer. International Journal of Radiation Oncology*Biology*
Physics 108:. https://doi.org/10.1016/j.ijrobp.2020.07.1870
16. Illing R, Emberton M (2006) Sonablate-500: Transrectal high-intensity focused ultrasound for the treatment of prostate cancer. Expert Review of Medical Devices 3:. https://doi.org/10.1586/17434440.3.6.717
17. Lynn JG, Zwemer RL, Chick AJ, Miller AE (1942) A new method for the generation and use of focused ultrasound in experimental biology. Journal of General Physiology 26:179–193. https://doi.org/10.1085/jgp.26.2.179
18. Fry WJ, Meyers R (1962) Ultrasonic method of modifying brain structures. Confin Neurol 22:315–327. https://doi.org/10.1159/000104377
19. Jagannathan J, Sanghvi NK, Crum L, et al (2014) High intensity focused ultrasound surgery (HIFU) of the brain: A Historical Perspective , With Modern Applications. Phys Med Biol 55:201–211.
https://doi.org/10.1227/01.NEU.0000336766.18197.8E.High
20. Hynynen K, Damianou C, Darkazanli A, et al (1992) On-line MRI monitored noninvasive ultrasound surgery. In: Proceedings of the Annual International Conference of the IEEE Engineering in Medicine and Biology Society, EMBS
21. Chapelon JY, Cathignol D, Cain C, et al (2000) New piezoelectric transducers for therapeutic ultrasound. Ultrasound in Medicine and Biology 26:.
https://doi.org/10.1016/S0301-5629(99)00120-9
22. Gelet A, Chapelon JY, Bouvier R, et al (1996) Treatment of prostate cancer with transrectal focused ultrasound: Early clinical experience. European Urology 29:.
https://doi.org/10.1159/000473739
23. Chapelon JY, Ribault M, Birer A, et al (1999) Treatment of localised prostate cancer with transrectal high intensity focused ultrasound. European Journal of Ultrasound 9:. https://doi.org/10.1016/S0929-8266(99)00005-1
24. Li S, Wu PH (2013) Magnetic resonance image-guided versus ultrasound-guided high-intensity focused ultrasound in the treatment of breast cancer. Chinese Journal of Cancer 32:441–452
25. Drost L, Hynynen K, Huang Y, et al (2020) Ultrasound-Guided Focused Ultrasound Treatment for Painful Bone Metastases: A Pilot Study. Ultrasound in Medicine and Biology 46:1455–1463.
https://doi.org/10.1016/j.ultrasmedbio.2020.01.032
26. Corradini S, Alongi F, Andratschke N, et al (2019) MR-guidance in clinical reality: Current treatment challenges and future perspectives. Radiation Oncology 14:1–12
27. Focused Ultrasound Foundation (2021) State of the Field
28. Siedek F, Yeo SY, Heijman E, et al (2019) Magnetic Resonance-Guided High-Intensity Focused Ultrasound (MR-HIFU): Technical Background and Overview of Current Clinical Applications (Part 1). RoFo Fortschritte auf dem Gebiet der Rontgenstrahlen und der Bildgebenden Verfahren 191:522–530. https://doi.org/10.1055/a-0817-5645
29. Hectors SJCG, Jacobs I, Moonen CTW, et al (2016) MRI methods for the evaluation of high intensity focused ultrasound tumor treatment: Current status and future needs. Magnetic Resonance in Medicine 75
30. Huisman M, Bosch MAAJ van den (2011) MR-guided high-intensity focused ultrasound for noninvasive cancer treatment. 161–166. https://doi.org/10.1102/1470-7330.2011.9041

31. Smith, Temkin, Shapiro H (1993) Thermal Effects of FUS on Bone Tissue. 06026:281–284
32. Bertrand A-S, Iannessi A, Natale R, et al (2018) Focused ultrasound for the treatment of bone metastases: effectiveness and feasibility. Journal of Therapeutic Ultrasound 6:1–9. https://doi.org/10.1186/s40349-018-0117-3
33. Huisman M, Lam MK, Bartels LW, et al (2014) Feasibility of volumetric MRI-guided high intensity focused ultrasound (MR-HIFU) for painful bone metastases. Journal of Therapeutic Ultrasound 2:1–10. https://doi.org/10.1186/2050-5736-2-16
34. Hurwitz MD, Ghanouni P, Kanaev S v., et al (2014) Magnetic resonance-guided focused ultrasound for patients with painful bone metastases: Phase III trial results. J Natl Cancer Inst. https://doi.org/10.1093/jnci/dju082
35. Corry PM, Barlogie B, Tilchen EJ, Armour EP (1982) Ultrasound-induced hyperthermia for the treatment of human superficial tumors. International Journal of Radiation Oncology, Biology, Physics 8:. https://doi.org/10.1016/0360-3016(82)90072-4
36. Scipione R, Anzidei M, Bazzocchi A, et al (2018) HIFU for Bone Metastases and other Musculoskeletal Applications. Seminars in Interventional Radiology 35:261–267. https://doi.org/10.1055/s-0038-1673363
37. Hynynen K, Deyoung D (1988) Temperature elevation at muscle-bone interface during scanned, focused ultrasound hyperthermia. International Journal of Hyperthermia 4:267–279. https://doi.org/10.3109/02656738809051103
38. Kopelman D, Inbar Y, Hanannel A, et al (2008) Magnetic resonance guided focused ultrasound surgery. Ablation of soft tissue at bone-muscle interface in a porcine model. European Journal of Clinical Investigation 38:268–275.
https://doi.org/10.1111/j.1365-2362.2008.01931.x
39. Nell DM, Myers MR (2010) Thermal effects generated by high-intensity focused ultrasound beams at normal incidence to a bone surface. J Acoust Soc Am 127:549–559. https://doi.org/10.1121/1.3257547
40. Catane R, Beck A, Inbar Y, et al (2007) MR-guided focused ultrasound surgery (MRgFUS) for the palliation of pain in patients with bone metastases - Preliminary clinical experience. Annals of Oncology 18:163–167.
https://doi.org/10.1093/annonc/mdl335
41. Liberman B, Gianfelice D, Inbar Y, et al (2009) Pain palliation in patients with bone metastases using MR-guided focused ultrasound surgery: A multicenter study. Annals of Surgical Oncology 16:140–146. https://doi.org/10.1245/s10434-008-0011-2
42. Fessenden P, Lee ER, Anderson TL, et al (1984) Experience with a Multitransducer Ultrasound System for Localized Hyperthermia of Deep Tissues. IEEE Transactions on Biomedical Engineering BME-31:
https://doi.org/10.1109/TBME.1984.325379
43. Marmor JB, Pounds D, Postic TB, Hahn GM (1979) Treatment of superficial human neoplasms by local hyperthermia induced by ultrasound. Cancer 43:.
https://doi.org/10.1002/1097-0142(197901)43:1<188::AID-CNCR2820430128>3.0.CO;2-7
44. Hynynen K, Shimm D, Anhalt D, et al (1990) Temperature distributions during clinical scanned, focused ultrasound hyperthermia treatments. International Journal of Hyperthermia 6:. https://doi.org/10.3109/02656739009140971
45. Siegel RL, Miller KD, Fuchs HE, Jemal A (2021) Cancer Statistics, 2021. CA: A Cancer

Journal for Clinicians 71:. https://doi.org/10.3322/caac.21654
46. Maroni P, Bendinelli P (2020) Bone, a secondary growth site of breast and prostate carcinomas: Role of osteocytes. Cancers (Basel) 12:1–14
47. Jiang W, Rixiati Y, Zhao B, et al (2020) Incidence, prevalence, and outcomes of systemic malignancy with bone metastases. Journal of Orthopaedic Surgery 28:. https://doi.org/10.1177/2309499020915989
48. Macedo F, Ladeira K, Pinho F, et al (2017) Bone metastases: An overview. Oncology Reviews 11:. https://doi.org/10.4081/oncol.2017.321 **49.** Mantyh PW (2014) Bone cancer pain: From mechanism to therapy. Current Opinion in Supportive and Palliative Care 8:83–90. https://doi.org/10.1097/SPC.0000000000000048
50. Dababou S, Marrocchio C, Scipione R, et al (2018) High-Intensity Focused Ultrasound for Pain Management in Patients with Cancer **51.** McGuire DB (2004) Occurrence of cancer pain. J Natl Cancer Inst Monogr
52. Caraceni A, Portenoy RK (1999) An international survey of cancer pain characteristics and syndromes. Pain 82:. https://doi.org/10.1016/S0304-3959(99)00073-1
53. Saito T, Toya R, Oya N (2019) Pain Response Rates After Conventional Radiation Therapy for Bone Metastases in Prospective Nonrandomized Studies: A Systematic Review. Practical Radiation Oncology 9
54. van der Linden YM, Lok JJ, Steenland E, et al (2004) Single fraction radiotherapy is efficacious: A further analysis of the Dutch Bone Metastasis Study controlling for the influence of retreatment. International Journal of Radiation Oncology Biology Physics 59:. https://doi.org/10.1016/j.ijrobp.2003.10.006
55. Saarto T, Janes R, Tenhunen M, Kouri M (2002) Palliative radiotherapy in the treatment of skeletal metastases. European Journal of Pain 6
56. McDonald R, Ding K, Brundage M, et al (2017) Effect of Radiotherapy on Painful Bone Metastases. JAMA Oncology 3:. https://doi.org/10.1001/jamaoncol.2016.6770
57. Johnstone C, Lutz ST (2014) External Beam Radiotherapy and Bone Metastases. Cancer Metastasis - Biology and Treatment 21:. https://doi.org/10.1007/978-94-007-7569-5_9
58. Huisman M, van den Bosch MAAJ, Wijlemans JW, et al (2012) Effectiveness of reirradiation for painful bone metastases: A systematic review and meta-analysis. International Journal of Radiation Oncology Biology Physics 84:. https://doi.org/10.1016/j.ijrobp.2011.10.080
59. Westhoff PG, Verdam MGE, Oort FJ, et al (2016) Course of Quality of Life After Radiation Therapy for Painful Bone Metastases: A Detailed Analysis From the Dutch Bone Metastasis Study. Radiation Oncology Biology 95:1391-1398. https://doi.org/10.1016/j.ijrobp.2016.03.032
60. Yeo SY, Elevelt A, Donato K, et al (2015) Bone metastasis treatment using magnetic resonance-guided high intensity focused ultrasound. Bone 81:513–523. https://doi.org/10.1016/j.bone.2015.08.025
61. Chan M, Dennis K, Huang Y, et al (2017) Magnetic Resonance–Guided High-Intensity-Focused Ultrasound for Palliation of Painful Skeletal Metastases: A Pilot Study. Technology in Cancer Research and Treatment 16:570–576. https://doi.org/10.1177/1533034616658576
62. Sapareto SA, Dewey WC (1984) Thermal dose determination in cancer therapy. International Journal of Radiation Oncology, Biology, Physics 10:787–800.

https://doi.org/10.1016/0360-3016(84)90379-1
63. ter Haar G, Coussios C (2007) High intensity focused ultrasound: Physical principles and devices. International Journal of Hyperthermia 23:.
https://doi.org/10.1080/02656730601186138
64. Brown MRD, Farquhar-Smith P, Williams JE, et al (2015) The use of high-intensity focused ultrasound as a novel treatment for painful conditions - A description and narrative review of the literature. British Journal of Anaesthesia 115
65. Napoli A, Anzidei M, Marincola BC, et al (2013) Primary pain palliation and local tumor control in bone metastases treated with magnetic resonance-guided focused ultrasound. Investigative Radiology.
https://doi.org/10.1097/RLI.0b013e318285bbab
66. Harding D, Giles SL, Brown MRD, et al (2018) Evaluation of Quality of Life Outcomes Following Palliative Treatment of Bone Metastases with Magnetic Resonance-guided High Intensity Focused Ultrasound: An International Multicentre Study. Clinical Oncology 30:233–242.
https://doi.org/10.1016/j.clon.2017.12.023
67. Bing F, Vappou J, de Mathelin M, Gangi A (2018) Targetability of osteoid osteomas and bone metastases by MR-guided high intensity focused ultrasound (MRgHIFU). International Journal of Hyperthermia 35:471–479.
https://doi.org/10.1080/02656736.2018.1508758
68. Wu F, Wang ZB, Lu P, et al (2004) Activated anti-tumor immunity in cancer patients after high intensity focused ultrasound ablation. Ultrasound in Medicine and Biology 30:1217–1222. https://doi.org/10.1016/j.ultrasmedbio.2004.08.003
69. Bucknor MD, Goel H, Pasco C, et al (2019) Bone remodeling following MR-guided focused ultrasound: Evaluation with HR-pQCT and FTIR. Bone 120:347–353.
https://doi.org/10.1016/j.bone.2018.11.009
70. Bartels MMTJ, Verpalen IM, Ferrer CJ, et al (2021) Clinical and Translational Radiation Oncology Combining radiotherapy and focused ultrasound for pain palliation of cancer induced bone pain; a stage I / IIa study according to the IDEAL framework. Clinical and Translational Radiation Oncology 27:57–63.
https://doi.org/10.1016/j.ctro.2021.01.005
71. Focused Ultrasound Foundation (2016) Bringing the Future into Focus
72. Amoretti N, Thariat J, Nouri Y, et al (2013) Imaging of bone metastases. Bulletin du Cancer 100:1109–1114. https://doi.org/10.1684/bdc.2013.1833
73. Johnson EM, Vyas U, Ghanouni P, et al (2017) Improved Cortical Bone Specificity in UTE MR Imaging. 695:684–695. https://doi.org/10.1002/mrm.26160
74. Noorda YH, Bartels LW, Huisman M, et al (2014) Registration of CT to pre-treatment MRI for planning of MR-HIFU ablation treatment of painful bone metastases. Physics in Medicine and Biology 59:4167–4179. https://doi.org/10.1088/0031-9155/59/15/4167
75. Lam MK, Huisman M, Nijenhuis RJ, et al (2015) Quality of MR thermometry during palliative MR-guided high-intensity focused ultrasound (MR-HIFU) treatment of bone metastases. Journal of Therapeutic Ultrasound 3:1–15.
https://doi.org/10.1186/s40349-015-0026-7
76. Baron P, Ries M, Deckers R, et al (2014) In vivo T2-based MR thermometry in adipose tissue layers for high-intensity focused ultrasound near-field monitoring. Magnetic Resonance in Medicine 72:1057–1064. https://doi.org/10.1002/mrm.25025

77. Hey S, de Smet M, Stehning C, et al (2012) Simultaneous T1 measurements and proton resonance frequency shift based thermometry using variable flip angles. Magnetic Resonance in Medicine 67:457–463. https://doi.org/10.1002/mrm.22987
78. Todd N, Diakite M, Payne A, Parker DL (2013) Hybrid proton resonance frequency/T1 technique for simultaneous temperature monitoring in adipose and aqueous tissues. Magnetic Resonance in Medicine 69:62–70.
https://doi.org/10.1002/mrm.24228
79. Diakite M, Odéen H, Todd N, et al (2014) Toward real-time temperature monitoring in fat and aqueous tissue during magnetic resonance-guided high-intensity focused ultrasound using a three-dimensional proton resonance frequency T1 method. Magnetic Resonance in Medicine 72:178–187. https://doi.org/10.1002/mrm.24900
80. Dewey WC (2009) Arrhenius relationships from the molecule and cell to the clinic. International Journal of Hyperthermia 25:3–20.
https://doi.org/10.1080/02656730902747919
81. Yarmolenko PS, Moon EJ, Landon C, et al (2011) Thresholds for thermal damage to normal tissues: An update. International Journal of Hyperthermia 27
82. Anzidei M, Napoli A, Sacconi B, et al (2016) Magnetic resonance-guided focused ultrasound for the treatment of painful bone metastases: role of apparent diffusion coefficient (ADC) and dynamic contrast enhanced (DCE) MRI in the assessment of clinical outcome. Radiologia Medica 121:905–915.
https://doi.org/10.1007/s11547-016-0675-9
83. Bitton RR, Rosenberg J, LeBlang S, et al (2021) MRI-Guided Focused Ultrasound of Osseous Metastases: Treatment Parameters Associated With Successful Pain Reduction. Invest Radiol 56:141–146. https://doi.org/10.1097/RLI.0000000000000721
84. Boulanger M, Nunes JC, Chourak H, et al (2021) Deep learning methods to generate synthetic CT from MRI in radiotherapy: A literature review. Physica Medica 89:265–281.
https://doi.org/10.1016/J.EJMP.2021.07.027
85. Jans LBO, Chen M, Elewaut D, et al (2021) MRI-based Synthetic CT in the Detection of Structural Lesions in Patients with Suspected Sacroiliitis: Comparison with MRI. Radiology 298:343–349. https://doi.org/10.1148/RADIOL.2020201537
86. Staartjes VE, Seevinck PR, Vandertop WP, et al (2021) Magnetic resonance imaging-based synthetic computed tomography of the lumbar spine for surgical planning: a clinical proof-of-concept. Neurosurg Focus 50:1–7.
https://doi.org/10.3171/2020.10.FOCUS20801
87. Poorman ME, Braškutė I, Bartels LW, Grissom WA (2019) Multi-echo MR thermometry using iterative separation of baseline water and fat images. Magnetic Resonance in Medicine 81:2385–2398. https://doi.org/10.1002/mrm.27567
88. Svedin BT, Parker DL (2017) Technical Note: The effect of 2D excitation profile on T1 measurement accuracy using the variable flip angle method with an average flip angle assumption: The. Medical Physics 44:5930–5937.
https://doi.org/10.1002/mp.12513
89. Zhang L, Armstrong T, Li X, Wu HH (2019) A variable flip angle golden-angle-ordered 3D stack-of-radial MRI technique for simultaneous proton resonant frequency shift and T1-based thermometry. Magnetic Resonance in Medicine
82:2062–2076. https://doi.org/10.1002/mrm.27883 **90.** Deoni SCL, Rutt BK, Peters TM (2003) Rapid combined T1 and T2 mapping using gradient recalled acquisition in the

steady state. Magnetic Resonance in Medicine 49:515–526.
https://doi.org/10.1002/mrm.10407
91. Najafi A, Sartoretti E, Binkert CA (2019) Sacroiliac Joint Ablation Using MR-HIFU. CardioVascular and Interventional Radiology 42:1363–1365.
https://doi.org/10.1007/s00270-019-02263-0
92. Napoli A, Bazzocchi A, Scipione R, et al (2017) Noninvasive therapy for osteoid osteoma: A prospective developmental study with MR Imaging-guided high-intensity focused ultrasound. Radiology 285:186–196.
https://doi.org/10.1148/radiol.2017162680
93. Willemsen K, Ketel MHM, Zijlstra F, et al (2021) 3D-printed saw guides for lower arm osteotomy, a comparison between a synthetic CT and CT-based workflow. 3D Printing in Medicine 7:13. https://doi.org/10.1186/s41205-021-00103-x
94. Zijlstra F, Willemsen K, Florkow MC, et al (2019) CT synthesis from MR images for orthopedic applications in the lower arm using a conditional generative adversarial network. In: Proceedings of the SPIE Medical Imaging Meeting, San Diego, California. SPIE, p 109491J
95. Florkow MC, Willemsen K, Zijlstra F, et al (2021) MRI-based synthetic CT shows equivalence to conventional CT for the morphological assessment of the hip joint. Journal of Orthopaedic Research. https://doi.org/10.1002/jor.25127
96. Su P, Guo S, Roys S, et al (2020) Transcranial MR imaging-guided focused ultrasound interventions using deep learning synthesized CT. American Journal of Neuroradiology 41:1841–1848.
https://doi.org/10.3174/ajnr.A6758
97. Yushkevich PA, Piven J, Hazlett HC, et al (2006) User-guided 3D active contour segmentation of anatomical structures: Significantly improved efficiency and reliability. Neuroimage 31:1116–1128. https://doi.org/10.1016/j.neuroimage.2006.01.015
98. Besl PJ, McKay ND (1992) A Method for Registration of 3-D Shapes. IEEE Transactions on Pattern Analysis and Machine Intelligence 14:239–256.
https://doi.org/10.1109/34.121791
99. Kuiper RJA, van Stralen M, Sakkers RJB, et al (2021) CT to MR registration of complex deformations in the knee joint through dual quaternion interpolation of rigid transforms. Physics in Medicine & Biology 66:175024.
https://doi.org/10.1088/1361-6560/ac1769
100. Klein S, Staring M, Murphy K, et al (2010) Elastix: A toolbox for intensity-based medical image registration. IEEE Transactions on Medical Imaging 29:196–205.
https://doi.org/10.1109/TMI.2009.2035616
101. Ronneberger O, Fischer P, Brox T (2015) U-net: Convolutional networks for biomedical image segmentation. Lecture Notes in Computer Science (including subseries Lecture Notes in Artificial Intelligence and Lecture Notes in Bioinformatics) 9351:234–241.
https://doi.org/10.1007/978-3-319-24574-4_28
102. Milletari F, Navab N ASA (2016) V-Net: fully convolutional neural networks for volumetric medical image segmentation. Proceedings of the 4th International Conference on 3D Vision, Stanford, California 565–571
103. Florkow MC, Zijlstra F, Willemsen K, et al (2020) Deep learning–based MR-to-CT synthesis: The influence of varying gradient echo–based MR images as input channels. Magnetic Resonance in Medicine 83:1429–1441.

https://doi.org/10.1002/mrm.28008
104. Kingma DP, Ba JL (2015) Adam: A method for stochastic optimization. 3rd International Conference on Learning Representations, ICLR 2015 - Conference Track Proceedings 1–15
105. Dice LR (1945) Measures of the Amount of Ecologic Association Between Species. Ecology 26:297–302. https://doi.org/10.2307/1932409 **106.** Kim HS, Park SB, Lo SS, et al (2012) Bidirectional local distance measure for comparing segmentations. Medical Physics 39:. https://doi.org/10.1118/1.4754802
107. Christensen DL, Nappo KE, Wolfe JA, et al (2019) Proximal femur hounsfield units on CT colonoscopy correlate with dual-energy X-ray absorptiometry. Clinical Orthopaedics and Related Research 477:850–860.
https://doi.org/10.1097/CORR.0000000000000480
108. Kim YS, Lee S, Sung YK, Lee BG (2016) Assessment of osteoporosis using pelvic diagnostic computed tomography. Journal of Bone and Mineral Metabolism 34:457–463.
https://doi.org/10.1007/s00774-015-0684-0
109. Modena D, Baragona M, Bosnacki D, et al (2018) Modeling the interference between shear and longitudinal waves under high intensity focused ultrasound propagation in bone. Physics in Medicine and Biology 63:.
https://doi.org/10.1088/1361-6560/aaef14
110. ten Eikelder HMM, Bošnački D, Elevelt A, et al (2016) Modelling the temperature evolution of bone under high intensity focused ultrasound. Physics in Medicine and Biology 61:1810–1828. https://doi.org/10.1088/0031-9155/61/4/1810
111. Kanberoglu K, Kantarci F, Yilmaz MH (2005) Reactive sclerosis: Hyperintense appearance on T2-weighted magnetic resonance imaging. Acta Radiologica 46:708–715.
https://doi.org/10.1080/02841850510021788
112. Florkow MC, Zijlstra F, Kerkmeijer LGW, et al (2019) The impact of MRI-CT registration errors on deep learning-based synthetic CT generation. In: Proceedings of the SPIE Medical Imaging Meeting, San Diego, California. SPIE, p 1094938
113. El-Samie HAEKA, El-Ghany HSA (2015) The value of added opposed/in phase MRI sequences in characterization of the focal vertebral bone marrow lesions in oncology patients. Egyptian Journal of Radiology and Nuclear Medicine 46:727–732.
https://doi.org/10.1016/j.ejrnm.2015.05.004 **114.** Taylor AJ, Salerno M, Dharmakumar R, Jerosch-Herold M (2016) T1 Mapping Basic Techniques and Clinical Applications. JACC: Cardiovascular Imaging 9:67–81
115. Dekkers IA, Lamb HJ (2018) Clinical application and technical considerations of T1 and T2* mapping in cardiac, liver, and renal imaging. British Journal of Radiology 91
116. Hattingen E, Müller A, Jurcoane A, et al (2017) Value of quantitative magnetic resonance imaging T1-relaxometry in predicting contrast-enhancement in glioblastoma patients. Oncotarget 8:53542–53551.
https://doi.org/10.18632/oncotarget.18612
117. Look DC, Locker DR (1970) Time saving in measurement of NMR and EPR relaxation times. Review of Scientific Instruments 41:250–251.
https://doi.org/10.1063/1.1684482
118. Messroghli DR, Radjenovic A, Kozerke S, et al (2004) Modified look-locker inversion recovery (MOLLI) for high-resolution T 1 mapping of the heart. Magnetic Reso-

nance in Medicine 52:141–146. https://doi.org/10.1002/mrm.20110
119. Yuan J, Chow SKK, Yeung DKW, et al (2012) Quantitative evaluation of dual-flip-angle T1 mapping on DCE-MRI kinetic parameter estimation in head and neck. Quant Imaging Med Surg 2:245–24553.
https://doi.org/10.3978/j.issn.2223-4292.2012.11.04
120. Herrmann K, Erokwu BO, Johansen ML, et al (2016) Dynamic quantitative T1 mapping in orthotopic brain tumor xenografts. Translational Oncology 9:147–154.
https://doi.org/10.1016/j.tranon.2016.02.004
121. Baron P, Deckers R, Knuttel FM, Bartels LW (2015) T1 and T2 temperature dependence of female human breast adipose tissue at 1.5 T: Groundwork for monitoring thermal therapies in the breast. NMR in Biomedicine 28:1463–1470.
https://doi.org/10.1002/nbm.3410
122. Pineda FD, Medved M, Fan X, Karczmar GS (2016) B1 and T1 mapping of the breast with a reference tissue method. Magnetic Resonance in Medicine 75:1565–1573.
https://doi.org/10.1002/mrm.25751
123. Sung K, Daniel BL, Hargreaves BA (2013) Transmit B 1 + field inhomogeneity and T1 estimation errors in breast DCE-MRI at 3 tesla. Journal of Magnetic Resonance Imaging 38:454–459. https://doi.org/10.1002/jmri.23996
124. Spanakis M, Kontopodis E, van Cauter S, et al Assessment of DCE-MRI parameters for brain tumors through implementation of physiologically-based pharmacokinetic model approaches for Gd-DOTA. Journal of Pharmacokinetics and Pharmacodynamics 43:. https://doi.org/10.1007/s10928-016-9493-x
125. Parker GJM, Barker GJ, Tofts PS (2001) Accurate multislice gradient echo T1 measurement in the presence of non-ideal RF pulse shape and RF field nonuniformity. Magnetic Resonance in Medicine 45:838–845.
https://doi.org/10.1002/mrm.1112
126. Dieringer MA, Deimling M, Santoro D, et al (2014) Rapid parametric mapping of the longitudinal relaxation time T1 using two-dimensional variable flip angle magnetic resonance imaging at 1.5 Tesla, 3 Tesla, and 7 Tesla. PLoS ONE 9:3–10.
https://doi.org/10.1371/journal.pone.0091318
127. Homer J, Beevers MS (1985) Driven-equilibrium single-pulse observation of T1 relaxation. A reevaluation of a rapid new method for determining NMR spin-lattice relaxation times. Journal of Magnetic Resonance (1969) 63:287–297.
https://doi.org/10.1016/0022-2364(85)90318-X
128. Blüml S, Schad LR, Stepanow B, Lorenz WJ (1993) Spin-lattice relaxation time measurement by means of a TurboFLASH technique. Magnetic Resonance in Medicine 30:289–295. https://doi.org/10.1002/mrm.1910300304
129. Schabel MC, Morrell GR (2009) Uncertainty in T1 mapping using the variable flip angle method with two flip angles. Physics in Medicine and Biology 54:.
https://doi.org/10.1088/0031-9155/54/1/N01
130. Xiang QS (1996) Inversion recovery image reconstruction with multiseed region-growing spin reversal. Journal of Magnetic Resonance Imaging.
https://doi.org/10.1002/jmri.1880060511
131. Yarnykh VL (2007) Actual Flip-Angle Imaging in the Pulsed Steady State: A Method for Rapid Three-Dimensional Mapping of the Transmitted Radiofrequency Field.
200:192–200. https://doi.org/10.1002/mrm.21120

132. Bipin Mehta B, Coppo S, Frances McGivney D, et al (2019) Magnetic resonance fingerprinting: a technical review. Magnetic Resonance in Medicine 81:25–46
133. Ben-Eliezer N, Sodickson DK, Block KT (2015) Rapid and accurate T2 mapping from multi-spin-echo data using bloch-simulation-based reconstruction. Magnetic Resonance in Medicine 73:809–817. https://doi.org/10.1002/mrm.25156
134. van Gelderen P, Jiang X, Duyn JH (2016) Effects of magnetization transfer on T1 contrast in human brain white matter. Neuroimage 128:85–95.
https://doi.org/10.1016/j.neuroimage.2015.12.032
135. Deoni SCL, Rutt BK, Arun T, et al (2008) Gleaning multicomponent T1 and T2 information from steady-state imaging data. Magnetic Resonance in Medicine 60:
1372–1387. https://doi.org/10.1002/mrm.21704
136. Stikov N, Boudreau M, Levesque IR, et al (2015) On the accuracy of T1 mapping: Searching for common ground. Magnetic Resonance in Medicine 73:514–522. https://doi.org/10.1002/mrm.25135
137. Bane O, Hectors SJ, Wagner M, et al (2018) Accuracy, repeatability, and interplatform reproducibility of T1 quantification methods used for DCE-MRI: Results from a multicenter phantom study. Magnetic Resonance in Medicine 79:2564–2575.
https://doi.org/10.1002/mrm.26903
138. Yarnykh VL (2010) Optimal radiofrequency and gradient spoiling for improved accuracy of T1 and B1 measurements using fast steady-state techniques. Magnetic Resonance in Medicine 63:1610–1626. https://doi.org/10.1002/mrm.22394
139. Chang LC, Cheng GK, Basser PJ, Pierpaoli C (2008) Linear least-squares method for unbiased estimation of T1 from SPGR signals. Magnetic Resonance in Medicine. https://doi.org/10.1002/mrm.21669
140. Senneville BD de, Mougenot C, Grenier N (2007) MR thermometry for monitoring tumor ablation. 2401–2410. https://doi.org/10.1007/s00330-007-0646-6
141. Winter L, Oberacker E, Paul K, et al (2016) Magnetic resonance thermometry: Methodology , pitfalls and practical solutions Magnetic resonance thermometry:
Methodology , pitfalls and practical solutions. 6736:.
https://doi.org/10.3109/02656736.2015.1108462
142. Kuroda K (2005) Non-invasive MR thermography using the water proton chemical shift. International Journal of Hyperthermia 21:547–560.
https://doi.org/10.1080/02656730500204495
143. Stollberger R, Ascher PW, Huber D, et al (1998) Temperature monitoring of interstitial thermal tissue coagulation using MR phase images. Journal of Magnetic Resonance Imaging 8:188–196. https://doi.org/10.1002/jmri.1880080132
144. Mougenot C, Köhler MO, Enholm J, et al (2011) Quantification of near-field heating during volumetric MR-HIFU ablation. Medical Physics 38:272–282.
https://doi.org/10.1118/1.3518083
145. Lam MK, de Greef M, Bouwman JG, et al (2015) Multi-gradient echo MR thermometry for monitoring of the near-field area during MR-guided high intensity focused ultrasound heating. Physics in Medicine and Biology 60:7729–7746.
https://doi.org/10.1088/0031-9155/60/19/7729
146. Parker DL (1984) Applications of NMR Imaging in Hyperthermia: An Evaluation of the Potential for Localized Tissue Heating and Noninvasive Temperature Monitoring. IEEE Transactions on Biomedical Engineering BME-31:161–167.

https://doi.org/10.1109/TBME.1984.325382
147. Kuroda K, Iwabuchi T, Obara M, et al (2011) Temperature dependence of relaxation times in proton components of fatty acids. Magnetic Resonance in Medical Sciences 10:177–183. https://doi.org/10.2463/mrms.10.177
148. Henningsson M, Mens G, Koken P, et al (2015) A new framework for interleaved scanning in cardiovascular MR: Application to image-based respiratory motion correction in coronary MR Angiography. Magnetic Resonance in Medicine 73:692–696. https://doi.org/10.1002/mrm.25149
149. Braskute I, Deckers R, Viergever MA, et al (2018) Bloch simulation-based correction for 2D VFA T1 mapping for fat MR thermometry. Proc Intl Soc Mag Reson Med 26:
150. Glover GH, Schneider E (1991) Three-point dixon technique for true water/fat decomposition with B0 inhomogeneity correction. Magnetic Resonance in Medicine 18:371–383. https://doi.org/10.1002/mrm.1910180211
151. Lefebvre G (2015) One sequence , many benefits in musculoskeletal MRI. Fieldstrength 18–21
152. Lena B, Bos C, Moonen CTW, et al (2019) Flip angle optimization and in vitro demonstration of 2D DESPOT1-based fat thermometry. Proc Intl Soc Mag Reson Med 27:
153. Lena B, Bos C, Ferrer CJ, et al (2021) Rapid 2D variable flip angle method for accurate and precise T1 measurements over a wide range of T1 values. NMR in Biomedicine 34:. https://doi.org/10.1002/nbm.4542
154. Bitton RR, Webb TD, Pauly KB, Ghanouni P (2019) Prolonged heating in nontargeted tissue during MR-guided focused ultrasound of bone tumors. Journal of Magnetic Resonance Imaging 50:1526–1533. https://doi.org/10.1002/jmri.26726
155. Fu F, Xin SX, Chen W (2014) Temperature-and frequency-dependent dielectric properties of biological tissues within the temperature and frequency ranges typically used for magnetic resonance imaging-guided focused ultrasound surgery. International Journal of Hyperthermia 30:56–65.
https://doi.org/10.3109/02656736.2013.868534
156. Kremer R, Gilsanz V (2016) Fat and Bone: An Odd Couple. Frontiers in Endocrinology. https://doi.org/10.3389/fendo.2015.00190
157. Wu F (2014) High intensity focused ultrasound: A noninvasive therapy for locally advanced pancreatic cancer. World Journal of Gastroenterology 20:16480–16488
158. Bley TA, Wieben O, Francois CJ, et al (2010) Fat and water magnetic resonance imaging. Journal of Magnetic Resonance Imaging
159. Svedin BT, Payne A, Parker DL (2019) Simultaneous proton resonance frequency shift thermometry and T 1 measurements using a single reference variable flip angle T1 method. Magnetic Resonance in Medicine 81:3138–3152.
https://doi.org/10.1002/mrm.27643
160. Yuin S, Elevelt A, Donato K, et al (2015) Bone metastasis treatment using magnetic resonance-guided high intensity focused ultrasound. 81:513–523
161. Napoli A, Anzidei M, Boni F, et al (2013) MR Imaging – guided Focused Ultrasound for Treatment of Bone Metastasis. 1555–1569
162. Uchiyama T, Honda M (2010) Measuring subcutaneous fat thickness in humans using ultrasonic waves. IEEJ Transactions on Electrical and Electronic Engineering 5:. https://doi.org/10.1002/tee.20539

163. Lena B, Bartels LW, Ferrer CJ, et al (2021) Interleaved water and fat MR thermometry for monitoring high intensity focused ultrasound ablation of bone lesions. Magnetic Resonance in Medicine 86:2647–2655.
https://doi.org/10.1002/mrm.28877
164. Suomi V, Komar G, Sainio T, et al (2019) Comprehensive feature selection for classifying the treatment outcome of high-intensity ultrasound therapy in uterine fibroids. Scientific Reports 9:. https://doi.org/10.1038/s41598-019-47484-y
165. Kikinis R, Pieper SD, Vosburgh KG (2014) 3D Slicer: A Platform for Subject-Specific Image Analysis, Visualization, and Clinical Support. In: Intraoperative Imaging and Image-Guided Therapy
166. Ramaekers P, Ries M, Moonen CTW, de Greef M (2017) Improved intercostal HIFU ablation using a phased array transducer based on Fermat's spiral and Voronoi tessellation: A numerical evaluation. Med Phys 44:1071–1088.
https://doi.org/10.1002/mp.12082
167. Kyriakou Z, Corral-Baques MI, Amat A, Coussios CC (2011) HIFU-Induced Cavitation and Heating in Ex Vivo Porcine Subcutaneous Fat. Ultrasound in Medicine and Biology 37:568–579. https://doi.org/10.1016/j.ultrasmedbio.2011.01.001
168. Partanen A, Mougenot C, Vaara T (2009) Feasibility of agar-silica phantoms in quality assurance of MRgHIFU. In: AIP Conference Proceedings
169. Pennes HH (1948) Analysis of tissue and arterial blood temperatures in the resting human forearm. J Appl Physiol 1:93–122.
https://doi.org/10.1152/jappl.1948.1.2.93
170. Ramaekers P, de Greef M, van Breugel JMM, et al (2016) Increasing the HIFU ablation rate through an MRI-guided sonication strategy using shock waves: Feasibility in the in vivo porcine liver. Physics in Medicine and Biology 61:1057–1077.
https://doi.org/10.1088/0031-9155/61/3/1057
171. Bucknor MD, Ozhinsky E, Shah R, et al (2017) Effect of Sonication Duration and Power on Ablation Depth During MR-Guided Focused Ultrasound of Bone. Journal of Magnetic Resonance Imaging 46:1418–1422.
https://doi.org/10.1002/jmri.25676
172. Chan AK, Sigelmann RA, Guy AW (1974) Calculations of Therapeutic Heat Generated by Ultrasound in Fat–Muscle–Bone Layers. IEEE Transactions on Biomedical Engineering BME-21: https://doi.org/10.1109/TBME.1974.324314
173. Hudson TJ, Looi T, Pichardo S, et al (2018) Simulating thermal effects of MR-guided focused ultrasound in cortical bone and its surrounding tissue: Medical Physics 45:506–519. https://doi.org/10.1002/mp.12704
174. Vyas U, Christensen D (2012) Ultrasound beam simulations in inhomogeneous tissue geometries using the hybrid angular spectrum method. IEEE Transactions on Ultrasonics, Ferroelectrics, and Frequency Control 59:.
https://doi.org/10.1109/TUFFC.2012.2300
175. Ritchie R, Collin J, Coussios C, Leslie T (2013) Attenuation and De-focusing During High-Intensity Focused Ultrasound Therapy Through Peri-nephric Fat. Ultrasound in Medicine and Biology 39:1785–1793.
https://doi.org/10.1016/j.ultrasmedbio.2013.04.010
176. Goss SA, Johnston RL, Dunn F (1978) Comprehensive compilation of empirical ultrasonic properties of mammalian tissues. Journal of the Acoustical Society of America

64:423–457. https://doi.org/10.1121/1.382016
177. Duck FA (1990) Physical Properties of Tissue. A Comprehensive Reference Book
178. Dussik KT, Fritch DJ, Kyriazidou M, Sear RS (1958) Measurements of articular tissues with ultrasound. Am J Phys Med 37:160–165. https://doi.org/10.1097/00002060-195806000-00013
179. Anderson P (1957) Call Me Joe. Astounding Science Fiction
180. Florkow MC, Willemsen K, Mascarenhas V v., et al (2022) Magnetic Resonance Imaging Versus Computed Tomography for Three-Dimensional Bone Imaging of Musculoskeletal Pathologies: A Review. Journal of Magnetic Resonance Imaging
181. Jerban S, Chang DG, Ma Y, et al (2020) An Update in Qualitative Imaging of Bone Using Ultrashort Echo Time Magnetic Resonance. Frontiers in Endocrinology 11
182. Carroll TJ, Sakaie KE, Wielopolski PA, Edelman RR (2005) Advanced Imaging Techniques Including Fast Imaging. In: Clinical Magnetic Resonance Imaging, 3rd ed
183. Nishimura DG, Vasanawala S (2000) Analysis and reduction of the transient response in SSFP imaging. Proceedings 8th Scientific Meeting, International Society for Magnetic Resonance in Medicine 8:301
184. Deshpande VS, Chung YC, Zhang Q, et al (2003) Reduction of transient signal oscillations in true-FISP using a linear flip angle series magnetization preparation. Magnetic Resonance in Medicine 49:151–157. https://doi.org/10.1002/mrm.10337
185. Chavhan GB, Babyn PS, Jankharia BG, et al (2008) Steady-state MR imaging sequences: Physics, classification, and clinical applications. Radiographics 28:1147–1160. https://doi.org/10.1148/rg.284075031
186. Hargreaves BA, Vasanawala SS, Pauly JM, Nishimura DG (2001) Characterization and reduction of the transient response in steady-state MR imaging. Magnetic Resonance in Medicine 46:149–158. https://doi.org/10.1002/mrm.1170
187. Parker DL, Smith V, Sheldon P, et al (1983) Temperature distribution measurements in two dimensional NMR imaging. Medical Physics 10:321–325.
https://doi.org/10.1118/1.595307
188. Lewa CJ, Majewska Z (1980) Temperature relationships of proton spin-lattice relaxation time t1 in biological tissues. Bulletin du Cancer 67:525–530
189. Kuroda K, Obara M, Cauteren M, et al (2009) Temperature Dependence of Relaxation Times in Individual Fatty Acid Components and Its Consideration for MR Thermometry of Adipose Tissues. Proceedings 17th Scientific Meeting, International Society for Magnetic Resonance in Medicine Honolulu:2533
190. McLean M, Parker DL, Odéen H, Payne A (2021) A T1-based correction method for proton resonance frequency shift thermometry in breast tissue. Medical Physics 48:4719–4729. https://doi.org/10.1002/mp.15085
191. Baron P, Deckers R, de Greef M, et al (2014) Correction of proton resonance frequency shift MR-thermometry errors caused by heat-induced magnetic susceptibility changes during high intensity focused ultrasound ablations in tissues containing fat. Magnetic Resonance in Medicine 72:1580–1589.
https://doi.org/10.1002/mrm.25063
192. Svedin BT, Payne A, Bolster BD, Parker DL (2018) Multiecho pseudo-golden angle stack of stars thermometry with high spatial and temporal resolution using k-space weighted image contrast. Magnetic Resonance in Medicine 79:.
https://doi.org/10.1002/mrm.26797 **193.** Todd N (2016) Advances in Image Recon-

struction Methods for Real-Time Magnetic Resonance Thermometry
194. Gaur P, Grissom WA (2015) Accelerated MRI thermometry by direct estimation of temperature from undersampled k-space data. Magnetic Resonance in Medicine 73:. https://doi.org/10.1002/mrm.25327
195. Song HK, Dougherty L (2000) k-Space weighted image contrast (KWIC) for contrast manipulation in projection reconstruction MRI. Magnetic Resonance in Medicine 44:.https://doi.org/10.1002/1522-2594(200012)44:6<825::AID-MRM2>3.0.CO;2-D
196. Leiner T, Bennink E, Mol CP, et al (2021) Bringing AI to the clinic: blueprint for a vendor-neutral AI deployment infrastructure. Insights into Imaging 12
197. Seasons GM, Mazerolle EL, Sankar T, et al (2019) Predicting high-intensity focused ultrasound thalamotomy lesions using 2D magnetic resonance thermometry and 3D Gaussian modeling. Medical Physics 46:5722–5732.
https://doi.org/10.1002/mp.13868
198. Allen SP, Prada F, Xu Z, et al (2021) A preclinical study of diffusion-weighted MRI contrast as an early indicator of thermal ablation. Magnetic Resonance in Medicine 85:. https://doi.org/10.1002/mrm.28537
199. Giles SL, Winfield JM, Collins DJ, et al (2018) Value of diffusion-weighted imaging for monitoring tissue change during magnetic resonance-guided high-intensity focused ultrasound therapy in bone applications: an ex-vivo study. European Radiology Experimental 2:. https://doi.org/10.1186/s41747-018-0041-x
200. Fujii M, Sakamoto K, Toda Y, et al (1999) Study of the cause of the temperature rise at the muscle-bone interface during ultrasound hyperthermia. IEEE Transactions on Biomedical Engineering 46:. https://doi.org/10.1109/10.759050
201. Lam NFD, Rivens I, Giles SL, et al (2020) Prediction of pelvic tumour coverage by magnetic resonance-guided high-intensity focused ultrasound (MRgHIFU) from referral imaging. International Journal of Hyperthermia 37:.
https://doi.org/10.1080/02656736.2020.1812736
202. Manni F, Ferrer C, Vincent CEC, et al (2021) Augmented-reality visualization for improved patient positioning workflow during MR-HIFU therapy. In: Medical Imaging 2021:Image-Guided Procedures, Robotic Interventions, and Modeling. SPIE, p 81
203. Huisman M (2014) MR-HIFU for treatments of painful bone metastases
204. Ollivier L, Brisse H, Leclere J (2002) Bone marrow imaging: Follow-up after treatment in cancer patients. Cancer Imaging 2:90–92 **205.** Bucknor MD, Chan FP, Matuoka JY, et al (2020) Cost-effectiveness analysis of magnetic resonance-guided focused ultrasound ablation for palliation of refractory painful bone metastases. International Journal of Technology Assessment in Health Care.
https://doi.org/10.1017/S0266462320001907
206. Bertrand AS, Iannessi A, Natale R, et al (2018) Focused ultrasound for the treatment of bone metastases: Effectiveness and feasibility 11 Medical and Health Sciences 1103 Clinical Sciences. Journal of Therapeutic Ultrasound 6:1–9.
207. Sun Y, Zhang H, Xu H rong, et al (2019) Analgesia of percutaneous thermal ablation plus cementoplasty for cancer bone metastases. Journal of Bone Oncology 19
208. Sharma K v., Yarmolenko PS, Celik H, et al (2017) Comparison of Noninvasive High-Intensity Focused Ultrasound with Radiofrequency Ablation of Osteoid Osteoma. Journal of Pediatrics 190:222-228.e1. https://doi.org/10.1016/j.jpeds.2017.06.046

List of Publications

Journal Publications

van der Velden B.H. M, van Rijssel M.J., **Lena B.**, Philippens M.E.P., Loo C.E., Ragusi M.A.A., Elias S.G., Sutton E.J., Morris E.A., Bartels L.W., Gilhuijs K.G.A.
Harmonization of Quantitative Parenchymal Enhancement in T1 -Weighted Breast MRI, Journal of Magnetic Resonance Imaging. 2020; 52:1374-1382.

Lena B., Bartels L.W., Ferrer C.J., Moonen C.T.W., Viergever M.A., Bos C.
Interleaved water and fat MR thermometry for monitoring high intensity focused ultrasound ablation of bone lesions, Magnetic Resonance in Medicine. 2021; 86:2647-2655.

Lena B., Bos C., Ferrer C.J., Moonen C.T.W., Viergever M.A., Bartels L.W.
Rapid 2D variable flip angle method for accurate and precise T1 measurements over a wide range of T1 values, NMR in Biomedicine. 2021; 34:01-14.

van Leeuwen F.H.P.*, **Lena B.***, Zwanenburg J.J.M., van Vulpen L.F.D., Bartels L.W., Fischer K., Nap F.J., de Jong P.A., Bos C., Foppen W.
Detecting low blood concentrations in joints using T1 and T2 mapping at 1.5, 3, and 7 T: an in vitro study, European radiology experimental. 2021;5(1):51.

Lena B.*, Florkow M.C.*, Ferrer C.J., van Stralen M., Seevinck P. R., Vonken E.P.A., Boomsma M.F., Slotman D.J., Viergever M.A., Moonen C.T.W., Bos C., Bartels L.W.
Synthetic CT for the planning of MR-HIFU treatment of bone metastases in pelvic and femoral bones: a feasibility study. European Radiology. 2022.

Breuer B.J.T., Bošnački D., Xing W., **Lena B.**, Bos C., Bartels L.W., Elevelt A., Modena D., Hilbers P.A.J., ten Eikelder H.M.M.
Modelling HIFU using geometrical spreading, In preparation.

Lena B., Breuer B.J.T., Ferrer C.J., Bošnački D., Ramaekers P., Moonen C.T.W., Viergever M., Bos C., Bartels L.W.
The influence of fat layer thickness and sonication settings on the Energy Density on Bone Surface during MR-guided focused ultrasound on bone. Under revision in Physics in Medicine and Biology.

Conference Proceedings

Lena B., Bos C., Moonen C.T.W., Viergever M.A., Bartels L.W.
Flip angle optimization and in vitro demonstration of 2D DESPOT1-based fat ther-

mometry
Talk presented at the ISMRM Benelux Chapter 11th annual meeting 2019 in Leiden, the Netherlands.

Lena B., Bos C., Moonen C.T.W., Viergever M.A., Bartels L.W.
Flip angle optimization and in vitro demonstration of 2D DESPOT1-based fat thermometry
Presented at the Joint Annual Meeting ISMRM-ESMRMB 2019 in Montreal, Canada.

Lena B., Bos C., Moonen C.T.W., Viergever M.A., Bartels L.W.
Water-Fat Thermometry using Interleaved 2D Variable Flip Angle and Proton Resonance Frequency Shift Scans
Talk presented at the ImagO Scientific Conference -18 Dec 2019. Granted the best presenter award.

Lena B., Bartels L.W., Moonen C.T.W., Viergever M.A., Bos C.
Water-Fat Thermometry using Interleaved 2D Variable Flip Angle and Proton Resonance Frequency Shift Scans
Presented at the ISMRM Benelux Chapter 12th annual meeting 2020 in Arnhem, the Netherlands.

Lena B., Bartels L.W., Moonen C.T.W., Viergever M.A., Bos C.
Interleaved water and fat MR thermometry for monitoring HIFU ablation of bone lesions
Presented at 7th International Symposium on Focused Ultrasound 2020, Virtual Conference & Exhibition.

ACKNOLEDGMENTS

PRE-ACKNOWLEDGEMENTS – ON A PERSONAL NOTE

"Doing research" is a very broad term: normally, it involves identifying a research question, designing experiments, interpreting the findings. Often, it also implies considering the available resources. This can range from implementing an old MR release on the scanner for a specific sequence, to performing an analysis on available retrospective patient data. Moreover, it may constrain some scientific choices and/or it implies finding unconventional solutions in designing experiments. For all these reasons, being such a complicated task, doing research is rarely a solo-work. This chapter is dedicated to all the people that in these years helped me to move further in conducting research. Some of them were highly involved in the projects and became co-authors, others helped for maybe a single task, but at the right moment, many others offered moral support. They were all crucial. This chapter is dedicated to them.

DANKWOORD

I've started to write this chapter already five years ago in my mind and now it's time to put it on paper.

First and foremost, thanks to my daily supervisors, Wilbert and Clemens, for the constant guidance, and understanding. Our weekly meetings were always funny, relaxed, but also serious and challenging moments. I treasure them. You were both my mentors, supervisors and role models to look at. You taught me how to do science and be a good scientist. Thanks Wilbert, for being the first one to believe in me in that August 2017 and for providing from that moment on, constant support. You left me space to grow as researcher addressing me in the right direction, without letting me down when I was lost. Clemens, you were always able to spot when I was not 100% and to take action on it, thanks for your sensitivity, countless hours at the scanner and for being always available for a chat or a meeting when I had a doubt (although sometimes I still hear echoes of that "Bea, Bea, Bea,..."). You both manage to be really present on a weekly basis, even during pandemic, which was not an easy task.

Thanks to my promotors, Max and Chrit, for the interesting discussions (not only science related) and for giving me the opportunity of doing a PhD at the UMCU, one of the most beautiful experiences of my life. Max, you helped me in keeping all my PhD under control and in getting always a clear idea of the next steps. Special thanks for your support and organization in the last months. Chrit, even though PhD can be stressful, I have never perceived pressure from your side. Thanks for welcoming me with a smile, from the first time I enter your door, until the last time we met in person. You are a milestone in the story of HIFU and for me, it was an honor to do my PhD in your group.

Among my supervisors, I have to mention Cyril. From my first months at the UMC, you motivated me and from my third year, you actively joined my supervision. I listened to you and I kept "pushing and keeping up the good work" until the end. So if I'm defending soon, it's also because of you. Thanks for being a friend, beside my cool supervisor.

To my reading committee and opponents, Prof.dr. J.J. Verlaan, Prof.dr.ir. C.A.T. van den Berg, Prof.dr. H.M. Verkooijen, Prof.dr. P.A.J. Hilbers, Prof.dr.ir. T.W.J. Scheenen, thanks for the time you dedicated to my thesis. I hope it insprired you interesting questions and we will have a lively discussion on the day of my defence.

I had the luck of being part of the PROMETHEUS project, that held together people from different organizations. Thanks to this project, I could collaborate with Boris and Dragan, from TUe Eindhoven and Jorik and Martijn, from Isala. Dragan and Boris, thank you for being always available for a discussion or clarification. Our constant exchanges allowed me not only to get a better understanding of the simulation world, but also helped me to organize and explain my work better. Martijn and Jorik, thanks for opening my eyes on the clinical applications of HIFU and to answer my innumerable questions regarding the treatment. Martijn, your clear way of how much clinics can benefit from research and viceversa were inspring for me. You didn't look at these worlds as apart but just as two sides of the same medals. Thanks also for bringing some italian (and Dante) in our conversations. Jorik, your critical mind and vision helped to improve a couple of chapters in this thesis and above all, special thanks for all the help with the data transfer! I bet at a certain point you might have had some nightmares at seeing my emails popping in, requesting more and more data/info, but you never showed it, being always kind and welcoming.

Many thanks to the past and present administrative staff in ISI: Marjan, Jacqueline, Renée, Anna, and Maria, for organizing people, documents, meetings and most important, social events and for keeping a lively environment. Special thanks to Maria, who brings such an explosive atmosphere everywhere she goes.
Big thanks to Gerard, for the rapid and efficient technical support when I needed it (especially for every password reset when my account was locked).

"Hi, this is Beatrice from MR23, I have a problem..." I guess Technisch Cluster has heard this call many times, as the scanner is often not an easy lady. Thanks for helping out with small and big issues. Especially to Dominique, that everytime with patience, came to listen to my problems (also when they involved implementing strange sequences on the scanner and the creation of multiple disksets).

This thesis would have not been the same without the discussions I had with many clinicians and researchers, that helped to shape its current form. Thus, I would like to thank from the clinical side Manon Braat, Inez Verpalen, Evert-Jan Vonken, Niels Blanken and Simone ter Horst. From the research side, thanks to Peter Seevinck, and Marijn van Stralen, fundamental for the second chapter of this thesis and Roel Deck-

ers and Mario Ries, for the feedbacks in the lab or during the HIFU meetings. Eduard Faber came in help in a moment in which all hopes were lost, with a shiny release 3.2.3 that I could install in the scanner to continue my research after being stuck for almost one year, my heartfelt thanks.

During a side project, I got the pleasure of collaborating with Wouter Foppen and Floor van Leeuwen. Wouter, with your open and friendly mind, you created an enjoyable environment to work in. Floor, the more we struggled with Albi, the more we became friends. So in the end, I'm glad things didn't go smoothly with the phantom! Thanks for your passion and your commitment in the project. You're organized and motivated, which make you a nice coworker, but also funny, social and enthusiast, which make you a great friend.
During the last years, I spent much more time at UMCU than everywhere else. The reason is that I loved my project, of course (need to write it, my supervisors may still read this :D), but also because of the people I met. Most of these people are still very present on my daily life; more than colleagues, they became friends, some even family. I like lists, so I will divide them accordingly:

- the greatest E corridor: you must know that in our division, there is a constant competition between the E and the Q building. Obviously, all the fun things as long coffee breaks, wheel chair competitions, camels passing by happened in the E corridor. Not just for the building itself, of course, but more from people that passed by there. So thanks to (at least, my) old E corridor: Alberto, the friend I trusted from the first time we met, that I referred to for MatLab, apartment choices, coffee breaks, sports; Mike, professor Mike, with his acute cleverness (you have been my example PhD model) and clear vision of the world and Harry Potter passion (when the next HP concert?); Erik, triathlon sportive guy, full of surprises, being it an hilarious joke with a straight face or its ability to dance; Hui Shan, for all the passions we share as reading, singing and physics, Fenghua and Hui, my first office mates that bear my eccessive excitement about everything and my constant talking; Marielle, the smart woman, so precise at work and life of the party outside, being it UMC parties, Uppsala, your wedding, you're fun! Sam, with your impressive memory, you really remember everything, from complicated math formulas to sentences rapidly said, thanks for being present, Ruurd, with your beautiful smile everytime you're meeting someone, you're the definition of cheering person, and for all your amazing adventures, you really know how to live; Nadieh, see later; Majd, thanks for teaching me about Middle East (and how to make Maqluba!)and for the constant funny and light environment you create; Sanne, you're definitely a woman that is not afraid of dirty her hands, being it house works, pregnancy or PhD, thanks also for showing me your house in Castricum; Julia, thanks for all the dances, trips, dinner and moments we shared. Your endless energy make of every little occasion a party! I admire your open humor and sociality, with which you create a vibrating social environment everywhere you go. You're probably the most charismatic (and resilient) friend I have. Tush and Steffen, we shared the same path and we immediately became friends. I have so many memories with you. Tush, oh nananana, c'mon! The man with endless energy, you were a constant throughout my PhD, I could

count on you for an advice, brainstorming, coffee break, squash and getting a blast at parties. You were the first guest in my house and with our improvised dinner on the floor, dancing salsa, you definitely gave a good start to my life in Utrecht. Steffen, thanks for bearing with my delays and my being all over the place, for being up to try out new things together and still sharing your life with me. Almost five years ago, with a bluntness typical of only Germans maybe, you asked me if I was really interested in hearing what happened to you (related to a story), the answer will always be "yes".
Great people started in this hallway, but other great people kept coming. So thanks also to the new E corridor: first of all, my amazing office mates, Nils and Ishaan. With Nils and his constant curiosity, I have never had a boring conversation; Ishaan, my forevaaa friend, in our world of young people with old souls, we understand each other; our discussions about books, movies, handwritten letters were my daily breath of fresh air, thanks to you, my list of books on Goodreads is diverging! Jorg and Louis, even for a short time before your moving, I really enjoyed our exchanges, with the critical mind of Louis and the capacity of listening of Jorg; Max, miniMax, I Hcannot Hnot Hmention How hmuch hI henjoy hexplaining my Heating project to you! For you, everyday there is a new possibility for jokes and in the (very very) end, I really like this side of you, plus, you get this ability of being naturally likeable by everyone which I'm really envious of. Mark, you brought further new energy to the group, being always up for drinks, chat, events and providing interesting stories about houses, Formula 1, New Zealand, one of your many (before pandemic) concerts, or the US. Saeed, calm and speaking only after reasoning, thanks for your politeness of other times and for making me try lots of great Iranian treats. Kim, the bound with you was almost immediate, seeing our almost identical sensitivity. Your kindness and constant attention to how others are feeling is unbeatable. We shared great memories, all over Europe, but sometimes, the nicest moments were just with "we three". You always try to save the world and that's incredible, but please don't forget how incredible you are. Thanks for your kindness and honest talks.
And to even newest PhD students in E: Rens, Iris, Ryanne, Matthijs, Cyrano, keep up the good reputation of our corridor!

- the Q, ISI, people: Niko, Christian, Edwin, Szabolcs, Ahmed, Jiggy, Hugo, Bas, Frank, Job, Matthijs. Special thanks to Jiggy, for being my croatian complaining friend of great taste and cooking skills, everytime we meet is a party; I'm glad we kepy in touch. Matthijs, with who I share a birthday and a tiramisú competition, thanks for being a very good listener, truly interested in someone's life.

- the Q, but not ISI people of the HIFU (not all doing HIFU) group: Isabell, Suzanne, Anita, Cyril, Josanne, Helen, Yulia, Cornel, Pim, Mark. Thanks also to the many students, Annemiek, Symona, Megan, Mark, Stan, Ryan and all the others I might forget to mention now, for keeping the group young and dynamic. Suzanne, your calm nature, generosity and incredible cooking skills are perfect to spoil people, thanks also for the many sport sessions together and for our on-going Christmas cookies tradition, which is one of my favourite moment in the year! Isy, you're German dynamite, a cookiemonster, the perfect and motivating sport buddy and

one of my closest friends; you entered with a kick in my life and from then, it's always fireworks when we meet. Thanks for your positive energy, the endless talks, your incredible way of explaining things and your deepest understanding.

- the 7T (but not working with 7T) people: Soraya, my mentor in the last years of PhD, thanks for your wise advices, Carlo, with your exceptional creativity, you're constantly looking for new ways to fill your life and this has been inspriring for me. Lisa, my feminist friend, your bright eyes and clear vision of the world challenged me to always do a bit better. Thanks for helping me finding a way out, when I saw none and for believing in me.

- the non-MRI group: Claudia, Marti and Vania. Vania, see later; Cla, from dancing flamenco on a random saturday, we became housemates. You brought green, delicious improvised cenette, and the sense of family in the house. Thanks also for the great combined birthday celebrations. Marti, you're the queen of this group, even though your PhD subject gets often mistaken for MRI. Thanks for being present and interested, for your sarcasm and humor, our weekly meetings is something I always look forward to and your messages always bring me a smile. I'm looking forward to buy your first book (beside your thesis, that I'll get for free, right? Good luck in finishing!).

- the Italian lunch break people: Guido and Gabriella, my italian godfather and godmother in the hospital.

- my paranymphs: Luisa, what a suprise to find the sister I've never met here in Utrecht. These years have been so great also because I could share so much of my life with you. From work to home, from parks to parties, from holidays to movies, from bouldering to lindy hop (:D), from MR courses/conferences to quarantine, you were there. You understood me immediately, like we have known each other forever. Thanks for the many times you checked I was not working too hard, I was taking proper rest and I was feeling good. Thanks also for all the vegan meals and cakes you prepared me, often with Marti! We supported each other in many occasions, especially during pandemic, which would have been much much harder without you. The late night talks in your terrace are still one of my favourite memories from the PhD time.
  Nadieh, you have been the first friend I made in Utrecht. You welcomed me immediately, opening your heart and talking with me about everything. Something that we have never stopped doing, being it during a 6-hours flight to Canada, on our morning runs, on parallel routes on a boulder wall, walking the city to get an icecream. You were a pillar for me in our corridor, the person I would go for a chat, a laugh, an update, but also for difficult moments, to get comfort. I missed more than expected to not have you so close by any longer.
  Vania, my captain, somehow our lives keep being more and more entangled. Your warm laugh immediately caught me on a movie night in Biltstraat and since then, has never left me alone. You're the person I can always count on: a partner in crime to get a blast at parties (and make people drink horrible liquors...) or at concert, a (shouting) guiding light on the football field, a Vaniliveroo provider when I'm sick and stuck at home, a sun to brighten days in the office or at the

scanner and above all, bad Thursdays. Your generosity and creativity have been true inspiration for me. Thanks also to your amazing partner, Nino, that welcomed me as family and I truly consider a cousin.

Huge thanks to those who participate to my Harry Potter and risotto nights, movieclubs, dinners, Christmas days, you made me feel at home.

I have been so lucky with my PhD and I cannot believe I got lucky again during my postdoc. After leaving an amazing environment as UMCU, I tried not to have too many expectations for afterwards. But, again, I've found a social, welcoming, funny group at the Gorter MRI Center in Leiden UMC, for my postdoc. With the almost-everyday cakes, long coffee breaks, sunny (it's still summer now) outside lunches with the all group, I couldn't believe my luck, for the second time in a row. Thanks for welcoming me. Special thanks to the low field group, Andrew, Chloé, Tom, Javad, Bart, Wouter, and my office mates, Lisa, Rosanne and Yiming, for the support and interest also in the last phases of my PhD.

My PhD got partially hit by pandemic, but before this happened, I enjoyed a lot to go conferences. Not only for their vibrating environments, that made the days overwhelming, but also, of course for the social part. And one conference, ISMRM 2019, gifted me two important people. Banafshe, we connected thanks to the Iranian "mafia", and both me and my stomach cannot be happier of the choice! You care so much about the people you love, you seem calm, but there is so much energy inside you! I'm glad to call you friend. Michele, my brother, obviously, the Bea of Antwerp and the Mik of Utrecht had to get along each other. I've known you forever, even if I've only met you 3 years ago. Thanks for bringing constant positivity, energy and randomness to every occasion.

After a long day of work, I was also happy to go back home. And that studio in Gasthuistraat, beside being a restaurant, a cinema, a discopub, a call center, an office, a yoga studio, a psychology corner, a Christmas cave, was, above all, home. Again, not because of the building per sé (it actually had pretty horrible steep stairs), but for the inside. I've already mentioned Claudia and Luisa, but there were/are also Melina, Simone, Ioannis, Iria, Filipe, Andrea... Thanks for spoiling me, checking on me, for the constant music and the big hugs. I'm gonna be repetitive, but I cannot stress enough how much this house helped me to get through pandemic. Filipe, "poisch" (or how you pronounce it), you manage to keep taking care of me even if we don't live together any longer! You were a great adding to the house. I'm always impressed by your elegance (perfect outfit, even when you work from home). Thanks also for being the person I can comment Eurovision with! Andrea, you told me the first day you arrived "we are not only housemates, but also friends" and you kept that promise. I miss that "Beaaaaaa" shouted across the walls, your improvised appearance in my living room, asking for dinner, and our afternoons and evenings dancing salsa (not your playing guitar, though :D). I'm glad though to know you're happy in Brazil.
In my free time, among the many hobbies and sports I picked up during the years, there is a constant: football. I thought I had to give it up, when I arrived in the Netherlands, as it would have been difficult not speaking dutch. Who would have thought that two

amazing women, zia Ale and Lucia, one evening in a bar, decided to start an Italian female football team in Utrecht? And that this team gets an increasing number of players, has a strange name and takes part of multiple tournaments? Thanks to my beautiful team, COI One, for being the funniest, most social, most screaming and probably on average formed by the shortest players in all Utrecht (or even NL). (For those who have read Vania's thesis, this might be repetitive, but sorry, it's always the same team!)
From the gol, the formation is: the gol keepers Vania, and Alessia, that gave literally everything for the team, from her lungs to her poor ankles. In the defence, my half-heart, non-passa-niente Laura, with who I have way too many things in common, our founder Lucia il cigno, with her elegance on the field, the unstoppable mastino Monica, the scaramantic enjoying-life-and-Italy Chiara, and Sonia Mento (do I really have to explain why she is called Sonia Mento here?). Middle field: Rosa, lief onvermoeibare Rosa, een kleine tractor in het veld, met een enorme passie voor Nederlands en voetbal (alleeen voor jou heb ik deze zin in het Nederlands geschreven!), Marghe, che non si vergogna di urlare "la vergogna!" quando sí, dovremmo vergognarci :), Marta P., even though sometimes it's difficult, month after month, you're doing your best to come to support this team, Giuliana, the proud sicilian, hoping you could play with us next season. Attack: Ary, la bomber per eccellenza, Irene dal piede d'oro, that made us score 3 or 4 times more than last year, occasionally Giulia la judoka, that knocks out the opponents only looking at them, zia Ale, la ballerina e narratrice della squadra, la sprizzante insegnante di yoga e italiano che mi ha (per mia fortuna) adottato. Not often playing but still very much part of the team: Claudia, Erika, Stefi, Marta M., Anouk, Michela. The always present supporters (and sometimes, life savers!) : Sonia, Myléne and Kelly. Special thanks, Sonia and Myléne, for the beautiful house you left me.
Thanks to all the trainers we had, Germano, Marco, Mario, Andrea, Giuseppe. Specialmente a Mario, che settimana dopo settimana, anno dopo anno, é sempre pronto, sul campo a supportarci, sopportarci e allenarci. None of this would have been possible without Roberto, il presidente, that so proud of the team, is always sponsoring and supporting us.
Among the other hobbies, I love reading and I've finally managed to realize one of my childhood dream, participating to a real bookclub. To the bookclub "Wisdom Tea and Whiskey", thanks for the many interesting discussions, scientific and not related Bruno, Cisco, Lieke, Martine, Suzanne, Hilde, Daniel, Martina, Vania, Lefkios, Pascal, Cinta. Our gatherings are something that I always look forward to (especially when we have some nice yogurt cake from Vania, pasteis de nata from Hilde, nice brunches out, etc). Dear Bruno, thanks for founding this beautiful group, bringing always chill positive vibes around, for the challenging mudrun in October and sharing our PhD experience together.
In the evenings after work or in the weekend, I often hang out with people from a very mixed group, the opulence group: Jo, Deji, Ele, Casper, Lisa, Laura, Isy, Suzanne, Cyril, Luisa, Marti, Celeste. Thanks for the many moments together, in bars, parks, beaches or boulderhals. Especially to Laura, thanks for bearing all the PhD related talks, being so sweet and social (this makes you definitely an atypical Dutchie), and the bouldering support sessions.

From distance, all the way from Italy, I got daily support, which didn't lose strength

throughout the years. The Durga Puja group, founded in the first years of university, counts 12 amazing girls and still gets a deep bound even at distance. This is already the third time that they ended up on my thesis, so you can imagine how strong and long is our bound. Thanks to Marti, Cami, Miky, Alice, Esty, Eli, Alma, Chiara, Ale, GiuliaBaj and Silvia, for the trips in Europe, le feste e controfeste, dinners, calls, improvised birthdays and lately even concerts. Marti, il "quando sono con te divento piú scema" is still valid, thanks for the serious talks, laughs, dinners and many ice creams. Milla, tata, the last time we met you told me "non ci vediamo spesso, ma non importa, quando succede, in un attimo sembra di vivere di nuovo a Pavia insieme", this is so true, you touched my heart, Miky, from the slides by Fraternale (with the explanation of resilience), you have always given me so much strength and confidence, thanks for being one of my best friends, Alice, mia moglie, even though sometimes you betray me, I know that your love is true, Eli, thanks for the daily intake of Guanciottolo, and for making me laugh like no other when we meet (even for your bad jokes, like Silvia), Esty, the owl, thanks for playing constant tetris with your job, to make our meetings possible, Chiara, as Esty, thanks for trying to balance your shifts at the hospitals with our calls and meetings, GiuliaBaj, thanks for sharing the struggles of the end of the PhD, Alma, thanks for reporting all the funny examples with your students and for the good books and music advices, Silvia, Soooooolvia, thanks for the long calls, walks and jokes (of good and bad quality, see Eli), my sofa and Utrecht are waiting for you and your yellow creativity again! Thanks also to Lavy, who joined a little later, but it's at all percent part of this group, I'm so happy you visited me in Utrecht!
Maybe I would not have been so fond of Utrecht from the very first moment, if I had not had Alessandra, my sister/Lore, already here. Ale, I don't have words to describe how grateful I am for all the help you gave me. It has been great to share so much together, from the first day of university in physics to the PhD defences. Da matricoline a dottoresse, ci siamo sempre state l'una per l'altra, che sia a distanza di una camera, di una strada, di mezza Europa, o 10 minuti di bici. Sei la costante tra l'ambiente italiano universitario e quello olandese. Quando siamo assieme, io sono a casa. Grazie per la tua dolcezza, la tua infinita positivitá e pazzia, e per capirmi cosí bene su tutto. Thanks also to Ewan for your infinite patience when I invaded your house as soon as you arrived in the Netherlands, but if you were bothered, you didn't show it, as you and Ale spoiled me with great dinners, breakfast, chats and company. It actually went better than any expectations and we became friends, thanks for your dry english humor, the TV series recommendations and for sharing your food and wine passion.
Grazie ad Ary e Paola, per essere le mie migliori amiche da piú di 15 anni ormai. Anche per voi, é la terza volta su una mia tesi. Questo significa che anche stavolta, la nostra amicizia ha superato la distanza. Poi, quando ci vediamo, sembra davvero di essere tornate al liceo, a scherzare, mandarci messaggi o cantare assieme. Grazie anche per aver disegnato la copertina e l'intermezzo di questa tesi, adoro che siate in qualche modo coinvolte anche in questo mio progetto di vita.
Pascal, che dire? Anzitutto, in che lingua scriverti, considerando tutte le lingue che conosci? For a quiet person, it's impressive how you entered my life and overturned it completely. You know me, truly, without boundaries. I cannot thank you for the support, not only, because you lived all the things that I experienced. When I met you, I thought you came out of a Disney movie; with time, you became my best friend, my

skating and squash instructor, a co-author, a philosopher, my psychologist, the perfect travel companion, what makes me smile randomly during the day. You taught me about dutch policy, how to read "Lampje", the best way to cut a tomato. Thanks for understanding me, sometimes more than how I understand myself.

Nella mia famiglia, grazie particolare allo zio Alby, senza il quale, casa mia sarebbe molto piú disastrata. Ti sei fatto 12 ore e passa di auto, solo per potermi aiutare, e non bastano mille grazie per questo. Grazie allo zio Nino, che anche da lontano, si interessa e chiede sempre come sto e come procede il mio lavoro a Utrecht. Grazie tanto a entrambi per essere cosí entusiasti ogni volta che torno e vederci e aggiornarci, spesso davanti a buonissime pizze.
Grazie alla zia Simona, per il costante supporto, per i bellissimi messaggi e le ancora piú belle merende. A lei e a tutta la sua splendida famiglia, lo zio Renzo, Tommy e Chicco.
Il grazie piú grande va ancora a voi, alla mia famiglia. A tutti i sacrifici che avete fatto, a quanto sia difficile stare a distanza, a quanto é bello ogni ritorno e straziante ogni partenza. Vi voglio un bene incredibile e se ho potuto scrivere questa tesi, e difenderla, é grazie a voi. Alle chiamate e i messaggi infiniti, a tutta la pazienza e l'incoraggiamento che mi date, a quanto vi interessate a quello che faccio e studio. Grazie per essere i miei fans numero 1, per sostenermi sempre e comunque e per fare di tutto per essere presenti ad ogni occasione. Grazie, mamma, per essere venuta cosí tante volte ad aiutarmi, prendendo aerei, treni, bici, e andando anche al supermercato a chiedere cose agli Olandesi (ma, mannaggia loro, non capivano!). Grazie, papá, per i viaggi lunghissimi che ti sei fatto e per chiamarmi la sera anche se sei stravolto. Voi siete le prime persone con cui voglio parlare ogni volta che succede una cosa bella. Grazie Lore e Lulú, per avermi sempre coinvolto e fatto sentire parte di questa famiglia. Non potró mai ringraziarvi abbastanza per occuparvi di tenere sotto controllo la casa (e mamma e papá), quando io sono a distanza. Lulú, la tua solaritá contagiosa illumina anche le mie giornate piú grigie, riesci sempre a farmi sorridere, grazie di interssarti tanto alla mia vita. Lore, sei il migliore ascoltatore che conosco, quando ti parlo vedo che ascolti attentamente e quando mi rispondi, é solo dopo aver riflettuto. Grazie per i tuoi preziosi consigli e la tua diversa visione della vita.

You all represented one or more songs I listened to in the soundtrack of my PhD, as background of a pretty city, with a tower I've never seen.

About the author

Beatrice was born on the 23rd of March 1992 in Borgomanero, Italy. She started a humanistic high school (Liceo Classico), thinking that literature, latin and greek would be her whole life. During her studies, she discovered physics and fell in love with it. She finished high school still loving humanistic subjects, but she enrolled for the Physics bachelor course in the University of Pavia. She went to visit CERN during her studies and thought nuclear physics would be her whole life. In the last year of the bachelor course, she discovered MRI and fell in love with it. She graduated in 2014 writing a thesis on the hyperpolarization of nuclear spins in amorphous sugars under the supervision of Dr. Marta Filibian and Prof. Pietro Carretta. She continued her studies at the University of Pavia enrolling in the Biomedical Physics Master program. She joined the I.R.C.C.S. Fondazione Salvatore Maugeri for her master thesis project, under the supervision of Prof. Elio Giroletti and Dr. Luca Moro. Her project focused on the analysis and optimization of the quality controls protocol for functional magnetic resonance at 3 Tesla. She graduated with 110/110 on the 29th of September 2016. After the graduation, she thought she would never do a PhD and left for Ecuador. There, she did an internship in the Radiotherapy Department of the Carlos Andrade Marin Hospital in Quito under the supervision of Dr. William Oña, thanks to the scholarship “Fondo di Cooperazione e Conoscenza” (and the enthusiastic support of her previous supervisor, Elio). She came back from Ecuador, ecstatic about the experience, but missing something in her life. She looked all over Europe where she could do a PhD about MRI, involving Focused Ultrasound, a technique she studied and wanted to investigate. Therefore, in September 2017, she was entrusted with a PhD position in the Image Science Institute of the UMC Utrecht and started working on the "PROMETHEUS - Pain Reduction Of Metastases by THErmal UltraSound" project, aimed at improving the MR-HIFU technology to enhance the clinical applicability for the treatment of painful bone metastases. The project was funded by a partnership between the Dutch Cancer Society KWF and the Technology for Oncology STW. In her PhD, she enjoyed combining different aspects, from MR scanning to building phantoms, from image postprocessing to simulation and sequence development under the supervision of Dr. ir. Wilbert Bartels and Dr. Clemens Bos as copromotors and Prof. dr. ir. Max Viergever and Prof. dr. Chrit Moonen as promotors. The results of her 4 years of research are reported in this thesis.

Currently, Beatrice is working as postdoctoral researcher in the low-field group of C.J. Gorter MRI Center in Leiden UMC, where her main tasks are sequence optimization and image development at low MRI field (i.e., doing the thing she loves more, MR scanning). She has learnt to avoid making big statements about her “whole life”, but not yet how to be concise.